New methods for high-resolution ion beam analysis

Memoria presentada por

Roch Andrzejewski

Para optar al grado de
Doctor en Ciencias Fisicas

Departamento de Fisica Aplicada
Universidad Auttonoma de Madrid

Tesis dirigida por:
Drirk 0. Boerma y David Matrin y Marero

“Among the maxims on Lord Naoshige’s wall there was this one: “Matters of great concern should be treated lightly.” Master Letti commented, “Matters of small concerns should be treated seriously.”

“There is something to be learned from a rainstorm. When meeting with a sudden shower, you try not to get wet and run quickly along the road. But doing such things as passing under the eaves of houses, you still get wet. When you are resolved from the beginning, you will not be perplexed, though you still get the same soaking. This understanding extends to everything.”
“Hagakure, The Book of the Samurai” Yamamoto Tsunetomo

This work I’m dedicating to my mother.

Resumen de la tesis: "**Nuevos métodos para análisis de en alta resolución con haces de iones**" por Roch Andrzejewski

En el año 2003, el Centro de Micro-análisis de Materiales (CMAM) fue oficialmente inaugurado. El Centro forma parte de la Universidad Autónoma de Madrir (UAM). Su principal instalación es un acelerador Tándem de nuevo diseño y un voltaje de 5 MV. El acelerador, de la compañía *High Voltage Europe* (HVEE), está basado en el principio de cascada. El objetivo del Centro es proveer a la comunidad científica local con técnicas standard de análisis mediante haces de iones y modificación de materiales. Más aun, se prevé llevar a cabo novedosos desarrollos a fin de situar al Centro en primera línea dentro de estos campos de investigación. El desarrollo de un espectrógrafo magnético de amplio ángulo usando un novedoso diseño, tal y como se describe en esta tesis, es sólo una prueba de lo plausible de este objetivo. Un importante ingrediente en este progreso, fue la aplicación de técnicas que permiten seleccionar de forma efectiva los sucesos importantes de los que han de ser eliminados. Estas técnicas han sido desarrolladas en aplicaciones de física de partículas elementales en instituciones como el CERN. Dotando al espectrógrafo con estas técnicas, sería posible identificar distintas señales de iones elásticamente dispersados ó retrodispersados (identificados por la masa), sumar efectivamente todos los estados de carga, resolver en ángulo, y prácticamente estar libres de fondo. El análisis de los espectros de energía permitiría la determinación (con una resolución en profundidad de nm) de la concentración y las posiciones de red, tanto de elementos pesados o ligeros diluidos en muestras cristalinas para una profundidad de 100 nm. Las posibilidades del análisis mediante haces de iones se verían así significativamente aumentadas con respecto a alas que ofrecen tanto MEIS como otros espectrógrafos existentes. Sin embargo, los métodos actuales para el análisis de los datos incluyen aproximaciones que pueden introducir errores a la hora de determinar la posición en la red. Con el fin de evitar dichas aproximaciones, se hace necesario un nuevo método de análisis mediante simulaciones por ordenador. Dicho método fue desarrollado en el CMAM principalmente por el Dr. V. Khodyrev. La segunda parte de esta tesis está dedicada a la evaluación y aplicación del nuevo programa de simulación. La tesis se organiza como sigue:

En el Capítulo 2, se presenta una revisión de la técnica de análisis mediante haces de iones y una versión simplificada de las teorías subyacentes. Se describen las posibilidades y también las limitaciones de los distintos métodos que se aplican en la actualidad. Así mismo se muestra un breve resumen de los sistemas de detección para medir espectros de energía de iones dispersados y en retroceso. La geometría óptima de medida y las propiedades de un hipotético detector ideal para medir estos tipos de iones son discutidas también. Finalmente se comenta sobre el análisis de datos y las limitaciones en energía y rango de profundidad, donde se permiten las aproximaciones usando teoría de colisiones simples.

En el Capítulo 3, el diseño de un nuevo tipo de espectrógrafo magnético es presentado. Los distintos métodos y programas de ordenador usados en el diseño del imán del espectrógrafo son discutidos. La característica diferencial del espectrógrafo consiste en un sistema para i) determinar el ángulo mediante el cual los iones entran en el equipo y ii) para identificar sus distintas especies. En este capítulo, se describen los detectores sensibles a la posición, usados en la determinación del ángulo velocidad y especie entrantes. El esquema del análisis de datos multidimensional es descrito en detalle. De la misma forma el resto de hardware del diseño es especificado, incluyendo el soporte del imán permitiendo realizar las medidas a 5 diferentes ángulos de dispersión, el sistema de

ultra alto vacío junto al goniómetro de precisión de múltiples ejes y el sistema de introducción de muestras.
La primera intención fue la de escribir un capítulo separado con los primeros resultados del espectrógrafo. En lugar de eso, los primeros test positivos están incluidos en este capítulo, debido a que el proceso de evaluación aun se encontraba en proceso a la hora de escribir esta tesis. El principal motivo de este lento desarrollo se puede encontrar en el limitado tamaño del grupo de trabajo encargado. Este grupo se encuentra limitado a menos de 2 personas con dedicación completa. Por comparación, actualmente otros 2 espectrógrafos de igual complejidad se encuentran en fase de evaluación. Estos espectrógrafos, usados por la separación de iones radioactivos producidos por un sistema de iones de alta energía, están basados en el mismo principio. Equipos de muchos físicos e ingenieros están trabajando en cada uno de estos sistemas.
En el Capítulo 4, se presenta un nuevo método de simulación de los espectros de energía de iones dispersados y en retroceso. De igual forma que en todos los programas existentes, las simulaciones se realizan mediante el cálculo de un gran número de trayectorias de iones (10^4 -10^6) , usando la aproximación de colisiones binarias. En lugar de un muestreo aleatorio, se sigue el método de muestreo mediante la importancia de alguna de las variables aleatorias. Esto lleva consigo un aumento en la velocidad de la computación de los espectros, permitiendo incluso el análisis de datos de alta energía. Hasta la fecha, esto último sería imposible sin las aproximaciones basadas en el modelo de dispersión simple. En este capítulo se muestran algunos ejemplos de de las simulaciones.
El Capítulo 5 trata del análisis de datos de dispersión de iones de He de 2, 3, y 5 keV por una superficie limpia de Cu(100). En la universidad de Linz, Austria, se había medido la dependencia con los ángulos acimutal y polar de la intensidad dispersada. Los intentos previos de reproducir estos datos con simulaciones no fueron exitosos. En el presente estudio, se usó el programa TRIC, expuesto en el capítulo anterior con el fin de encontrar la causa de la discrepancia. Con TRIC se simularon los barridos con diferentes formas para el potencial proyectil-átomo, con diferentes variaciones en la geometría de medida permitidas por las incertidumbres experimentales y con diferentes valores para la relajación de las capas superficiales. Una búsqueda como esta en un espacio multi-paramétrico del mejor ajuste entre datos medidos y simulados de dispersión de iones de baja energía no hubiera sido posible con otro programa de simulación distinto de TRIC. Finalmente se obtuvo un ajuste casi perfecto. El estudio muestra que la exactitud de la geometría de medida es un factor muy importante, conjuntamente con la elección del potencial de interacción. Este trabajo, que incluye la simulación de miles de espectros en energía, también sirvió como banco de pruebas para el programa TRIC. La conclusión de este trabajo es que la dispersión de iones de baja energía en combinación con el programa TRIC forma un conjunto muy poderoso de herramientas para el estudio de las capas superficiales de superficies cristalinas. En el momento de la escritura de esta tesis, una instalación de este tipo se encuentra en la fase de pruebas en el CMAM.
Debido a que el trabajo que se describe en esta tesis se encuentra aún en progreso, es demasiado pronto para extraer conclusiones definitivas. Sin embargo, se puede afirmar que, en el caso de que el espectrógrafo magnético funcione de acuerdo a las especificaciones, será posible la determinación de las propiedades de materiales como función de la profundidad en la escala nanométrica que no se pueden realizar con otros métodos existentes. El análisis de los datos por comparación con simulaciones se debe realizar con el programa TRIC desarrollado recientemente para evitar las aproximaciones que pueden afectar a la fiabilidad de los resultados. El análisis con técnicas de haces de iones se convertiría así en una herramienta indispensable en los campos de nanociencia y nanotecnología.

Chapter 1. INTRODUCTION

The application of ion beams with energies in the MeV range for solid state physics and materials science (HEIS) started roughly in the sixties of last century. Accelerators in use for nuclear physics studies [1,2,3,4] were used part-time for high-energy ion scattering (HEIS) to study the composition of samples as a function of depth of thin layers. Also the channeling effect was discovered [5] and applied to study the (recovery of) damage in crystals of semiconductors caused by the implantation of dopants The lattice sites of implanted dopants in semiconductors or impurities in metals [7,7] were also studied using the channeling technique. After these early developments the application of accelerators for the analysis of solids became widespread. The rapid growth of this application was stimulated by the emerging semiconductor industry. Another factor was the availability of accelerators (formally) used for low-energy nuclear physics. The auxiliary techniques developed for nuclear physics, such as detectors, electronics, spectrographs were well suited for this new application. The number of accelerators in use for HEIS studies of virtually all materials grew rapidly, to a few hundred in the early nineties. Since that time this number has declined, probably because of the competition with emerging techniques like the application of synchrotron radiation, secondary ion mass spectrometry (SIMS) and laser techniques. Still there are a number of problems for which HEIS is the best technique to provide answers. An example is the determination as a function of depth of the absolute concentration and lattice sites of dilute impurities. However, the application of HEIS for this type of measurement, especially for light elements (H, B, N, O, F), is not straightforward. It requires the unique identification of the signals of light elements in the presence of the much more abundant signals of heavier elements. Practically the only way to do this is by elastic recoil detection (ERD) of light ions with a device allowing for mass identification. This device should cover a large solid angle to reduce the ion fluence required for the measurement. Otherwise radiation damage would severely interfere with the structure determination. In addition, the yield of recoiled ions, summed over all charge states, should be measured as a function of the recoil angle within this solid angle. The energy resolution of the measurement should be compatible with a depth resolution of close to 1 nm, in order to fulfill the requirements of present day´s nano-technology. A device uniting all required properties does not exist yet.

The technique of medium-energy ion scattering (MEIS) of 50-200 keV H or He ions, to study the composition and structure of the first few layers of crystalline samples, may approach best the

mentioned properties. It was developed in the late seventies with the creation of the "TUBA" facility at the AMOLF institute in Amsterdam [8]. With this device the scattering yield from crystalline samples can be measured with an electrostatic analyzer over an angular range of 20º and angular resolved in one dimension, using a position sensitive detector. This technique is still used successfully in a few laboratories, including laboratories in the USA and IBM [9,10], Great Britain [11], Korea [12], and Japan [13], to determine the composition and structure of crystals in a range up to 10 nm, with a depth resolution of 1 nm. The limitations of this technique are the limited depth range, the problem of background subtraction from the signal of light elements and the discrimination between different light elements.

In 2003 the new centre CMAM (Centro de Micro-Análisis de Materiales) was officially inaugurated. The Centre is a part of the Universidad Autónoma de Madrid (UAM). Its main facility is a 5 MV tandem accelerator of a novel type, based on the cascade principle and delivered by High Voltage Engineering Europe (HVEE). The aim of the Centre is to provide the local scientific community with "standard" techniques for ion beam analysis and modification of materials. In addition, new developments are envisaged, placing the Centre at the forefront of modern developments in these fields of application. The development of a wide-angle magnetic spectrograph of a novel design, as described in this thesis, is a part of the possible realization of this goal. An important ingredient in this development was the application of techniques allowing the selection of important events from a background of a much larger number of events that are to be rejected. Such techniques have been developed for elementary particle physics in institutions like CERN. With the spectrograph provided with these additional techniques it would be indeed feasible to identify separately signals of elastically scattered or (mass-identified) recoiled ions, effectively summed over all charge states, angular resolved, and practically free of background. The analysis of the acquired energy spectra would allow the determination with nm depth resolution the concentration and lattice sites of both dilute heavy and light elements in crystalline samples over a depth range of 100 nm. The capabilities of ion beam analysis would be significantly increased beyond those already offered by MEIS or other existing spectrographs [14]. However, existing methods in use for the analysis of such data include some approximations which may introduce errors in the lattice site determination. To avoid the approximations, a new method of analysis by comparing with computer simulations is required. Such a method was developed in the CMAM, mainly by dr. V. Khodyrev. The second part of this thesis is devoted to the testing and application of the new computer program for simulations. The thesis is organized as follows:

In chapter 2 a review of the technique and (a simplified version of) underlying theories of ion-beam analysis is presented. It describes the possibilities and also the limitations of the various classes of methods as presently used. Also a brief overview of detection systems for the measurement of energy spectra of scattered and recoiled ions is presented. The optimum measuring geometry and the properties of a hypothetical "ideal" detector to be used for the detection of scattered or recoiled particles are discussed. Also the data analysis is reviewed, and the limitations of the energy and depth ranges, where the usual approximations involving single-scattering theory are allowed, are discussed.

In chapter 3 the design of a new type of magnetic spectrograph is presented. The various methods and computer programs used for designing a spectrograph magnet are discussed. The unique feature of the spectrograph consists of a system for the determination of the angle by which the ions enter the spectrograph and for the identification of the detected ion species. The position sensitive detectors used for the determination of the entrance angle, velocity and species of the ions are described, together with the electronic system. Details of the scheme for the multi-dimensional data analysis are given. Also the design of the rest of the hardware is described, including the support of

the magnet allowing measurements at five different scattering angles, the ultra-high vacuum system with the precision multi-axes goniometer and the sample introduction system.
It was the intention to write a separate chapter about the test results of the spectrograph. Instead, the first (positive) test results are included in this chapter, because the testing process was still in progress at the time of writing of this thesis. A main reason for the slow progress may be found in the size of the team working on the spectrograph, which is effectively limited to less than two full-time appointed persons. For comparison, at present two spectrographs of comparable complexity are in the testing phase [15,16]. These spectrographs, to be used for the separation of radioactive ions produced by a high-energy ion facility, are based on the same principle. A team of many physicists and technicians is working at each of these spectrographs.

In chapter 4 a new method of simulation of energy spectra of scattered or recoiled ions is presented. Like in all existing programs the simulations are carried out by the calculation of a large number (10^4-10^6) of ion trajectories, using the binary collision approach. Instead of random sampling, the method of sampling by importance of some of the random variables is followed. This gives rise to a large increase in the speed of computation of the spectra, even enabling the simulation of high-energy data. Until now, the latter would be impossible without approximations based on the single scattering model. Some examples of simulations are given in this chapter.

Chapter 5 deals with the analyses of data on the scattering of 2, 3 and 5 keV He ions from a clean Cu(100) surface. Azimuth and polar scans of the scattering intensity were measured at the University of Linz., Austria. Previously attempts to reproduce this data by simulations were not successful. To find the cause of the mismatch, in the present study the fast simulation program TRIC, discussed in the previous chapter, is used to simulate the scans with different shapes of the projectile-atom potential, with variations of the measuring geometry chosen within the assumed experimental uncertainties, and with different values for the relaxation of the top layers. Such a multi-parameter search for the best match between measured and simulated data concerning low-energy ion scattering would not be possible with any other simulation program than TRIC. Finally an almost perfect fit was obtained. The study shows that the accuracy of the measuring geometry is a very important factor, together with the interaction potential. This work, involving the simulation of thousands of energy spectra, also served as a testing ground for the program TRIC. The conclusion of this work is that low-energy ion scattering, in combination with the program TRIC, is a very powerful set of tools for studying the structure of near-surface layers of crystal surfaces. At the time of writing of this thesis such a capability is in the testing phase at the CMAM.

Since the work described in this thesis in still in progress, it would be too early for firm conclusions. However it is fair to say that, in case the magnetic spectrograph as described in this thesis would be working according to specifications, determinations as a function of depth on the nanometer scale of materials properties become possible that cannot be done with other existing methods. Analysis of the data by comparison with simulations should be done with the newly developed program TRIC to avoid approximations that may affect the reliability of the results. Ion beam analysis would thereby become an indispensable tool in nano-science and -technology.

It is clear that the work presented in this thesis is based on the efforts by many persons. It is a pleasure to thank the many people who contributed. Experimental physics projects are commonly carried out by a team of persons. In such a team friendship and good relations is of equal importance as knowledge and know-how. I was strongly supported by the CMAM team, also when I had to face a hard time. For me the work on this project is finished. I would like to thank those who continued with the project, thereby helping and supporting me to finish my PhD study.

I would like to thank Dirk Boerma, the director of my thesis, from whom everything started. He accepted me as his PhD student and he gave me great support which extended not only to science. He gave me this opportunity to participate in the large and innovative project, resulting in the work described in this thesis. His strong character was a good lesson to learn many things. He is also a very good person and he gave me lot of patience not only during explaining scientific things. Thank you, Dirk for your enthusiasm, which was the engine for this project. Thank you for all help which I received from you and all knowledge which I gained.
I would like to thank Vasily Khodyrev from the Moscow State University, who worked many times in the CMAM. I thank you for the interesting scientific conversations, new ideas and sharing with me your great passion for science, which had a big impact on me. From all conversation I see that the Russian spirit and the way of thinking is somehow similar to the Polish one.
Antonio Rivera my friend, I would like to thank you for all your help during difficult moments, for all our discussions, which were sometimes very intensive. You are a friend on which I can rely. I enjoyed the discussions about doing science.
Raquel Gonzales helped me with accommodation after my arrival to Madrid, she showed me the city, taught me all about UHV. Thank you for this and all the nice time spent.
Victor Joco and I became friends at first sight. It was really pleasure to do “free and crazy” science with you. I think during this period we came into “scientific resonance” doing all type of experiments. We had a lot of great brain-storm discussions together with Vasily in the “Cutre” bar. Thank you for all your colored and mystic stories about Rumania. Thank you for all nice time which we spent together.
Jose Emilio is a person which stays always calm. I had never seen him nervous. Thank you for being in the group which was struggling with bugs in the TRIC and other simulation programs.
Angel Guirao developed the electronics for the spectrograph. Thank you, Angel, for all discussions about electronics, computers and Spain.
Ramon Escobar is a new member of the surface group who agreed to continue my work on the spectrograph. We had no to much time to know each other better, I hope that you will enjoy working in CMAM.
Also I would like to thank the direction of the CMAM for all the support. I would like to thank Aurelio Climent for his lectures for PhD students, for help with all administration problems and being the peacemaker. Also I would like to thank David Martin for taking the effort of being my tutor. Fernando Agullo was the first director of the CMAM and I would like to acknowledge his support. Gaston Garcia was a person who explained me the first steps in ion optical calculations. Thank you, Gaston for this help and all the good organization related to the project.
Jorge Alvarez is a good IT specialist. Without his supervision of the computers I used, it would be impossible to finish all simulations on time. Thank you, Jorge. Also I want to thank you for all trips and your sense of humor.
Miguel Crespillo was my roommate and friend in the CMAM. He has a lot of passions, a great sense of humor and he knows amazing stories. Together we were doing different culinary experiments. Thank you Miguel for keeping me smiling. Thank you also for trips through Madrid lasting all the night.
Richard Smith was an “Englishman in Madrid”. Thank you for your friendship and English way of seeing things. Together we were discovering mysterious places in Madrid and in the surroundings.
I would like to thank secretaries of CMAM Beatriz Renes and Ana Granados, for all battles for me with Spanish administration.
Angel Munoz I don’t know how you are doing this, but you are always in a good humor, and ready to help other people. Thank you for all conversations, help and ideas.
Nuria Gordillo she was a good colleague during my studies. Thank you, Nuria for showing me a places and cities around the Madrid, introducing me to your friends and for all parties.
Thank you rest of the people of CMAM for all lunches, working and being together in one place for such long period. Thank you Olga Enguita, Carolina Gutierrez, Maria Dolores, Raul Gago, Jose

Olivares, Andres Redondo, Juan de la Figuera and Farid El Gabaly. Thank you, Martin Otto for your great sense of humor and making my stay in Madrid funnier. Also I would like to thank Antonio Rodrigez and Jaime Narros for all their technical work for the spectrograph.

Also a number of persons outside Madrid were supporting me. I would like to thank Marek Monet form Lodz the University for inviting me to do research at the Lodz University and for providing me access to accelerators in Lodz and Warsaw. He was a very good companion for discussions and mentor for doing different scientific activities.

Jerzy Czerbniak was the supervisor of my master thesis and a great promotor of my carrier. He was the person who initiated my interests in ions and ion collisions simulations.

During my stay in Poland I was sharing my working place with Adam Puszkarz. Thank you, Adam for good company.

Thank you, Valery Kuzmin from the Flerov Laboratory in Dubna, for your Hartree-Fock calculations.

I would like to thank prof. Peter Bauer from the Johannes Kepler University and Renata Kolarova for making available to me experimental results for my simulation work.

Finally I thank my mother for supporting me all the time and staying with me during difficult times. You always believed in me and you are the person which I can always trust.

References

1. S. Datz, T. S. Noggle, and C. D. Moak , Phys. Rev. 15 (1965) 254.
2. G. R. Piercy, F. Brown, J. A. Davies, and M. McCargo, Phys. Rev. 10 (1963) 339.
3. J. U. Andersen, J. A. Davies, K. O. Nielsen, S. L. Andersen, Nucl. Instr. and Meth. 138 (1965) 210.
4. G. Bonani, M. Suter, H. Jung, Ch. Stoller, W. Wölfli, Nucl. Instr. and Meth. 157 (1978) 55.
5. M.T. Robinson and O.S. Oen, Phys. Rev. 132 (1963) 2385.
6. R.B. Alexander, G. Dearnaley, D.V. Morgan, J.M. Poate, Physics Letters A 32 (1970) 365.
7. T. M. Buck, J. M. Poate, K. A. Pickar, C-M. Hsieh, Surface Science 35 (1973) 362.
8. J. F. Van Der Veen, R. G. Smeenk, R. M. Tromp, F. W. Saris, Surface Science 79 (1979) 219.
9. E.P. Gusev, H.C. Lu, E. Garfunkel, T. Gustafsson and M. Green, IBM J. Res. Develop. 43 (1999)265.
10. M. Copel, R. M. Tromp, Surface Science 337 (1995) L773.
11. P. D. Quinn, D. Brown, D. P. Woodruff, P. Bailey, T. C. Q. Noakes, Surface Science 511 (2002) 43.
12. D. W. Moon, H. I. Lee, Current Applied Physics 3 (2003) 45.
13. T. Kobayashi, Nucl. Instr. and Meth. B 249 (2006) 266.
14. G. Dollinger, A. Bergmaier, L. Goergens, P. Neumaier, W. Vandervorst, S. Jakschik, Nucl. Instr. and Meth. B 219 (2004) 333.
15. A. Cunsolo et al., Nucl. Instr. And Meth. A 484 (2002) 56.
16. H. Savajols, Nucl. Instr. And Meth. B 204 (2003) 146.

Chapter 2. ION BEAM ANALYSIS

2.1. Introduction

In Ion Beam Analysis (IBA) a sample is bombarded with ions that are accelerated to energies in the keV to MeV range. The beam size is typically ~1x1 mm and the beam intensity varies between 1 nA and ~100 nA. As a result of the bombardment various particles or radiations are emitted by the sample, like elastically scattered or recoiled particles, nuclear reaction particles or γ-rays (if the bombardment energy is in the MeV range), sputtered particles, electrons, X-rays, visible light, as illustrated in figs. 2.1 and 2.2. Here we only discuss the emission and detection of elastically scattered or recoiled particles.

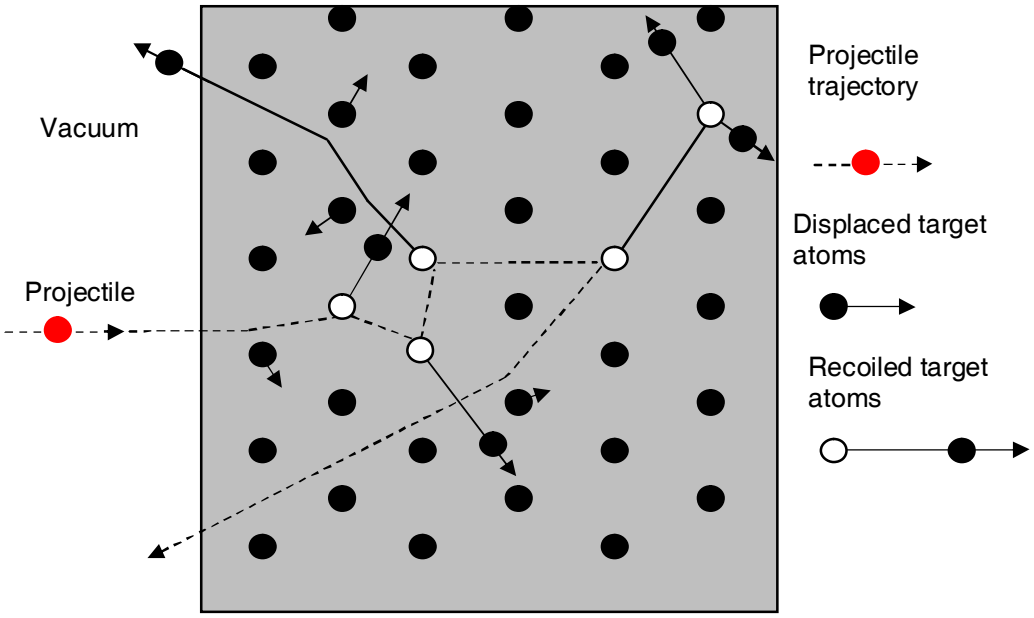

Fig. 2.1. *Schematic illustration of the interactions between a swift ion with target atoms occurring during penetration of a sample.*

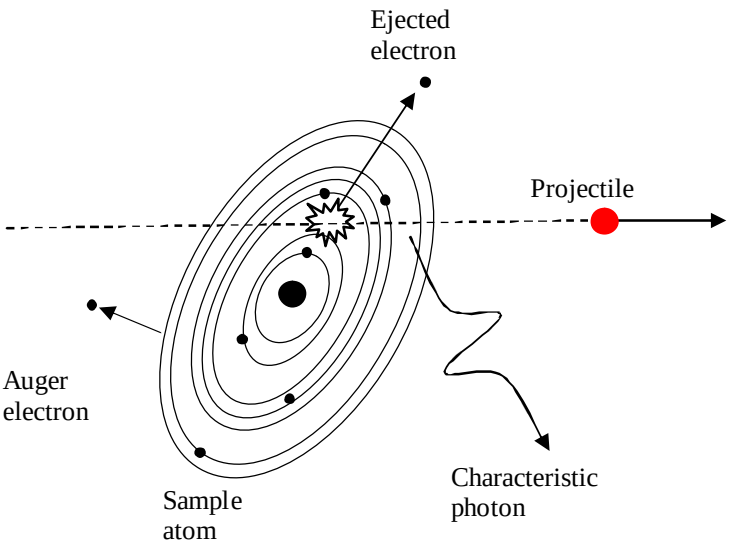

Fig. 2.2. *Types of emission during the projectile – target atom collision.*

The purpose of IBA [17,18,19,20] is to determine the element (or rather isotope) composition of the sample as a function of depth. No information on the chemical binding of these elements is obtained. The probing depth depends on the energy and species of the ion and it can vary from the nm to the μm range. If the sample is mono-crystalline, also depth dependent information on the structure can be obtained by measuring the scatter or recoil intensity as a function of the direction (with respect to the crystalline axes) of bombardment or detection. With this method, in principle, the position and the thermal vibration amplitude of each atom species in the crystal lattice can be determined. Also lattice strain can be detected as well as lattice damage.

In ion-solid interactions the ion as a whole is deflected by the ion-atom potential. This deflection is accompanied by electronic excitation. It is customary to treat the deflection and excitation as separate problems. This is a reasonable approach if the ion energy is in the keV range or higher, because the impulse transferred to electrons is only a small fraction of the total transferred impulse. For deflection angles of a degree or less of light ions the disentanglement of the deflection by the atomic potential and electronic excitations is not fully justified [21]. Also the energy lost in electronic excitations is ignored in the calculation of the deflection angle. Still, to very good approximation, the deflections of an ion propagating in a solid are treated as elastic collisions with isolated atoms. The binding energy of the atom in the solid (~5 eV) is neglected. The deflection is calculated using a classical (versus quantum mechanical) approximation. Also this is a good approximation for ions with energies in the keV to MeV range [5].

2.2. Kinematics

As mentioned above, the collision of a projectile with a target atom can be described in terms of an elastic collision between two nuclei. The fraction of the energy transferred from the projectile to the target atom can be calculated from the laws of conservation of energy and momentum. The collision between two particles is illustrated in fig. 2.3. A projectile with mass M_1 and energy E_0 is colliding with a target atom with mass M_2. After the collision, the projectile has energy E_1 and it is scattered at an angle θ with respect to the direction of incoming beam. The target atom recoils with energy E_2 at an angle ξ with respect to the direction of incoming beam. The ratio between the energy of the particles after the collision to the energy before the collision is given by kinematic factors $K_{1,2}$. The formulas for the kinematic factors are given in fig. 2.3. The positive sign in the first formula holds when $\mu = M_2/M_1 > 1$. For $\mu < 1$ both the + and – signs apply.

$$E_1 = K_1 E_0 = \left[\frac{M_1 \cos\theta \pm \left(M_2^2 - M_1^2 \sin^2\theta\right)^{1/2}}{M_1 + M_2} \right] E_0 \quad (2.1)$$

$$E_2 = K_2 E_0 = 4 \frac{M_1 M_2}{(M_1 + M_2)^2} \cos^2 \xi \quad E_0 \quad (2.2)$$

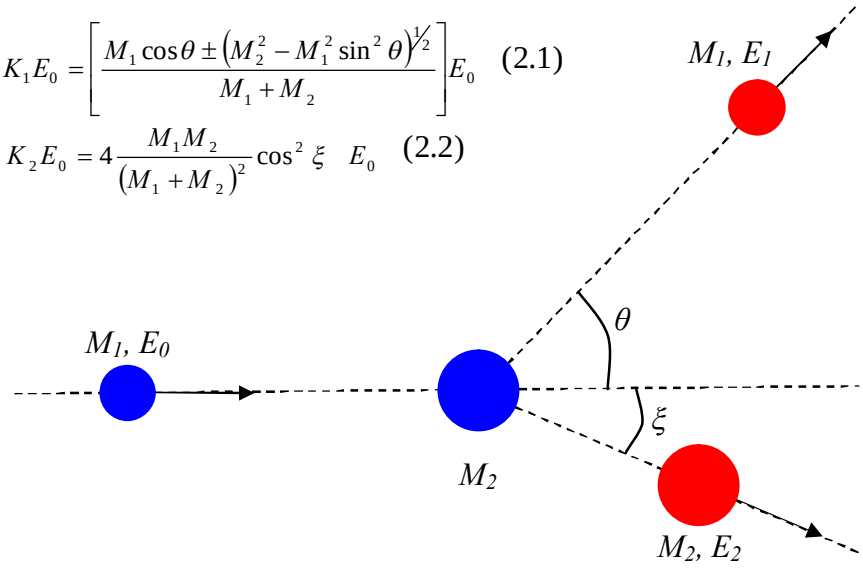

Fig. 2.3. *A schematic representation of a scattering event in the laboratory reference frame. A blue colour indicates particles before the collision and a red colour indicates particles after the collision.*

It is important to note the following peculiarities of elastic collisions:

- Elastic recoiling is only possible in forward directions ($\xi < 90^o$).
- For $\mu > 1$, scattering can occur to all directions ($0 < \theta < 180^o$)
- For $\mu < 1$ scattering is only possible to forward angles $< \theta^*$, with $\theta^* = \arcsin(\mu)$. Within this forward scattering cone, and at a fixed angle θ, two energies of the scattered particle occur, as given by the formula in fig. 2.3.
- For $\mu > 1$ the mass dispersion dE_1/dM_2 increases with E_0 and with the scattering angle θ.

We note that for $\mu < 1$ an angular range $\theta < \theta^* < 90^o$ exists in which only direct recoiling can be observed and no scattering. In ERD with heavy ions the detection angle is usually chosen within this range. Alternatively, for $\mu > 1$, an angular range $90^o < \theta < 180^o$ exists in which only direct scattering can be observed. For this reason RBS is usually done with light ions with the detector at a backward angle. These points are illustrated in fig. 2.4.

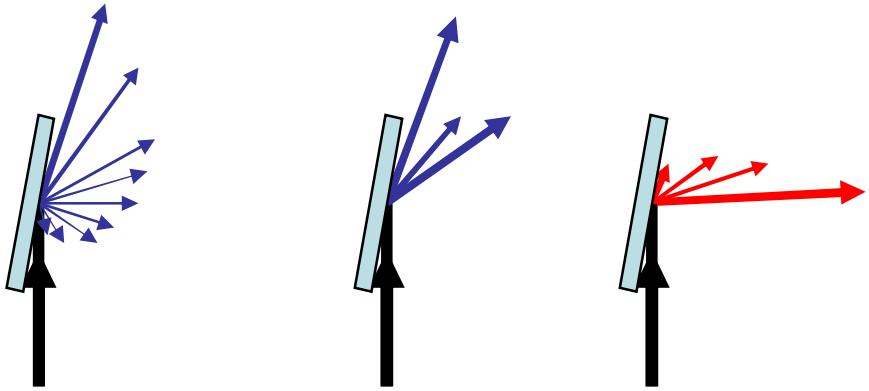

RBS M1<M2 **RBS M1>M2** **ERD M1≦ M2**

Fig. 2.4. *Schematic distribution of ions emitted from the sample upon radiation. The black arrows indicate the ion beam; the blue arrows indicate scattered particles, red arrows indicate recoiled particles. The intensity distribution is schematically indicated by the length of the arrows.*

In the centre of mass (CM) system the cross section for scattering can be derived from the dependence of the scattering angle Φ on the impact parameter b:

$$\sigma(\phi) = \frac{b}{\sin\phi}\left|\frac{db}{d\phi}\right| \qquad (2.3)$$

In the laboratory system (LS) the cross section is:

$$\sigma(\Theta) = \sigma(\phi)\frac{\sin\phi}{\sin\Theta}\left|\frac{d\phi}{d\Theta}\right| = \sigma(\Theta) = \sigma(\phi).F(\phi,\mu) \qquad (2.4)$$

$$F(\phi,\mu) = \left|\frac{\mu}{\mu+\cos\phi}\left(1+2/\mu\cos\phi+1/\mu^2\right)^{3/2}\right| \qquad (2.5)$$

If $\mu < 1$, $F(\Phi,\mu)$ is singular for $\Phi=\Phi^*$, with Φ^* = *arcos* $(-\mu)$, or $\Theta=$ arcsin(μ). This singularity is indicated schematically in fig. 2.4. The function $F(\Phi,\mu)$ is plotted in fig. 2.5. Similarly we get for the cross section in the LS for recoiling:

$$\sigma(\xi) = \sigma(\phi)G(\phi) \quad (2.6)$$

with $G(\phi) = 4\sin\frac{1}{2}\phi$

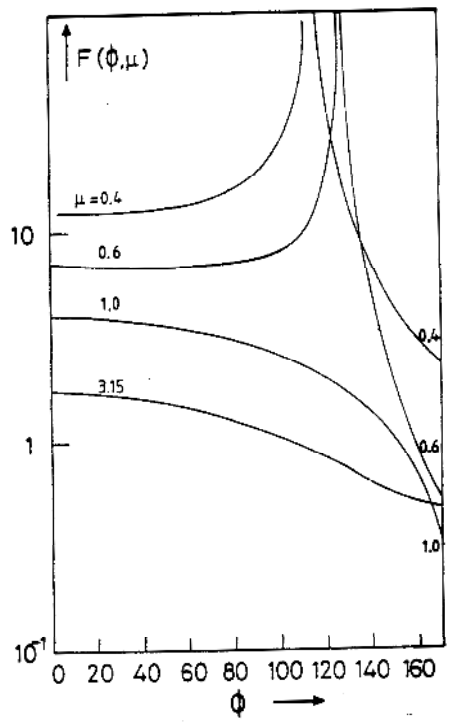

Fig. 2.5. *The function F(Φ,μ) plotted as a function of Φ for the different values of μ. For μ < 1 there is a singularity.*

2.3.1. Energy loss and electronic excitations

When ions are propagating in a solid, they are losing kinetic energy due to nuclear collisions and electron excitations. Since the energy loss is a statistical process, the energy loss of ions passing through a thin layer will be spread around an average value. The energy loss processes will also cause angular deflections, giving rise to angular straggling. Theoretical models have been developed to predict the average energy loss, the energy straggling and the angular straggling.

The stopping force is defined as the energy loss per unit length: $S=dE/dx$. Another way to define the energy loss is by the stopping cross section $\varepsilon=(1/N)(dE/dx)$, where N is the particle density. As mentioned before, for energies in the range keV/amu – few MeV/amu, the interaction of an ion with atoms in a solid can be split into nuclear and electronic interactions. For this reason the stopping force is divided into the electronic $S_e(E)$ and nuclear $S_n(E)$ stopping forces [21]. The total is then given by:

$$\frac{dE}{dx} = S_n(E) + S_e(E) \quad (2.7)$$

2.3.2. The nuclear energy loss

The nuclear energy loss is due to elastic collisions between the projectile and atoms in the medium. The nuclear energy loss is dominant for ions with low energy as shown in fig. 2.6. If the interaction potential $V(r)$ between the ion and the atoms of the medium is known, it is possible to calculate the nuclear energy loss $S_n(E)$, as well as the nuclear energy- and angular-straggling. The interaction potential will be discussed later. Assuming that the interaction can be described by the Coulomb potential, the following expressions can be derived:

$$\left[\frac{dE}{dx}\right]_n = 8\pi N \frac{M_1 C^2}{M_2 E} \ln \frac{2a_{12} M_2 E}{C(M_1 + M_2)} \quad (2.8)$$

$$C = KZ_1 Z_2 e^2 \quad (2.9)$$

where a_{12} is a screening radius. K is the constant in the Coulomb potential in the MKgS system = 9 x 10^9 Nm^2C^{-2} ($K = 1/4\ \pi\varepsilon_0$). Note that the energy dependence of the stopping force is ln(E)/E.

For more precise calculations the universal nuclear stopping force is used, in which the screening of the potential by electrons is taken into account [21]. The corresponding formulas can be found in [22].

The nuclear energy loss straggling is given by:

$$\sigma_n^2 = \frac{4\pi C^2 M_1^2}{(M_1 + M_2)^2} \Delta R \quad (2.10)$$

where ΔR is the layer thickness. This straggling is independent of the energy.

The angular straggling $\overline{\psi}_n^2$ is given by:

$$\overline{\psi}_n^2 = \frac{M_2}{M_1} \frac{\overline{\Delta E}}{E_0} \quad (2.11)$$

This formula can be used to estimate the depth within which the single scattering theory is applicable.

2.3.3. Electronic energy loss and excitations

During the propagation of an ion in a solid, electrons of the solid and of the ion (if present) are constantly excited and de-excited. In this process kinetic energy of the ion is transferred to the solid, giving rise to the so-called electronic energy loss. When electrons bound to the ion are excited to the continuum, obviously the ion charge state changes. Also electrons from the solid may be captured by the ion. At ion energies where the ion is not fully stripped of all its electrons, this process of electron capture and loss gives rise to a fluctuating charge state of the ion. Up to now no ab-initio calculations of the processes mentioned have been carried out, with the exception of the most simple cases, like the energy loss and charge exchange of H or He ions [22,24,25,26,27,28,29,30,31,32,33,34,35].

A simple estimate of the average charge state of the ion (due to Bohr) is that electrons are stripped from an ion whenever the velocity v_0 of the ion exceeds that of the electrons v_e, in the different shells. If $v_0 < v_e$ for a certain electron shell of the ion, an electron will be captured into this shell, and vice-versa. This model was refined later in the work of [26], by a different way to calculate the electron velocities in an ion.

Based on this simple theory the following empirical formula for the effective charge Z* of the ion was obtained [36,37]

$$Z^* = Z_1\left(1 - \exp\left[-v_0 / v_e \delta Z_1^{2/3}\right]\right) \quad (2.12)$$

Here v_e is the Bohr velocity and δ is a constant ≈ 0.8.

In the discussion of the electronic energy loss it is important to note that for bare ions the interaction of an ion with electrons can be divided into two groups, the distant resonance collisions and the close collisions with large momentum transfer to electrons. The resonance collision can be simplified in a model where the atom electrons are promoted to an excited state by the interaction with the transient electro-magnetic field of the ion passing by. For the close collisions the interaction may be considered as a scattering process governed by the Coulomb potential, whereby the electron is promoted to the continuum. At not too low ion velocities (as compared to the velocities of the electrons of the atoms) both contributions to the energy loss are of approximately equal magnitude.

In the simple Bethe-Bloch approach the energy loss for bare ions at energies where $v >> \bar{v}_e$ can be written as:

$$\left[\frac{dE}{dx}\right]_e = \frac{4\pi\, N K^2 Z_1^2 Z_2 e^4}{m_e v_0^2} \ln\left[\frac{2 m_e v_0^2}{I}\right] \quad (2.13)$$

where N is the number of atoms per unit volume, I≈10eV is the average excitation energy of the atomic electrons and v_0 is the ion velocity. For somewhat smaller velocities one may replace Z_1 by Z_1* to obtain a rough description of the energy loss in cases where the ion is not fully stripped of all its electrons. Here Z_1* is the effective charge of the ion as given by eq. 2.12. The dependence of the stopping on the energy E of the ion is again $\ln(E)/E$. The energy dependence is depicted in fig. 2.16. The same theory yields a formula for the energy straggling, known as the Bohr straggling:

$$\sigma_e^2 \approx 4\pi\, K^2 Z_1^2 Z_2 e^4 N \Delta R \quad (2.14)$$

It is known [1**¡Error! No se encuentra el origen de la referencia.**] that the Bohr straggling is a slight overestimate.

The angular straggling $\overline{\psi}_e^2$ is given by:

$$\overline{\psi}_e^2 = \frac{M_e}{M_1}\frac{\overline{\Delta E}}{E_0} \quad (2.15)$$

At low energies, where v<< v_e, the energy loss is proportional to the velocity v to good approximation. Theoretical models predicting this dependence are based on the promotion of electrons of the atom and the ion to excited states of a quasi molecule formed during the collision. One of these models is the *LSS* (Lindhard, Schiott, Scharff) model [39]. The resulting $\sqrt{E}$ dependence is also depicted in fig. 2.6. Here it is not straightforward to derive formulas for the straggling. This straggling in the electronic energy loss can be ignored with respect to the nuclear straggling, which is larger by orders of magnitude. The stopping force by the LSS theory, using a Thomas-Fermi atomic model, is given by:

$$\left[\frac{dE}{dx}\right]_e = -\zeta_e \cdot 8\pi e^2 N a_0 Z_1 Z_2 \left(Z_1^{2/3} + Z_2^{2/3}\right)^{-3/2} \cdot v/v_0 \quad (2.16)$$

where a_0 is the Bohr radius, v_0 the Bohr velocity and ζ_e a dimensionless constant of the order $Z_1^{2/6}$.

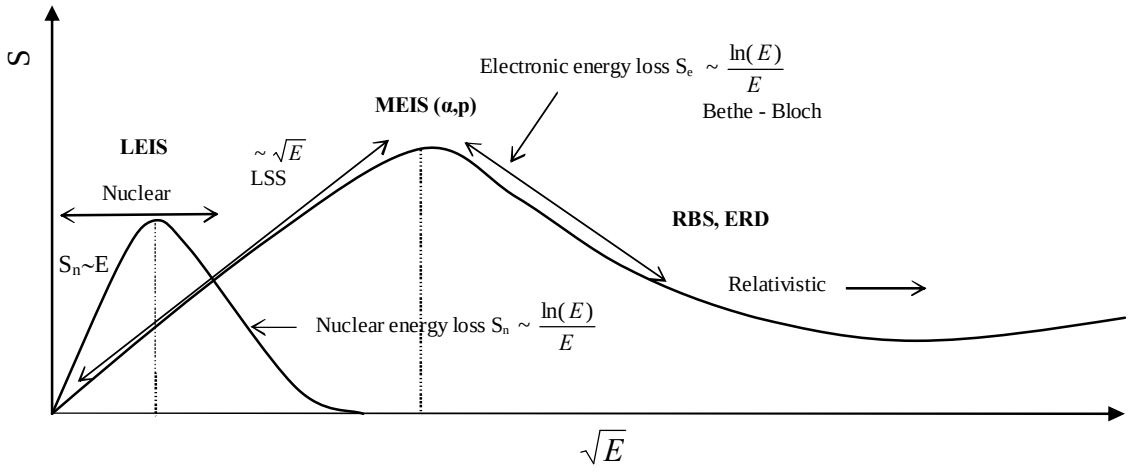

Fig. 2.6. *Global dependence of S_n en S_e on the square root of the energy. The increase of the electronic stopping at very high energies is mainly due to relativistic effects and nuclear excitations According to the Bethe Bloch formula the energy dependence is ln(E)/E, a function that has a maximum similar to the maximum in the curve.*

The energy dependence of the electronic and nuclear stopping forces is illustrated in fig. 2.6. As can be seen, in the energy regime for RBS or ERD the electronic energy loss dominates. By taking the ratio of the formulas for the electronic and nuclear stopping forces for high energies, one can estimate that at high energies the nuclear stopping is only a few percents of the electronic stopping.

Until now only the interaction of ions with mono-atomic media was considered. To obtain the energy losses for molecular media, the Bragg rule may be applied to first approximation. This rule implies that energy loss in compounds can be estimated assuming that interaction processes

between ions and component target atoms are independent of the electron configuration. According to Bragg's rule the stopping forces can be added linearly as a first approximation:

$$S(E) = -\frac{dE}{dx}(E) = \sum_{i=1}^{K} n_i x_i \varepsilon_i \quad (2.17)$$

where k is the number of different components, x_i their relative number fraction, ε_i their specific stopping force per atomic number and n_i the overall number of atoms per unit volume. The stopping forces of the elements are well tabulated and there are semi-empirical approximation formulas for almost all ions available.

The Bragg rule formula is a reasonable approximation for projectile energies much above the maximum of the stopping force. Since the electronic stopping forces depend on the configuration of the electrons in the stopping media, the Bragg rule is only approximately valid. Corrections to the Bragg rule can be as large as 10-20% for solid compounds containing heavy and light constituents, such as oxides and nitrides. In organic compounds deviations up to 50% are observed [40]. Phenomenological models were developed taking into account chemical-state effects, for example by [41].

In the above description of the energy loss the dependence on the impact parameter is not included. This means that the stopping is averaged over all impact parameters of the ion-solid interactions. It is trivial to obtain the impact parameter dependence of the nuclear stopping from a description of the ion trajectories in a solid in terms of binary collisions. Only a few models exist that predict the impact-parameter dependence of the electronic stopping. A rough estimate is that the close-collision part of the electronic stopping scales with the local electron density, and that the distant collision part does not depend on the impact parameter.

A more advanced theoretical approach was used in the program CasP [42] by Grande, and Schiwietz. This program makes fast numerical calculations of the electronic energy transfer Q_e (due to excitation and ionization of target atoms) as a function of the impact parameter b in a collision. By selecting a proper screening function, it is possible to treat the energy loss for different charge states of the ion. The physical inputs of the program are the projectile velocity, the projectile-screening potential, the target-electron density distribution (tabulated output of Hartree-Fock-Slater model calculations) and the oscillator strengths for the target electrons.

2.4.1. Rutherford backscattering spectroscopy (RBS) and elastic recoil detection (ERD)

The most widely used techniques in ion beam analysis are RBS and ERD for the determination of the composition of a sample as a function of depth. Together these techniques are known as high-energy ion scattering (HEIS). The reasons for its wide-spread use are clear: the experimental set-up can be simple, the running time for a typical experiment is relatively short, the analysis of the results is relatively straightforward, but above all, the information about the elemental composition is obtained as a function of depth in a single measurement.

The physical concepts governing RBS and ERD are identical. In both cases a sample is bombarded with ions with energy in the range of about 0.2-10 MeV/amu. The ion beams are usually generated by an electrostatic accelerator such as a (tandem) Van de Graaff accelerator with a very low energy spread ($\Delta E/E < 10^{-4}$) of the beam. In RBS the energy spectrum of elastically scattered ions is measured and in ERD that of elastically recoiled atoms emerging from the sample. The energy spectra measured in RBS or ERD carry information about the composition of the sample as a function of probing depth. The principle is illustrated in fig. 2.7.

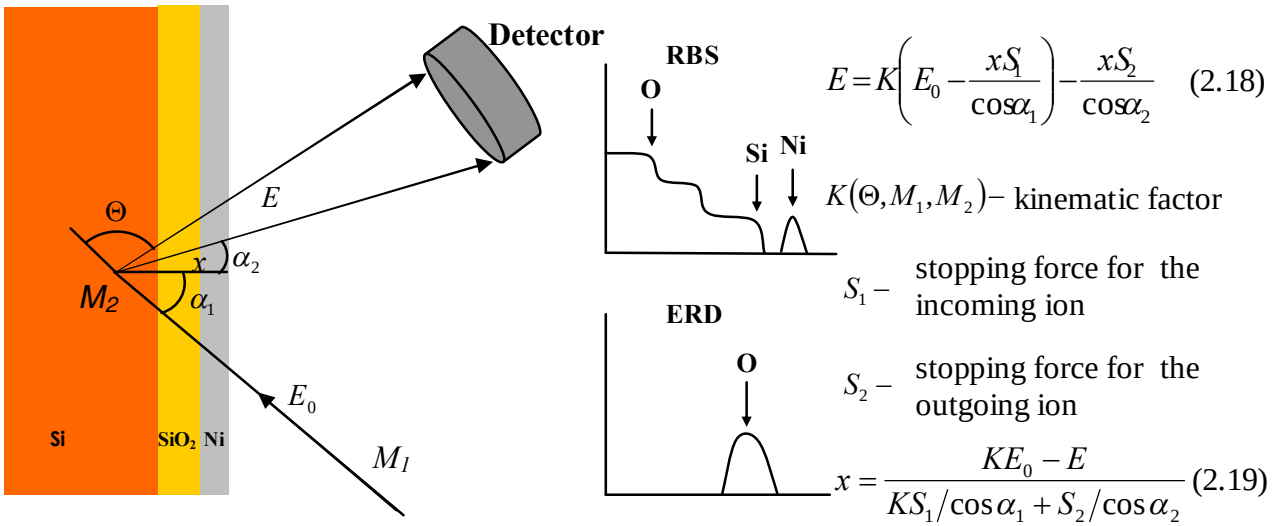

Fig. 2.7. *A schematic outline of RBS and ERD-depth profiling. See text for details.*

The energy of an ion scattered or recoiled over a given angle from the surface layer is given by the kinematics. Since these energies depend on the mass of the atom in the sample on which the collision took place, the composition of (the surface layer of) the sample can be derived from the energy spectrum. When the scattering or recoiling takes place in deeper layers, the energy of scattered or recoiled particles is also determined by the energy loss on the ingoing and outgoing trajectories. To relate the measured energies with depth, it is crucial to assume that single scattering theory is applicable. This assumption implies that each measured ion emerging from the sample has undergone only one major collision and that the trajectories to and from this collision point are straight lines. Effects of (small-angle) multiple scattering are ignored or treated as a perturbation to the idealized picture. Further on we will see that single scattering theory can be applied to good approximation for the ion energies specified above and for a limited penetration depth of the ion.

If single scattering theory is applicable, the energy scale of the spectrum can be translated into a depth scale using formula 2.19 in fig. 2.7. It is important to note that this step implies another assumption, namely that the energy loss along the trajectory is equal to the energy loss per unit length averaged over the impact parameter. As we will see later, this is not the case if the trajectory is in a mono-crystal close to a crystal axis or plane. For the translation of the depth- to energy-scale

it is required that the ion moves in a material without order, i.e. in an amorphous material. In practice the translation can also applied for fine-grained poly-crystalline materials and even, as an approximation, for mono-crystalline materials if the ion trajectories are in a "random" direction (not close to crystal axes or planes). The depth resolution Δx is proportional to the energy resolution. This resolution ΔE is given by the detector resolution. At larger depth x (x>5nm) the straggling in the energy loss becomes an important factor. The yield from different elements can be derived from the energy spectrum of the scattered or recoiled ions. To translate the yield into a concentration the cross sections for scattering and the detection efficiency should be known. The cross sections can in good approximation be calculated with the Rutherford formula. Some corrections of the order of a few percent may be applied to take into account the screening of the Coulomb potential by electrons [17,18,22]. The detector efficiency follows from calibration measurements. For a commonly used Si-diode detector the detector efficiency is unity. In case the concentration must be determined on an absolute scale, also the beam fluence should be measured. In most cases it is sufficient to determine the concentrations on a relative scale.

In case single scattering theory holds and for media with a "random" distribution of the atom positions, the channel content N_{chan} as measured with an analogue-to-digital converter (ADC) can be calculated as a function of energy as:

$$N_{chan}(E) = N_{ion}\,\varepsilon\,d\Omega\,\sigma(E')N\Delta x \quad (2.20)$$

Here E is the energy corresponding to the channel number, N_{ion} is the total number of ions used for the bombardment of the sample, ε is the detector efficiency, $d\Omega$ is the solid angle of the detector, $\sigma(E')$ is the cross section for the energy E' at which the scattering took place:

$$E' = (E + S_2 x/\cos\alpha_2)/K \quad (2.21)$$

The number of atoms per m^2 is $N\Delta x$, with N the atomic density and Δx the length interval corresponding to the channel width in the spectrum. This channel width ΔE is determined by the energy calibration. With equation (2.19) the quantities Δx and ΔE can be related.

The spectrum thus calculated must be folded with the detector resolution and possibly with the energy spread due to straggling. Then it precisely reproduces a measured spectrum in the energy range where single scattering theory is applicable. This procedure can be used to calculate spectra for trial compositions of the sample. In this way the composition of a sample can be determined from a measured spectrum by comparing measured and calculated spectra. Several programs exist for the analysis of RBS (and also ERD) spectra based on this approach: GISA [43], RUMP [44], RBX [45], DEPTH [46], DataFurnace (NDF) [47], SIMNRA [48], MCERD [49].

The probing depth depends on the energy and species of the ions used as projectile and the observed ions, on the geometry of the measurement and, to a smaller extent, on the composition of the sample. Depending on these parameters, the maximum probing depth may vary between roughly 10 and 5000 nm. The maximum probing depth is achieved for RBS with protons with energy of 3 MeV or more.

In a RBS experiment the detector is usually placed at an angle larger than 90° with respect to the beam direction; then mainly backscattered projectiles are detected. Mainly H or He ions are used for RBS. The technique is well suited for the detection of heavy elements in a matrix of lighter elements, because the signal of heavier elements appears at the high-energy part of the spectrum and can be well distinguished from the signal of the matrix. The reverse is true for the measurement of light elements in a heavier matrix. Because the signal of light elements is not separated from the bulk and because of the low cross section of light elements for backscattering, RBS is a less suitable technique for this purpose.

In ERD experiments, the detector is placed at an angle smaller than 90° with respect to the beam direction and commonly heavy ions are used as projectiles. The typical heavy particles used in ERD are Ar, Cu, Ag, I, or Au. The detection of scattered ions from the incident ion beam is normally suppressed in order to avoid background. The easiest and most common method is the use of a foil, which stops the scattered ions, but allows the passing of the lighter recoils, which have a lower stopping power. ERD with heavy projectiles is mainly used for depth profiling of light elements ($Z \leq 10$). The great advantage of ERD over RBS is that all the atom species of the sample are recoiled if an energetic incident beam is used, so a complete analysis of the sample is immediately obtained if a detector separating the observed ion species would be available. From the measured energy spectrum of the recoiled ions a concentration depth profile can be calculated in the same fashion as described for RBS.

2.4.2. Applicability of single scattering theory

As stated above, single scattering theory implies that each measured ion emerging from the sample has undergone only one major collision and that the trajectories to and from this collision are straight lines. In reality ions on the ingoing and outgoing path suffer many small angle deflections with small scattering angles. This is called multiple scattering. Additionally ions may undergo more than one scattering event with large scattering angle, before they are scattered towards the detector. This plural scattering is supposed to be a minor effect in RBS and ERD analysis.

Multiple scattering results in an angular spread of the particles what causes a spread of path lengths and angle of scattering of the main scattering event; see figs. 2.8.a. and 2.8.b.

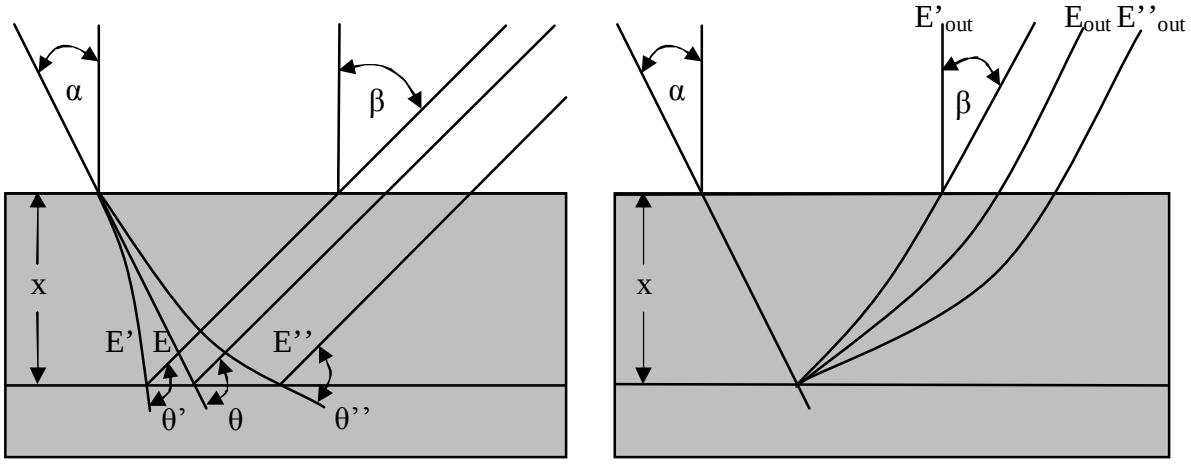

Fig. 2.8. *Contributions of multiple scattering on the ingoing path (a) and contributions of multiple scattering on the outgoing path (b).*

In fig. 2.9. the scattering angle is plotted as a function of impact parameter for collisions of 6 keV Ne ions, and of 2 MeV He ions, both with Cu. The angle is calculated with the Molière approximation for the Ne-Cu inter-atomic potential and with the Coulomb potential for the He-Cu interaction. In the graph the scattering angle for the He-Cu collisions is multiplied by a factor of 100.

For Ne-Cu collisions with an impact parameter b = 0.5 Å the scattering angle is 8°. On average a Cu atom in an atomic layer occupies 5.2 $Å^2$. Each Ne-ion propagating within a distance of 0.5 Å from a Cu-atom –this is 15% of the Ne ions- is deflected by more than 8°. This example

illustrates that a Ne-ion describes a zigzag trajectory through Cu, and that a main fraction of the energy will be lost in "nuclear collisions". For He-Cu at 2 MeV the deflection is only 2.3° for an impact parameter b = 0.01 Å. For 1 in 1.7 x 10^4 He-ions the deflection is 2.3° or more.

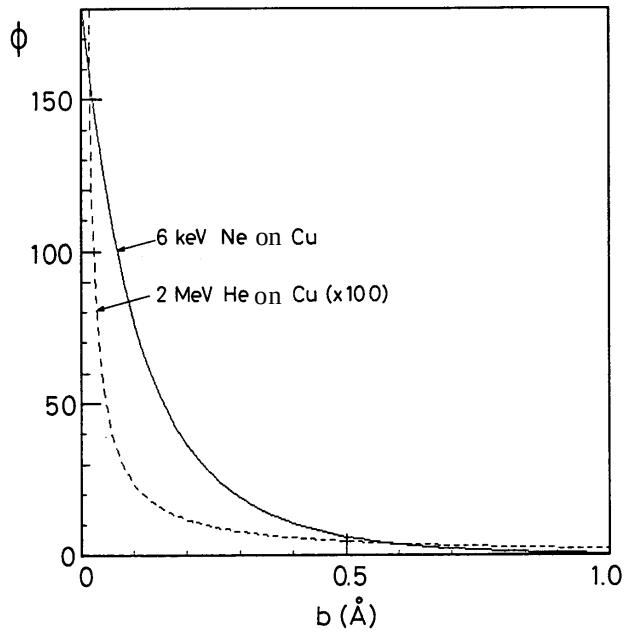

Fig. 2.9. *The scattering angle (cm) as a function of impact parameter for scattering of 6 keV Ne ions and 2 MeV He ions from Cu. Note that the angle for He-Cu collisions has been multiplied by a factor of 100.*

This example illustrates that single scattering theory cannot be applied for low energy ion scattering. To estimate when this approach can be applied for higher energies, we calculate the depth where the angular straggling due to nuclear collisions of an ion scattered at this depth and re-emerging to the surface is equal to a (pre-defined) value. Taking (as an example) a value of 2º, we find as a function of ion species and energy the probing depth within which single scattering theory may be used for RBS as an approximation (see fig. 2.10.).

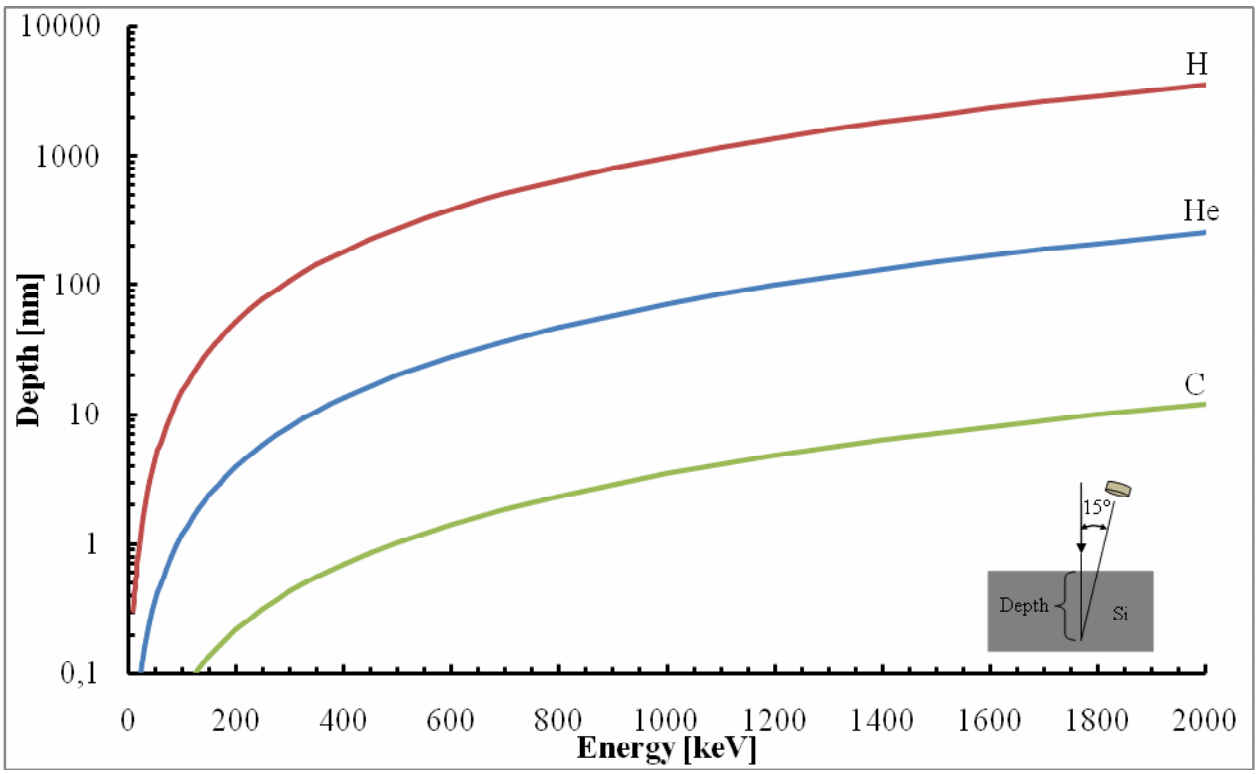

Fig. 2.10. *Depth as a function of energy at which the angular straggling due to nuclear collisions, as calculated with eq. 2.11, is equal to 2°. The curves are calculated for a RBS geometry as indicated for H-, He- and C- ions on Si.*

2.4.3. Medium-energy ion scattering

In medium-energy ion scattering (MEIS) typically protons with an energy between 50 and 100 keV or He ions with an energy between 100 and 200 keV are used as projectiles. At these energies the electronic stopping has a (broad) maximum (see fig. 2.6.). Usually an electrostatic analyzer is used for the detection of the scattered ions with good energy resolution ($\Delta E/E \sim 5 \times 10^{-4}$). In its focal plane often a 2D position sensitive detector is used to cover a certain energy range and a wide detection angle (up to 20º) [50,51].

The method is used to probe surfaces or thin (< 5 nm) top layers of samples to get information on the composition and structure. In such thin layers single-scattering theory can still be used to good approximation. For the relevant range of energies more than 90% of the scattered He or H atoms are singly charged.

2.4.4. Low-energy ion scattering

In low-energy ion scattering (LEIS) mostly noble gas ions (He, Ne, Ar) with energies of 1-10 keV are used to probe the composition and the structure of the outer layers of a (mono-crystalline) sample [52].

The ions have zigzag trajectories at these low energies. For glancing-angle (~10º) incidence of the beam or for glancing detector angles the major part of the observed scattering or recoiling events is from the first one or two layers below the surface. Particles coming from deeper layers cause a low "background" at the low energy side of a peak due to scattering/recoiling from the first few layers. A second peculiarity of low-energy ion scattering is that a main fraction of scattered or recoiled ions pick up an electron at the moment they enter or leave the sample, i.e. near the surface. In general a fraction of > 95% of noble-gas ions gets neutralized in this way. The small charged

fraction is practically exclusively due to scattering from the outer layer. This fact is exploited to probe the composition of surfaces with an electrostatic analyser [53]. For atoms with a loosely bound electron, like alkali atoms, the ionized fraction is much larger (~30%). For this reason often Na- K- or Cs- ions are used in LEIS when an electrostatic analyzer is used to detect the scattered ions. When noble gas ions are used, the time-of flight technique (ToF) is commonly used to determine the velocity of the scattered or recoiled atoms as is illustrated in fig. 2.11.

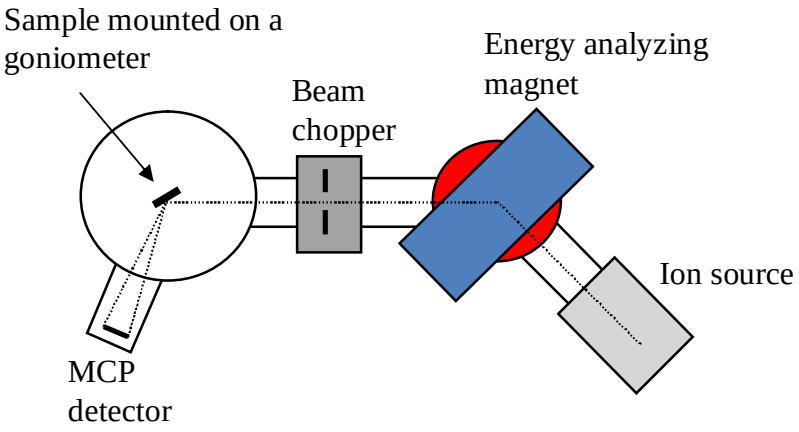

Fig. 2.11. *A typical experimental configuration for LEIS -ToF.*

2.4.5. Measurement of atom positions in mono-crystalline layers

When ions propagate in a crystal, the flux density and, therefore, the chance for a close encounter of an ion with atoms in the crystal, is not uniform as is the case in amorphous materials. The redistribution of flux is due to shadowing, blocking, or channelling, depending on the situation. This is related with the fact that for a certain crystallographic direction, charged particle can move in the open spaces (channels) between close packed rows or planes of atoms in a crystal.

In fig. 2.12. a computer simulation is shown of the change of the ion flux density in an initially uniform ion beam, entering a Si lattice parallel to strings of atoms (i.e. entering along a major crystal axis). In fig. 2.12.a. the ion trajectories have been calculated in a lattice without thermal vibrations; in fig. 2.12.b. the thermal vibrations have been included. As can be seen, a shadow cone forms behind each surface atom. Due to thermal vibrations the shadow cone gets somewhat blurred. The flux density near the centre of the space between rows of atoms increases, whereas the flux density near the rows diminishes. This effect is called shadowing.

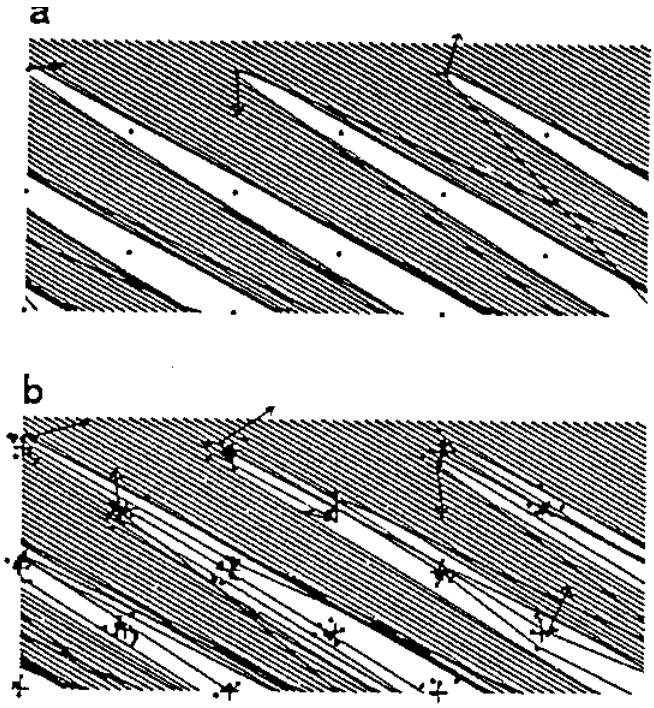

Fig. 2.12. *Calculated trajectories of 100 keV protons for parallel incidence in a crystalline direction of Si. A screened Coulomb potential was used in the calculations. In the top part (a) the lattice is rigid, i.e. no thermal vibrations are taken into account. In the bottom part (b) vibrations calculated for room temperature are taken into account [54].*

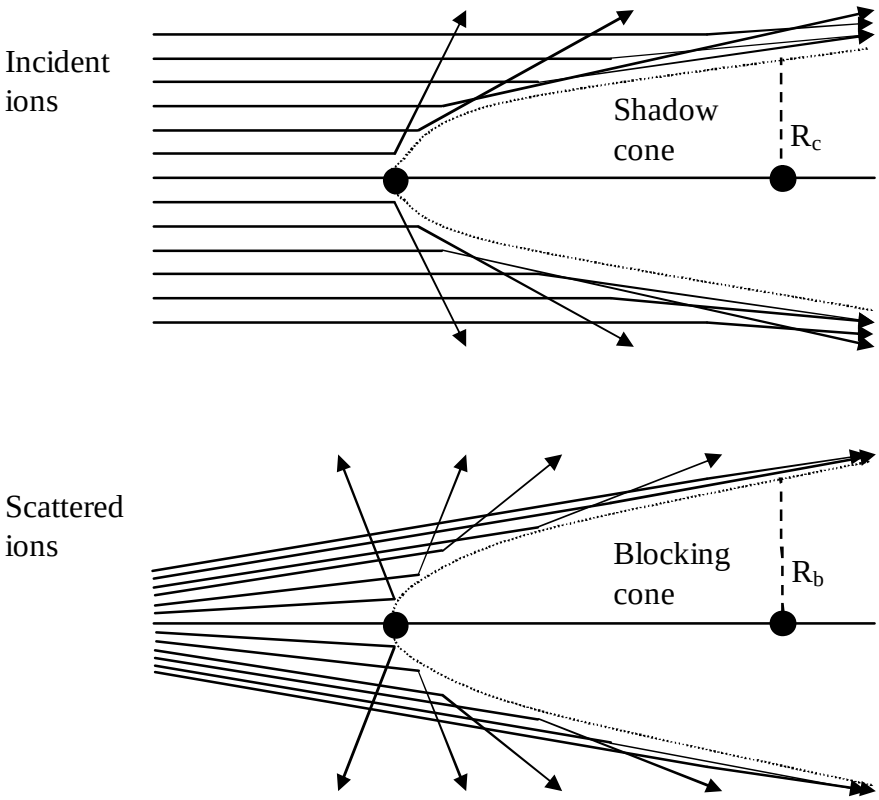

Pic. 2.13. *Formation of a shadow- and a blocking cone, respectively. A shadow cone appears behind each (surface) atom bombarded by ions. R is the radius of the cone at the position of the next atom. A blocking cone is formed behind atoms close to the trajectories of ions scattered from a previous atom.*

Processes similar to shadowing occur when an ion is scattered from an atom of the lattice, or when an atom of the lattice is recoiled. Blocking cones are formed in the direction of atom strings, as illustrated in fig. 2.13. The rate of scattering/recoiling as observed with a detector with a small opening angle will be strongly diminished due to blocking for detection angles coinciding with atom strings. First we derive an expression for the width of the shadow cone assuming a Coulomb potential. A similar expression can be used for the width of the blocking cone. In fig. 2.13. the formation of channelling and blocking cones is illustrated.

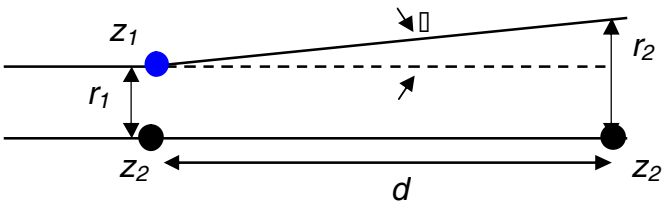

Fig. 2.14. *Schematic presentation of an ion trajectory, whereby the ion is incident parallel to the line connecting two atoms. The deflection is by the first atom. The second atom lies in the shadow cone of the first atom.*

In fig. 2.14. a trajectory of an ion with charge Z_1 is indicated schematically. The ion is incident parallel to the line connecting the two atoms, and is deflected over a small angle by an atom with charge number Z_2. It then passes a second atom at a distance d from the first atom. The

distances of the ion trajectory to the first and the second atom are r_1 and r_2, respectively. The value of r_2 as a function of r_1 for the Coulomb potential is:

$r_2 = r_1 + \frac{Z_1 Z_2 e^2 Kd}{E_0 r_1}$ (2.22), with a minimum for $\frac{dr_2}{dr_1} = 0$ equal to:

$$r_{2\min} = R_c = 2\sqrt{\frac{Z_1 Z_2 e^2 Kd}{E_0}} \quad (2.23)$$

Here $r_{2min} = R_c$ is the radius of the shadow cone at a distance d from the top of the atom. For a screened potential the value of R_c would be smaller by up to a factor of 2 for energies in the keV region. The half-opening angle of the cone for an inter-atomic distance is $\psi_{1/2} = R_c / d$. Structure determinations with MEIS or LEIS are based on the formation of shadowing and blocking cones. The yield for scattering or recoiling at the edges of these cones will be increased due to an increased flux density of the projectiles (see fig. 2.13.). This effect is called focussing. Maxima and minima observed in angular scans, where the direction of the beam or the detector is varied, can be explained in terms of focusing, shadowing and blocking. The width of shadowing/blocking cones in MEIS is of the order of a few degrees. The width in LEIS is of the order of 10º- 20º. For grazing angles of the beam or detector smaller than these typical values, surface atoms can be in each other´s shadowing/blocking cone. This implies that the structure of the outermost layer of a crystalline sample can be determined from LEIS angular scans. This is illustrated in fig. 2.15.

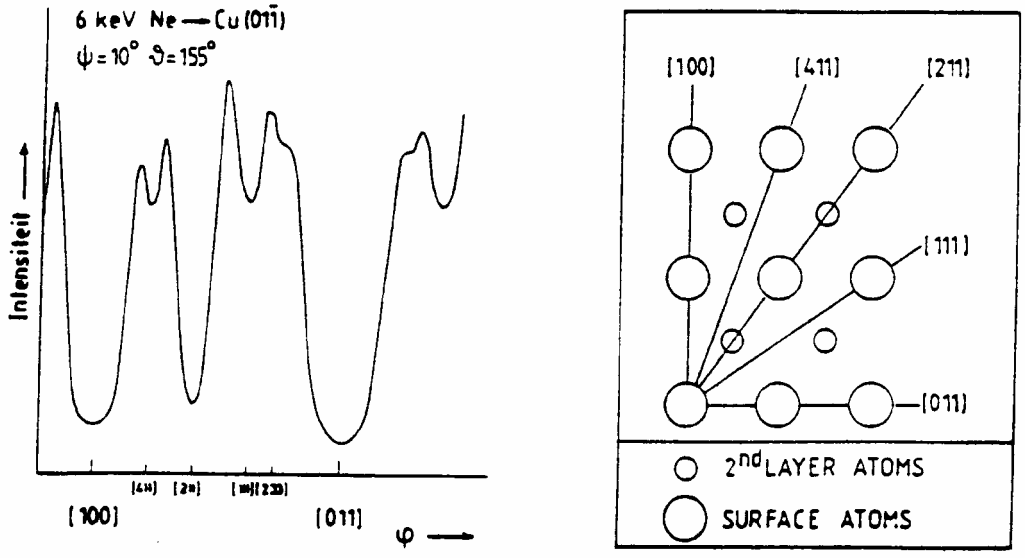

Fig. 2.15. *Azimuthal scan with 6 keV Ne^+ ions on a Cu (110) surface. The Ne^+ beam is incident under an angle ψ=10 º with the surface. Minima in the yield are observed at azimuth angles coinciding with the directions of rows of surface atoms as indicated in the picture at the right.*

Both LEIS (at non-grazing angles) and MEIS angular scans carry information on the positions of atoms in deeper layers.

In MEIS and HEIS, ions moving near the centre of the "channel" between the atom strings will collide with small angles at greater depth than shown in fig. 2.12 with strings of atoms. The ions are gently steered away from the strings, again towards the centre of the channel. This steered motion

gives rise to an enhancement of the flux density near the centre of the channel, which would last until the ion has lost all its kinetic energy, in the absence of lattice imperfections, thermal vibrations or deflections by electrons. This phenomenon is called axial channelling. As a consequence, the scattering or recoiling yield from deeper layers will be reduced by a large factor of the order of 50 if the beam is directed along a major crystal axis. Also the interaction of the ions with core electrons will be reduced, resulting in a reduction of the electronic stopping by up to 50%. An example of a "channelling" spectrum is given in fig. 2.16. The channelling effect is exploited mainly in HEIS to probe the structure of deeper layers.

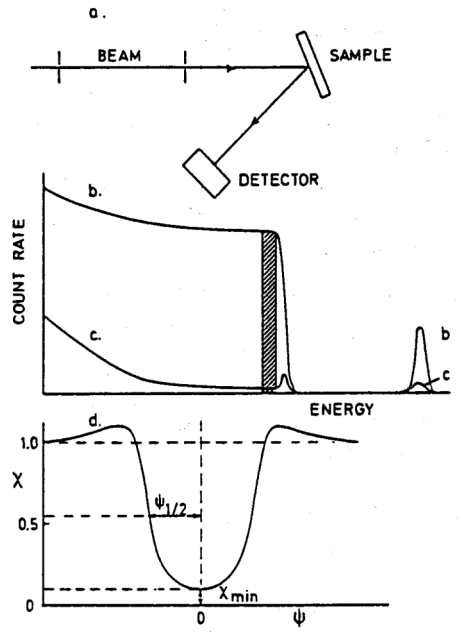

Fig. 2.16. *Schematic presentation of a RBS/channelling experiment. Spectrum b is taken with the beam in a "random" direction; spectrum c with the beam along a crystal axis. In the spectra a peak due to scattering from a heavier atom species, present in a thin layer near the surface, is indicated. The channelling dip d is the sum of channel contents in the indicated window plotted as a function of the angle between the beam and the crystal axis.*

Channelling effects can also be observed when the ion beam is directed between lattice planes. For major crystal planes the yield of scattering or recoiling due to planar channelling is reduced by a factor of the order of 5. Contrary to the situation in axial channelling, the steered motion in planar channelling is more or less coherent (see fig. 2.17.). This gives rise to an oscillation in the scattering yield as a function of depth, as illustrated in the figure.

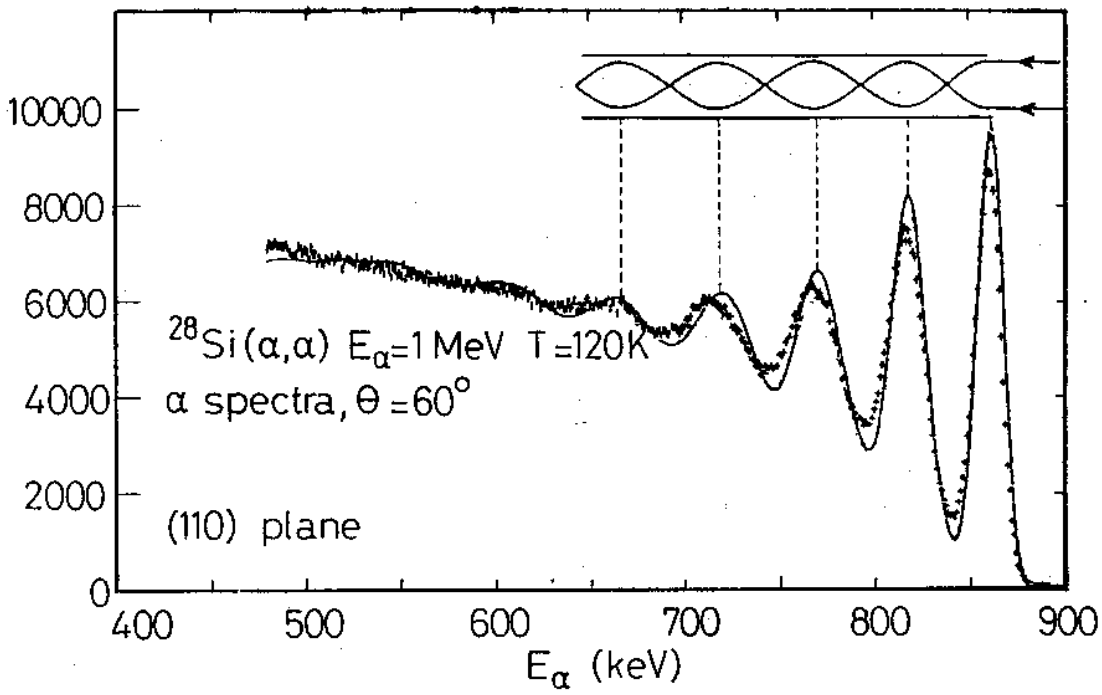

***Fig. 2.17**. Energy spectrum of 1 MeV He+ ions scattered from a Si crystal after planar channelling in a (110) planar channel. The full line is the result of a computer simulation. The ion trajectories oscillating (in phase) are indicated schematically.*

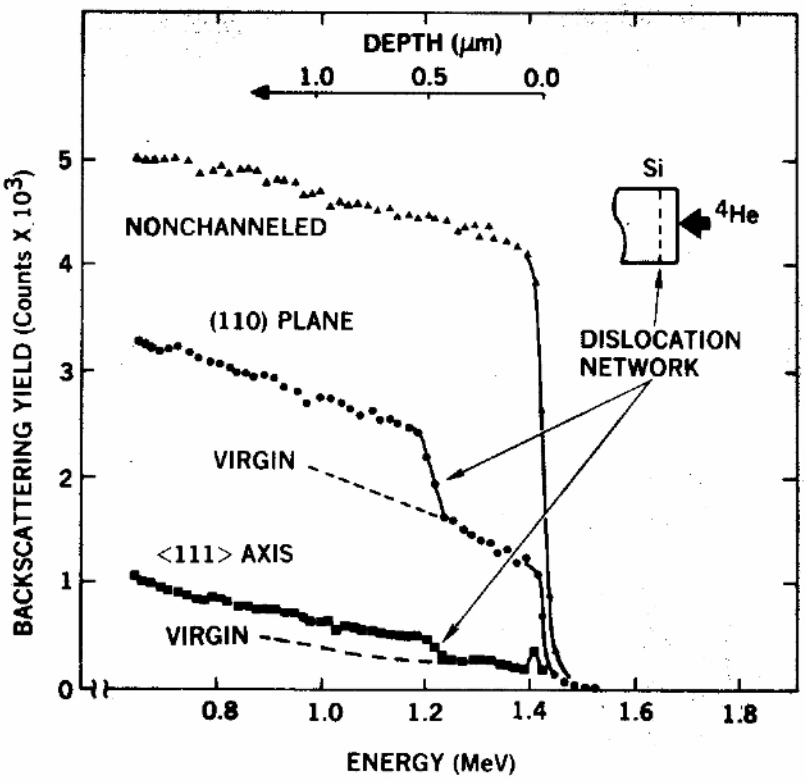

***Fig. 2.18.** An example of phosphorous-diffused Si studied by RBS. Backscattering spectra for 2.5 MeV He ions incident along {110} planar and <111> axial channels are shown. [17].*

Some approximate theories have been developed to predict the width of channelling dips, and the reduction factor of the yield of channelled ions with respect to the scattering yield of ions propagating in a "random" direction in a crystal. These predictions are important for the understanding of the phenomena observed, or for the design of experiments, rather than for a quantitative interpretation of data. The "break-through" angle, for which a channelling ion is not steered back by strings or planes can be estimated (see fig. 2.19.). This angle is a measure for the widths of the axial or planar channelling dips. For the Coulomb potential one gets [18]:

$$\psi_c \cong \left(\frac{a}{d} \sqrt{2Z_1 Z_2 e^2 / E d} \right)^{0.5} \quad (2.24) \text{ (low energy) or } \psi_c \cong \sqrt{2Z_1 Z_2 e^2 / E d} \quad (2.25) \text{ (high energy).}$$

where a is the screening distance and d is the atomic spacing along the aligned row.

In accordance with experimental results the width of channelling dips for axial channelling with MeV protons or He ions are on the order of one, or a few degrees. The widths of planar channelling dips are on the order of a few tenths of a degree.

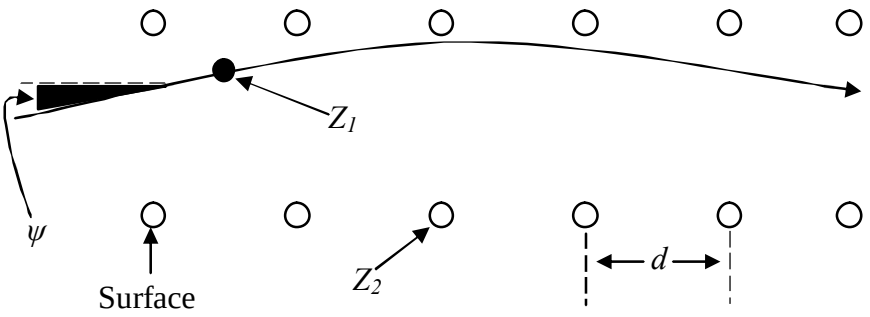

Fig. 2.19. *String model of channelling.*

Using the "continuum" theory of channelling [55], the minimum yield for scattering for axial or planar channelling (as a fraction of the "random" yield) can be estimated:

$$\chi_{\min}(axial) = \pi N d \left(u^2 + a^2 \right) \quad (2.26)$$

$$\chi_{\min}(planar) = \frac{\sqrt{2} M_1}{d_p} \quad (2.27)$$

where N is the atomic density and u is the transverse vibration amplitude and d_p is the distance between planes.

The expressions for the minimum yield give values that are accurate within 30% for axial channelling and within a factor of 2 for planar channelling. For ions in the 100 keV/amu-several MeV/amu range the minimum yield for axial channelling is of the order of one or a few percents; for planar channelling these minimum yields are of the order of 25%.

It is clear that data on channelling carry information on the crystal structure, including crystal defects and thermal vibrations. This information can be obtained per lattice atom species. Data on scattering from - or recoiling of- "foreign" atoms (dopants or impurities) carry information on their atom position in the lattice. The channelling dips of substitutional impurities will be similar to the

channelling dip of the lattice atoms. The yield of interstitial impurities may be much higher that the "random" yield when the beam is directed along specific axis, see fig. (2.20).

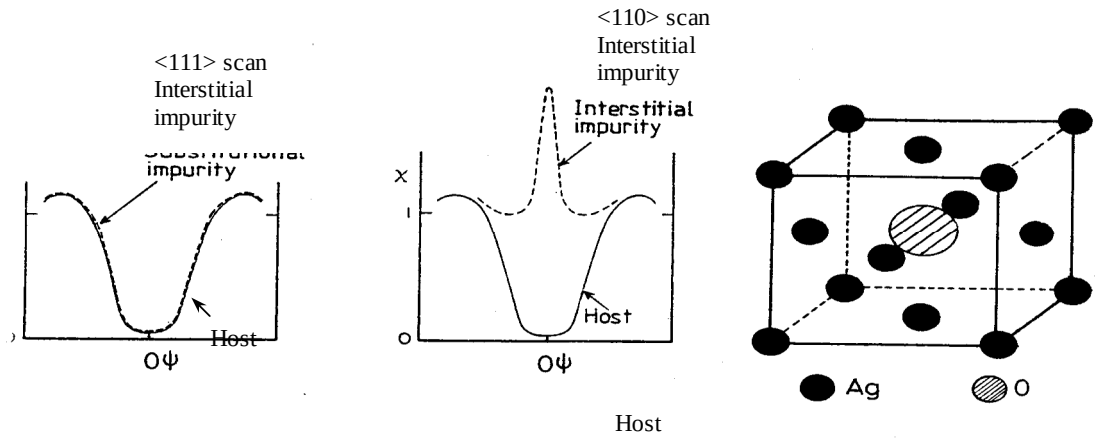

Fig. 2.20. *An interstitial atom in a fcc lattice. Projected in [100] or [111] directions the interstitial atom is in a row of matrix atoms. Projected in the [110] direction the atom is in the middle of a channel. So, for the foreign atoms a dip will be measured around [100] and [111] string directions, and a channelling peak around a [110] direction.*

The potential to extract structure information from ion scattering experiments has not been exploited fully yet. This may be due to the problems encountered in the analysis of the data. For a quantitative analysis, computer simulations of the experiment for trial structures of the atomic arrangement and /or for trial values of the thermal vibrations are needed. As discussed in a next chapter, a number of computer programs has been developed for this purpose. Most programs make use of approximations to keep the computation time within limits. In our group we developed a new and fast simulation program in which these approximations are omitted.

2.5. Calculation of trajectories

In cases that single scattering theory cannot be applied, or when ions are propagating in a mono-crystalline structure, measured data are usually analyzed by comparison with simulated data. In such simulations trajectories of ions propagating in a solid are calculated. In principle a description of an ion trajectory in a solid requires a quantum-mechanical treatment, which cannot be done even with present day supercomputers. To calculate trajectories in a solid, a number of approximations is made:

- The trajectory can be calculated without taking into account the electronic excitations or electron capture and loss processes that take place during the propagation of the ion in a solid. The (impact-parameter dependent) energy loss per collision due to interactions with electrons is taken into account separately.
- A classical description is applied to calculate the trajectory of the ion. This is justified by the fact that the De-Broglie wavelength of ions with velocities as used in IBA is much smaller than the inter-atomic distances in the solid. This wavelength is also small as compared to the interaction length for ion scattering [21].
- A binary collision model is applied, meaning that the ion interacts with only one atom at a time. This is justified by the fact that the distance at which the main interaction between the ion and the atom occurs is smaller than the inter-atomic distance.
- For broad energy regions the ion-solid interaction can be described by a fixed potential which only depends on the ion-atom distance and the properties of the ion and lattice atoms. This

implies that the influence of charge fluctuations of the ion is not taken into account. The range of this potential is assumed to be smaller than the inter-atomic distance.

- The trajectories of ions with energies in the keV-MeV range in a solid can be described to good approximation replacing the actual trajectories by their asymptotes.

On the basis of such a model it is possible to create fast computer programs for the calculation of ion trajectories in a solid, which can be run in a personal computer. The classical binary collision problem can be solved using the laws of conservation of energy and momentum for a given interaction potential.

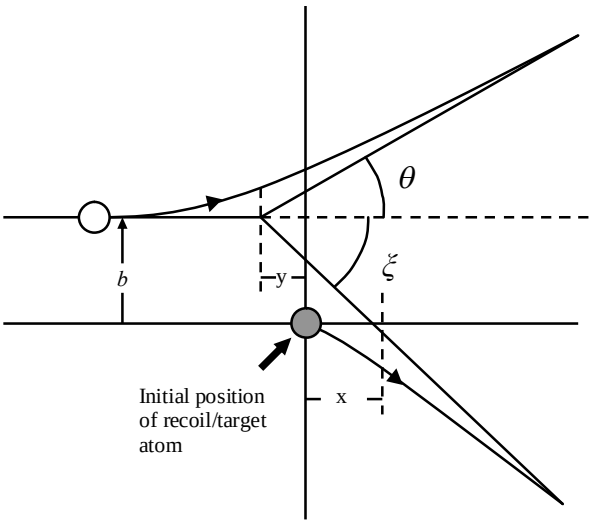

Fig. 2.21. *The classical binary collision in the laboratory system. The asymptotic trajectories of the projectile and the target are shown. The parameters describing the collision of the projectile are indicated.*

The deflection angle θ *in the centre-of-mass* system of an ion approaching an atom with impact parameter b and having an interaction potential $V(r)$ is given by the scattering integral:

$$\varphi = \pi - 2b \int_{r_m}^{\infty} \frac{dr}{r^2 \sqrt{1 - \frac{V(r)}{E} - \frac{b^2}{r^2}}} \quad (2.28)$$

where r_0 is the distance of the closest approach of the projectile.

The distances x and y (see fig. 2.21) are given by:

$$x = \frac{b}{1 + \frac{M_1}{M_2}} \left(\left(1 - \frac{M_1}{M_2} \right) tg \frac{\varphi}{2} - \frac{M_1}{M_2} \tau \right) \quad (2.29)$$

$$y = \frac{M_1 / M_2}{1 + \frac{M_1}{M_2}} b \left(2tg \frac{\theta}{2} + \tau \right) \quad (2.30)$$

where the time integral τ is given by:

$$\tau = 2\frac{\mu}{b}\left(\int_{\rho_0}^{\infty} \frac{dr}{r^2\sqrt{2\mu\left(E_{cm} - \frac{\mu b^2 v^2}{2r^2} - V(r)\right)}} - \int_{b}^{\infty} \frac{dr}{r^2\sqrt{2\mu\left(E_{cm} - \frac{\mu b^2 v^2}{2r^2}\right)}} \right) \quad \text{with } \mu = \frac{M_1 M_2}{M_1 + M_2} \quad (2.31)$$

The physical meaning of this integral is the time difference between particle moving on the real trajectory and the trajectory approximated by asymptotes (see fig. 2.21.).

The momentum (or impulse) approximation for elastic scattering is used for small (of the order of 1º) deflection angles θ. In this approximation it is assumed that the path of the projectile is not deflected to first order and thus the recoil receives an impulse in the direction perpendicular to this path.

We describe the trajectory in the x-z plane and assuming that:

1. The x-component does not change: $dz/dt = v_1$;
2. The force F_x is calculated for a straight trajectory, for x = b, where b is the impact parameter.

In that case we have:

$$\tan\varphi \approx \varphi = \frac{p_x(+\infty)}{p_z(+\infty)} = \frac{1}{mv_1}\int_{-\infty}^{\infty} F_x\,(x,z)\,dt = \frac{1}{mv_1^2}\int_{-\infty}^{\infty} F_x\,(x,z)\,dz \quad (2.32)$$

Here p_x, p_z are the components of the impulse. With $F_x = -\delta/\delta x\, V(x,z)$ and x=b we find:

$$\varphi = -\frac{d}{db}\left[\frac{1}{mv_1^2}\int_{-\infty}^{\infty} V\left(\sqrt{b^2+z^2}\right)dz\right] \quad (2.33)$$

For the Coulomb potential this yields:

$$\varphi = \frac{KZ_1Z_2e^2}{Eb} \quad (2.34)$$

The remaining problem is the choice of the interaction potential. Usually the potential is written as the product of the Coulomb potential between the nuclei of the interacting ion/atom pair times a screening function describing the influence of the electrons:

$$V(r) = \left(\frac{Z_1Z_2e^2}{r}\right)\varphi(r/a) \quad (2.35)$$

where r is the distance of the ion from the nucleus.

The screening function is determined by the relative velocity of the ion, the electron distributions around the atom and the ion and by polarization effects. Depending if the ion velocity is (much) smaller or (much) larger than the Bohr velocity of the electrons, the electron clouds

around the atom and ion will be polarized during the interaction or remain unaltered to first approximation.

For high energies (above a few hundred keV/amu) the ion is stripped from all electrons. In this case the ion can be treated as a bare nucleus and the screening function can be derived to good approximation from the electron distribution of the free atom, using the Poisson relation. The electron density can be calculated from the wave functions that are tabulated for all atoms [56]. This type of calculation can also be done if the ion is not stripped of all its electrons. Then the interaction of the remaining electrons on the ion with the target nucleus and with the target electrons (and vice-versa) has to be taken into account [57]. As a refinement the electron distribution of an atom in the solid may be used (Muffin-tin model). This gives a static potential where the deformation of the electron density of the atom due to the ion-atom interaction is not taken into account.

In the simplest form the electron density due the Thomas-Fermi approximation for the electron density is used to obtain the potential. A good approximation to this potential is due to Molière [58], for which the screening is given by:

$$\varphi(r/a) = \sum_{i=1}^{3} \alpha_i \exp(-\beta_i r / a_{TF}) \quad (2.36)$$

where a_{TF} is the Thomas-Fermi screening radius:

$$a_{TF} = \frac{0.8853 a_H}{\left(Z_1^{\frac{2}{3}} + Z_2^{\frac{2}{3}}\right)^{\frac{1}{2}}} \quad (2.37)$$

with a_H the Bohr radius: 5.292 Å and α_i, β_i constants.

$\alpha_i = \{0{,}1; 0{,}55; 0{,}3\}$ $\beta_i = \{6{,}0; 1{,}2; 0{,}3\}$

Another approximation to the screening function is given by Ziegler et al. [22], giving rise to the so-called ZBL or Universal potential, in which the screening function is given by:

$\Phi(r/a) = \sum_{i=1}^{4} p_i \exp(-q_i r / a_U)$, a_U - screening radius. (2.38)

$$a_U = \frac{0.8853 a_H}{\left(Z_1^{0.23} + Z_2^{0.23}\right)} \quad (2.42)$$

where p_i and q_i – are constants.

$p_i = \{0.18175, 0.50986, 0.28022, 0.02817\}$

$q_i = \{3.1998, 0.94229, 0.4029, 0.20162\}$

In this case the parameters were obtained by fitting to experimental data.

As argued below, the use of static potentials is not justified at low energies where the ion velocity is smaller than the Bohr velocity. This is the case for ion energies in the range smaller than 10 keV/amu. At these energies the ion is also not fully stripped of all its electrons. However, in many works the Molière or ZBL potential is also used in this energy range with remarkable success. In these cases the potentials are slightly modified by replacing the screening radius, as given by eq. 2.35, by a lower value obtained by fitting to experimental data.

A better alternative is to use at these low energies a dynamic potential. In such a potential the deformation (polarization) of the electron density around the ion and the target atom during the ion-atom interaction is taken into account. The use of a dynamic potential is required because the time scales of the collision and the deformation of the electron clouds are comparable. In this case the potential can be calculated on the basis of a dynamic two body problem according to the Hartree-Fock-Slater model. The interaction of one electron with all the other electrons is replaced by an average charge distribution due to all the electrons. For this potential the Schrödinger equation for the ion-atom pair is solved, and the averaged interaction potential is recalculated. In an iterative process finally a stable solution of the Schrödinger equation is obtained. From the resulting electron density distribution the potential can be calculated. This process is repeated for the range of distances for which the potential needs to be known. Slater and Fock introduced anti-symmetric wave function which has the physical meaning of a correction for the fact that the electron has only interaction with remaining electrons instead with all of them. In more sophisticated versions of the HFS model also solid state effects can be taken into account [59,60].

Of course an intermediate range of ion energies exists in which the polarization of the electron distributions is only taking place partially. For the calculation of a potential for these cases time dependent HFS calculations should be done. To our knowledge such complicated calculations have not been tried yet.

In some cases it may be questionable if the potential can be considered to be constant during the calculation of trajectories. Due to fluctuations in the charge of the ion, the interaction potential between the ion and the atoms may vary as well. As far as we know, this problem has not yet been tackled in trajectory calculations.

2.6. Radiation damage

Radiation damage is a point of concern in ion beam analysis. The formation of damage may be split into nuclear damage and electronic damage. In nuclear damage formation atoms in the sample are displaced due to nuclear collisions. In this way pairs of interstitial atoms and vacancies (Frenkel pairs) are formed. Some of these pairs may annihilate, especially when the displacement of the interstitial atom is small. The number of Frenkel pairs formed along the ion track depends on the energy E_{nucl} lost in nuclear stopping and the displacement energy E_d of an atom in the lattice. An energetic ion creates many interstitial atoms. These interstitial atoms may form other interstitial atoms, so that a collision cascade is formed (see fig. 2.1). According to Kinchin and Pease [61] the number of pairs that do not immediately annihilate immediately can be estimated as:

$N_f = 0.8\ E_{nucl} / 2E_d$ (2.43)

The further development of the damage strongly depends on the type of material and the temperature. If the interstitial atoms are mobile at the prevailing temperature they may form interstitial clusters or dislocation loops (by the local creation of an extra layer in the lattice). If vacancies are mobile, they may form voids or loops. Both clusters or loops and voids cause locally a strain field in the lattice. In metals and in semiconductors interstitial atoms are mobile at room temperature. In metals also vacancies are mobile at room temperature. In semiconductors and other non-metallic materials amorphous clusters may form, depending on the temperature and the density of interstitial atoms formed in the collision cascade. Nuclear damage will always interfere with the measurement of structure in thin layers. For room temperature this is especially the case for non-metals. However, when light ions (H, He) are used, the damage can be limited to acceptable (hardly observable) levels if proper precautions are taken. These include the use of large position-sensitive detectors, use of a geometry, where the cross sections for scattering or recoiling are large, and a change of target spot during the measurements. This last option requires large and homogeneous samples.

The electronic damage is proportional to the electronic stopping and is the result of electronic excitations of the atoms in the sample. These excitations may give rise to the breaking of bonds, especially in organic materials. This effect occurs at any level of electronic stopping, and gives rise to the loss of hydrogen from organic samples during irradiation. The loss (not the modification of the structure) may be prevented by cooling the sample to liquid He temperature. Via electron-phonon interactions the sample material is heated along the ion track. In insulating materials this may give rise to local melting and re-solidification, if the electronic stopping exceeds certain threshold values. The diameter of the melted columns along ion tracks may be of the order of 10 nm [62].

This implies that with a fluence of 10^{11} ions/cm^2 practically all the irradiated material is affected. Roughly speaking, such fluence is needed for the accumulation of one energy spectrum in HEIS carried out with heavy ions. The mentioned threshold is about 5-10 keV/nm, depending on the sample material. These threshold values are exceeded for heavy ions with energies of a few tens of MeV, as commonly used in ERD. For these ions also the number of Frenkel pairs created per unit length is large. The conclusion is that ERD with energetic heavy ions cannot be combined with structure measurements in semiconductors or in insulating materials. It is noteworthy to mention that the nuclear damage created by the irradiation with energetic heavy ions may be repaired or prevented by the heating/melting due to electronic interactions. In such cases it is questionable if the measured structure is the same as in the non-irradiated material [63].

For HEIS or MEIS executed with light ions the electronic damage is not a point of concern, with the exception of bond-breaking effects as observed in the investigation of organic materials.

2.7. Detectors

The oldest type of detector is a photographic plate. They were used by Curie and Rutherford to detect nuclear decay particles. Photographic plates have no energy resolution. However, they have excellent position resolution. For this reason they have been used also as focal plane detectors in magnetic spectrographs [64].

Nowadays, for the detection of high-energy ions often a Si detector is used. In principle this is a Si diode with the voltage in the reverse (non-conducting) direction. The p-n transition is near to the surface, which is commonly covered with a thin Au layer. When a high-energy ion penetrates into the detector, most of its energy is dissipated by creating electron-hole pairs in the depletion layer of the diode, causing a transient current. The signal is to good approximation proportional with the energy of the ion. The efficiency of this type of detector is unity. For the energy range of interest (RBS, ERD) the energy resolution is approximately 12 keV for He ions and ~ 5 keV for protons. The energy resolution decreases strongly with increasing mass of the detected ion [17,18]. For instance, the resolution at 10 MeV is for C: 70 keV, for O: 100 keV, and for Si 260 keV. In the scattering plane the detector opening cannot exceed 1^o to avoid excessive kinematic spread. In the direction perpendicular to the reaction plane the opening angle can be a few degrees. Obviously the detector size could be increased by using a position-sensitive detector. Such developments are emerging in recent literature [65].

Because Si detectors cannot discriminate between masses of ions, they can only be used in ERD if the mass of the ion is determined independently. This can be done by bombarding the sample with heavy ions. The lighter recoiled ions are penetrating through a foil placed in front of the detector, while the heavier scattered (beam) ions are stopped in this foil. This method has limited applications. In another version the foil is replaced by a very thin silicon detector. The mass of the ion penetrating the thin detector can be derived from the specific energy loss in this thin detector. This is a useful system for discriminating between light recoiled atoms (H, Li, C, N, O, F).

Gas-filled detectors (see [66] for the description of a suitable detector) are commonly used for ERD measurements [67] carried out with energetic beams of heavy ions with energies roughly

between 50 and 200 MeV. The recoils are detected in an angular range where no direct scattering occurs. The depth range that can be probed in this way is on the order of 200nm. Recoiling ions with energies of a few MeV/amu are entering through a thin foil (~ 1 μm mylar mounted on a grid) into a ~200 mm long chamber filled with up to a few tens of mbar of a gas (methane, butane). The electrons and the ions, created along the trajectory of the impinging ion, are detected as a function of the lateral position (resolution 1mm x few mm's), by measuring the drift time of the electrons generated along the trajectory and accelerated towards grids placed parallel to the trajectories. The number of electrons is also measured as a function of the longitudinal position, by splitting the grids in a number of sections. In this way the angle, ion mass and the total energy can be determined per event, so that a correction for kinematic energy spread can be carried out. A new type of ionisation detector chamber has been tested successfully, using a Si3N4 etched window [68], with initial thickness 100 nm which corresponds to 32 $\mu g/cm^2$, and recently with a window of 50 nm. Due to the extremely thin entrance window, the resolution is two times better than of a boron implanted silicon detector for 2.5MeV iodine ions.

For low-energy ions often a channel-plate detector or some other type of electron multiplier is used. Ions or neutral atoms impinging on the detector induce emission of one or more electrons. These electrons are accelerated by an electric field in narrow channels in which many collisions with the channel wall take place. During each collision more secondary electrons are created. The electrons are collected on an anode, where they create a charge pulse. The height of this pulse can be equivalent to 10^5-10^6 electrons. This height has no relation with the energy of the impinging ion. The pulse can be used as the stop pulse in a time-of-flight measurement. The start pulse may then be derived from the beam chopper and the time delay between both pulses can be measured with a TAC (time-to-amplitude converter) [69].

This type of detector is also used in RBS or ERD measurements combined with Time-of Flight (ToF) [69].

In this type of measurement ions to be detected pass through a thin foil. The secondary electrons, set free in this foil, are detected usually with a channel-plate detector. In coincidence with this signal, the arrival time of the ions at a second foil or a silicon detector placed at a distance of roughly 1 m from the first foil is detected. The flight time can be determined with a precision of better than 0.5 ns. A stop detector (mostly a silicon detector) can be placed behind this foil to measure the total energy of the ion. Mass identification is obtained from the measured velocity combined with the energy. The energy resolution derived from the time-of-flight measurement can be on the order of $\Delta E/E = 1\%$. A drawback of this type of measurement is the very small solid angle. This solid angle could be enlarged when a position-sensitive detector were used to monitor the secondary electrons from the first foil. To obtain a large solid angle in this way, the size of the second detector should be increased correspondingly. To our knowledge, such systems are not yet developed.

In some laboratories electrostatic or magnetic spectrographs are used for the detection of ions [71]. The achievable energy resolution of $\Delta E/E \sim 5 \times 10^{-4}$ is much better than obtained with the methods described above. With such devices near-to-mono-layer depth resolution can be obtained under favourable conditions [72,73].

In a spectrographs ions are deflected over a large angle (~90^o) and the ions are detected in the focal plane with a 1- or 2- dimensional position sensitive detector with a large size to obtain an energy spectrum over a range of ~5-20% of the energy of the incoming ions, and in some cases, to resolve the angle perpendicular to the scattering plane ($\Delta \phi \sim 5^o$-20^o). The opening angle in the scattering plane must be small (< 0.2^o) to avoid kinematic spread. For medium energy ion scattering (MEIS) mostly electrostatic spectrographs are used, with a 2-dimensional position sensitive channelplate detector in the focal plane. With such a device an angular range of up to 20^o can be measured. For ERD mostly magnetic spectrographs are used. For the identification of the ion

species in ERD an additional device is needed, such as a Wien filter or a mass-sensitive gas-filled detector in the focal plane. The focusing properties of some spectrographs can be chosen such that automatically a correction for the kinematic spread is obtained. In such spectrographs a large solid angle of up to 20 msr can be obtained by using a large 2-dimensional position sensitive detector in the focal plane [57]. The angle in the scattering plane is not resolved. The most elaborate spectrographs in use nowadays for materials research are inherited from previous nuclear physics groups [74,73,75]. The very good resolution is better than can be used in depth profiling of thin layers with a thickness of more than a few nm with ERD, because already beyond a thickness of a few nm energy straggling becomes the dominant factor in the determination of the depth resolution. A major drawback of this type of detector is that only ions with one specific mass/charge ratio can pass the spectrograph for one setting of the fields. The amount of useful counts is thereby reduced by roughly a factor of 3, if ions with the most frequently occurring charge are observed. This loss in counts is not a main obstacle. However, the calibration, relating the number of counts with the relative amount of atoms of a certain species in the sample, is lost. At present the division over the charge fractions of ions emerging from a sample cannot be accurately predicted.

2.8. Optimization of measurements of the composition and structure of thin layers

In this section we try to define the optimum conditions for the measurement with IBA of the composition and structure of layers with a thickness of up to a few tens of nm. Even for this restricted goal it is not possible to select one technique. The choice depends on the sample composition (detection of light elements in a heavier matrix, or vice-versa) and on the distance from the surface of the layer(s) for which the information is needed.

For the surface layer and the first one or two layers below the surface, LEIS-ToF carried out with Ar or Ne ions in glancing angle geometry would be the best technique [60]. In one single LEIS measurement it is possible to distinguish scattered and recoiled particles. For an optimum set-up with a flight path of about 1 m and a time resolution of better than 20 ns, both for scattering and recoiling the mass resolution is about 2 amu, with the exception of masses > 70 amu. Thanks to the very large cross sections for scattering and recoiling, angular distributions can be measured at forward scattering angles in a short time (< 30 min) with an ion fluence of < 10^{12} ions/cm^2, implying that the damage due to the irradiation is very small. If only the composition of the outer layer has to be measured, LEIS with Ar ions using an electrostatic detector to measure the scattered ion fraction is the method of choice.

For a layer thickness of up to 10 mono-layers MEIS is a very suitable technique, especially to probe heavier elements in a lighter matrix. Since only scattered ions are observed, there is a problem with background in the measurement of lighter elements in a heavier matrix. The mass resolution is not as good as with LEIS. Hydrogen cannot be detected. The depth resolution near the surface amounts to a few mono-layers. The method is very well suited to resolve the atom positions of heavier elements in a lighter matrix or to determine the structure of epitaxial layers [61, 62].

For thicker layers ions with higher energies are needed to perform RBS measurements for heavy elements in light matrices, or ERD for light atoms in heavy matrices. Especially for the measurement of structures the use of energetic heavy ions has to be avoided, as was argued in section 2.6. Unless very large depths of more than a few hundred nm have to be probed, beams of He ions are a better choice as compared to protons, because of a higher cross section for scattering and higher stopping powers. For 1 MeV He ions in Si the energy straggling would be 10 keV for a probing depth of 138 nm, if the directions of the beam and detector are nearly perpendicular to the sample. This implies that for smaller depths if would be of advantage to use a detector with a better energy resolution than a Si surface barrier detector. For ERD measurements with He ions, aiming at structure determinations, a detector would be required that discriminates the large flux of He ion scattered to forward directions, and that can identify the ion species. To reduce the effects of

radiation damage, such a detector should be a position sensitive detector with a wide detection angle. In addition such a detector should have a very good energy resolution. The development of such a detector is a subject of this thesis.

Even with the "ideal" detector some other considerations come into play. To have the best depth resolution, glancing-angle geometry should be used, as described earlier. Also the beam energy or the energy of the recoiled atoms should be chosen in the neighbourhood of the maximum in the stopping power (see fig. 2.6). For instance, for (recoiling) C ions this maximum would be approximately 2 MeV. Another item tied with the reduction of radiation damage, is the efficiency of the measurement. For a given detector the efficiency is determined by the cross section for ion scattering or recoiling. For the Coulomb potential this cross section varies as $1/E^2$. The nuclear stopping and, therefore the creation of damage per unit path length, varies as ln(E)/E. The cross section for scattering and recoiling varies with the scattering (recoiling) angle as indicated in fig. 2.21. As can be seen, it is advantageous to choose a forward angle for RBS. At forward angles the mass discrimination in RBS is very limited, so that such a choice is only possible in special cases. For ERD a recoil angle not far from 90º would give a very high cross section. Here the problem is that near 90º the recoil energy is close to zero and that the kinematic spread at a recoil angle near 90º is very large. This spread is given by $\Delta E/E = 2tg(\xi)\Delta\xi$. To determine the optimum conditions for an experiment, a computer simulation in which all parameters are varied will be necessary.

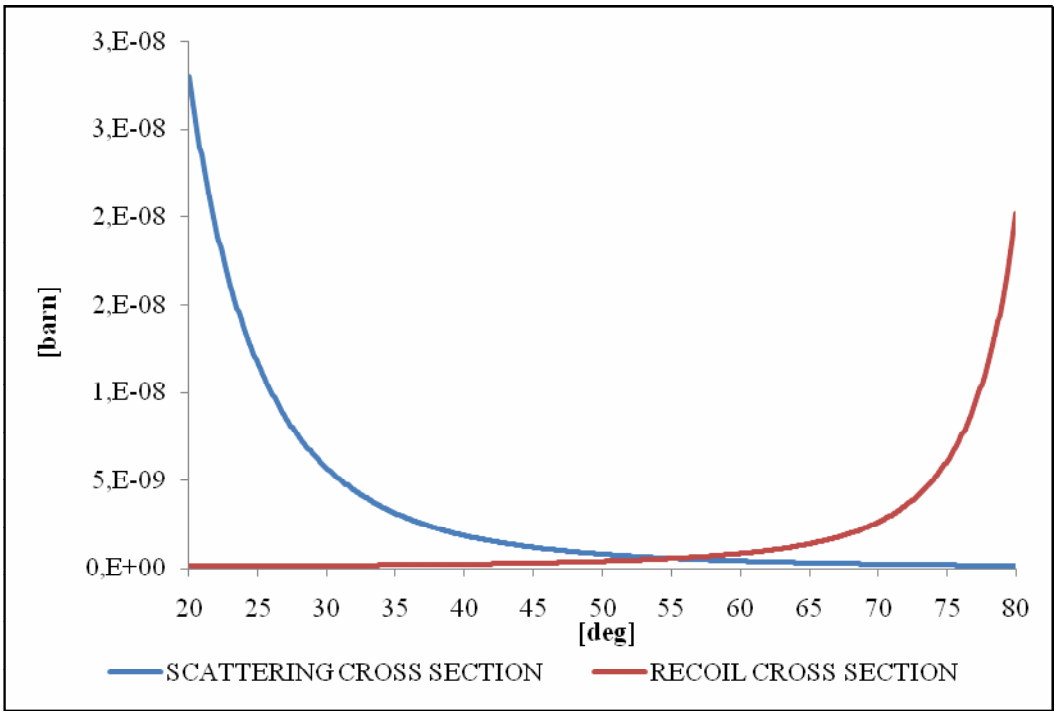

Fig. 2.22. *The cross section for recoiling and scattering for 2MeV He on Si as a function of the recoil/scattering angle.*

2.9. References

17. J. R. Tesmer, M. Nastasi, Handbook of Modern Ion Beam Material Analysis (Materials Research Society, 1995).

18. J. R. Bird, J. S. Williams, Ion Beams for Materials Analysis (Academic Press Australia, 1989).
19. M. Nastasi, J. W. Mayer, J. K. Hirvonen,, Ion-Solid Interaction (Cambridge University Press, 1996).
20. D. O. Boerma, Nucl. Instr. and Meth. B 50 (1990) 77.
21. J. Lindhard et al.: Notes on Atomic Collisions I-III (Kgl.Dan.Vid.Selsk.Mat.Fys.Medd. 36,10(1968), 33,14(1963), 33,10(1963)).
22. J. F. Ziegler, J. P. Biersack, and U. Littmark, In The Stopping and Range of Ions in Matter, volume 1, New York, 1985. Pergamon.
23. O.B. Firsov, Zh. Eksp. Teor. Fiz. 36 (1959) 1517.
24. T.L. Ferrel, R.H. Ritchie, Phys. Rev. B 16 (1977) 115.
25. P.M. Echenique, R.M. Nieminem, J.C. Ashley, R.H.Ritchie, Phys. Rev. A 33 (1986) 897.
26. W. Brandt, M. Kitagawa, Phys. Rev. B 25 (1982) 5631.
27. P.J.M. Smulders, D.O. Boerma, Nucl. Instr. And Meth. B 29 (1987) 471.
28. C. Deutsch, G. Maynard, Phys. Rev. A 40 (1989) 3209.
29. O.H. Crawford, Phys. Rev. A 39 (1989) 4432.
30. T. Kaneko, Phys. Rev. A 41 (1990) 4889.
31. A. Bret, Nucl. Instr. and Meth. B 88 (1994) 107.
32. T. Kaneko, Phys. Rev. A 49 (1994) 2681.
33. E.J. McGuire, Phys. Rev. B 57 (1998) 2758.
34. P.L. Grande, G. Schiwietz, Phys. Rev. A 58 (1998) 3796.
35. G. Schiwietz, P.L. Grande, Nucl. Instr. And Meth. B 153 (1999) 1. 1999.
36. N. Bohr and J. Lindhard, K. Dan. Vidensk. Selsk. Mat. Fys.Medd. 28 (1954) 7.
37. H.D. Betz and L. Grodzins, Phys. Rev. Lett. 25 (1970) 903.
38. P. Sigmund, Stopping of Heavy Ions, a Theoretical Approach, Springer Tracts in Modern Physics Vol. 204, Springer (2004).
39. J. Lindhard, M. Scharff, and H. E. Shiøtt, Mat. Fys. Medd.Dan. Vid. Selsk. 33, 1 (1963).
40. D. I. Thwaites, Radiation Research, 95 (1983) 495.
41. J. F. Ziegler and J. M. Manoyan: Nucl. Inst. And Meth. B 35 (1988) 215.
42. P.L. Grande, G. Schiwietz, Program CasP, http://www.hmi.de/people/schiwietz/casp.html.
43. E. Rauhala, J. Appl. Phys. 56 (1984) 3324.
44. L.R. Doolittle, Nucl. Instr. and Meth. B 9 (1985) 344.
45. E. Kótai, Nucl. Instr. and Meth. B 85 (1994) 588.
46. E. Szilágyi, F. Pászti and G. Amsel, Nucl. Instr. and Meth. B 100 (1995) 103.
47. N.P. Barradas, C. Jeynes and R.P. Webb, Appl. Phys. Lett. 71 (1997) 291.
48. M. Mayer, Technical Report IPP9/113, Max-Planck-Institut für Plasmaphysik, Garching, Germany, 1997.
49. T. Sajavaara, K. Arstila, A. Laakso and J. Keinonen, Nucl. Instr. and Meth. B 161–163 (2000) 235.
50. S. Shimoda, T. Kobayashi, Nucl. Instr. and Meth. B 219 (2004) 573.
51. J.F. van der Veen, Surf. Sci. Reports, 5 (1985) 199.
52. H. Niehus, W. Heiland and E. Taglauer, Sci. Reports, 17 (1993) 213.
53. D. O. Boerma: Nucl. Instr. and Meth. B 183 (2001) 73.
54. J. F. van der Veen, Surface Sci. Reports, 5 (1985) 199.
55. J. Lindhard, K. Danske Vidensk. Selsk. Mat. Fys. Medd. 34 (1965) 14.
56. C. F. Bunge, J. A. Barrientos, Atomic Data and Nuclear Tables 53 (1993) 113.
57. V.A. Khodyrev, private communication.
58. G. Molière Z. Naturforsch. 2A (1947) 133.
59. J. C. Slater, Phys. Rev. 81 (1951) 385.
60. H. Adachi, T. Mukoyama, J. Kawai, Hartree-Fock-Slater Method for Materials Science, Vol. 84, Berlin, 2006 Springer.
61. G. Kinchin and R. Pease, Rep. Progr. Phys. 18 (1955) 1.

62. M. Toulemonde, S. Bouffard, F. Struder, Nucl. Instr. and Meth. B 91 (1994) 108.
63. G. Dollinger, A. Bergmaier, L. Goergens, P. Neumaier, W. Vandervorst and S. Jakschik, Nucl. Instr. and Meth. B 219 (2004) 333.
64. J. Freudenthal, F. W. Jacobs, International Journal or Mass Spectrometry and Ion Physics, 46 (1983) 115.
65. Kai Arstila, J. Forster, K. Mizohata, Erik Edelmann, Pertti Tikkanen, Timo Sajavaara and Juhani Keinonen, "Large solid angle position sensitive detector for elastic recoil detection analysis", http://www.physics.helsinki.f
66. R. G. Elliman, H. Timmers and T. D. M. Weijers, Nucl. Instr. and Meth. B 219 (2004) 410.
67. W. M. Arnoldbik, N. Tomozeiu and F. H. P. M. Habraken, Vacuum 73 (2004) 109.
68. M. Stocker, R. Bertschniger, Nucl. Instr. and Meth. B 223 (2004) 104.
69. M. Draxler, S.N. Markin, S.N. Ermolov, K. Schmida, C. Hesch, A. Poschacher, R. Gruber, M. Bergsmann, P. Bauer, Vacuum 73 (2004) 39.
70. S. Giangrandi, B. Brijs, T. Sajavaara, K. Arstila, A. Vantomme and W. Vandervorst, Nucl. Instr. and Meth. B 261 (2007) 529.
71. D.O. Boerma, Nucl. Instr. and Meth. B 136 (1998) 42.
72. R. G. Smeenk, R. M. Tromp, H. H. Kersten, A. J. H. Boerboom and F. W. Saris, Nucl. Instr. and Meth. 195 (1982) 581.
73. O. Schmelmer, G. Dollinger, G. Datzmann, C. Goeden and H. -J. Körner, Nucl. Instr. and Meth. B 158 (1999) 107.
74. H.A. Enge, Nucl. Instr. and Methods 28 (1964) 126.
75. A. A. Rollefson, J. D. Zumbro, J. W. Kaiser, R. W. Tarara and C. P. Browne, Nucl. Instr. and Meth. 204 (1982) 85.
76. S.Y. Grachev, J.M. Gallego, D. Écija, D. O. Boerma, R. Gozalez-Arrabal, R. Miranda, Nucl. Instr. and Meth. B 219-220 (2004) 593
77. D. J. O'Connor, E. R. Wouters, A. W. Denier van der Gon, J. Vrijmoeth, P. M. Zagwijn, W. F. J. Slijkerman, J. W. M. Frenken and J. F. van der Veen, Surface Science, 287 (1993) 438.
78. T.J. Wood, C. Bonet, T.C.Q. Noakes, P. Bailey, S.P. Tear, Surf. Science 598 (2005) 120.

Charter 3. THE MAGNETIC SPECTROGRAPH

3.1. Introduction

As was discussed in the previous chapter, an ideal detector for both RBS and ERD measurements should be mass dispersive, and have an energy resolution that is good enough to obtain nm resolution near the surface. In addition, it should have a large solid acceptance angle, with the angle resolved in two dimensions within this solid angle. The resolution of the determination of this angle should be on the order of 0.1º x 0.1º to make possible corrections for the kinematic spread, and to be able to resolve blocking patterns for structure determination. Such an ideal detector does not exist yet for the ion beam analysis technique. As will be shown in this chapter, such a detector can be designed using modern techniques. Basically it consists of a wide-angle magnetic spectrograph provided with a facility that enables the determination of the position with which an ion enters into the magnet. For this purpose, ions entering into the spectrograph first pass though an ultra-thin carbon foil. The electrons generated in this foil are focused onto a 2-dimensional position sensitive detector so that the position at which the ion passed the foil can be reconstructed from the output of the detector. Already a long time ago the use of an entrance foil with this purpose has been proposed in the literature [1,2,3,4,5,6,15,8,16]. Until now, two large spectrographs were designed for mass separation of radioactive isotopes produced for nuclear physics studies. These facilities with a foil to determine the entrance angle are not yet working. No such spectrographs were designed for applications in material science.

3.2. General concept

A magnetic spectrograph is a sector magnet with a vacuum chamber between its poles. Ions passing through the (vertical, homogeneous) magnetic field $\boldsymbol{B}$ experience the Lorentz force $\boldsymbol{F}=q\boldsymbol{v}\times\boldsymbol{B}$ and follow a circular path with radius $\rho = mv/Bq$ in the horizontal plane. If the bending angle is approximately equal to the sector angle of the magnet the ions will be transmitted. For a given value of $B\rho$, ions with magnetic rigidity mv/q are selected. Such sector magnets are used as analyzing magnets behind an ion source or an accelerator, in mass spectrometers or in magnetic spectrographs. In the latter two applications often electrostatic elements are added to select the ion mass m, charge q and velocity v separately. As illustrated in fig. 3.1a and 3.1b, a sector magnet focuses a beam of ions in the (horizontal) bending plane, because of differences in path lengths in the magnetic field. These focusing properties can be tuned by changing the angle of the pole face with respect to the beam direction. Focusing in the perpendicular (vertical) direction requires a component of the magnet field in the horizontal plane perpendicular to the ion trajectory. As

illustrated in fig. 3.1c, a horizontal component is present in the fringing fields at the pole faces. This horizontal field has a component perpendicular to the ion trajectories if the beam makes an angle ≠ 90º with the pole face. It changes its sign going from the upper pole to the lower pole and

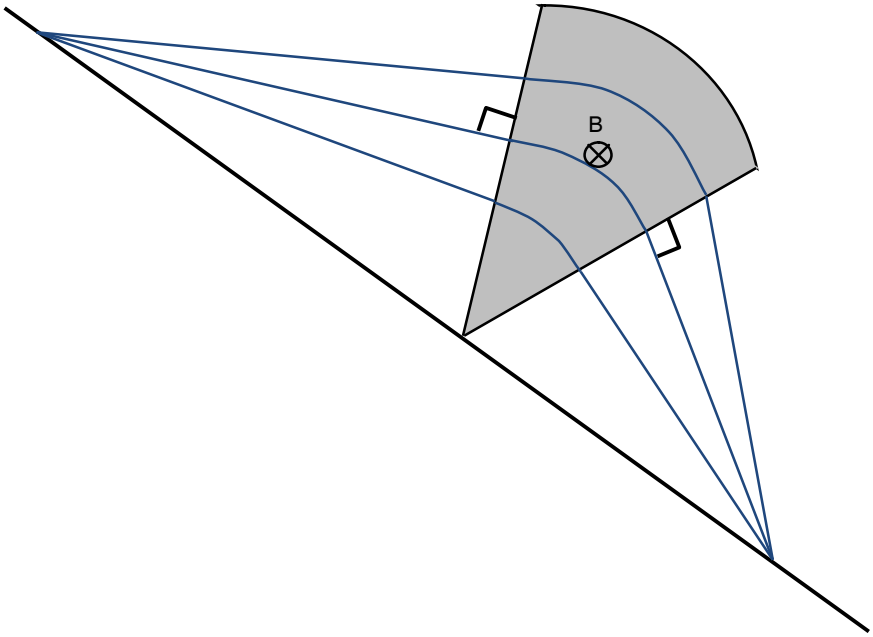

MAKE THE FIGURE SYMMETRIC

Fig. 3.1a. *The effect of different pole face angles in generating different ion path lengths (blue) which cause focusing of the ion beam in the horizontal plane.*

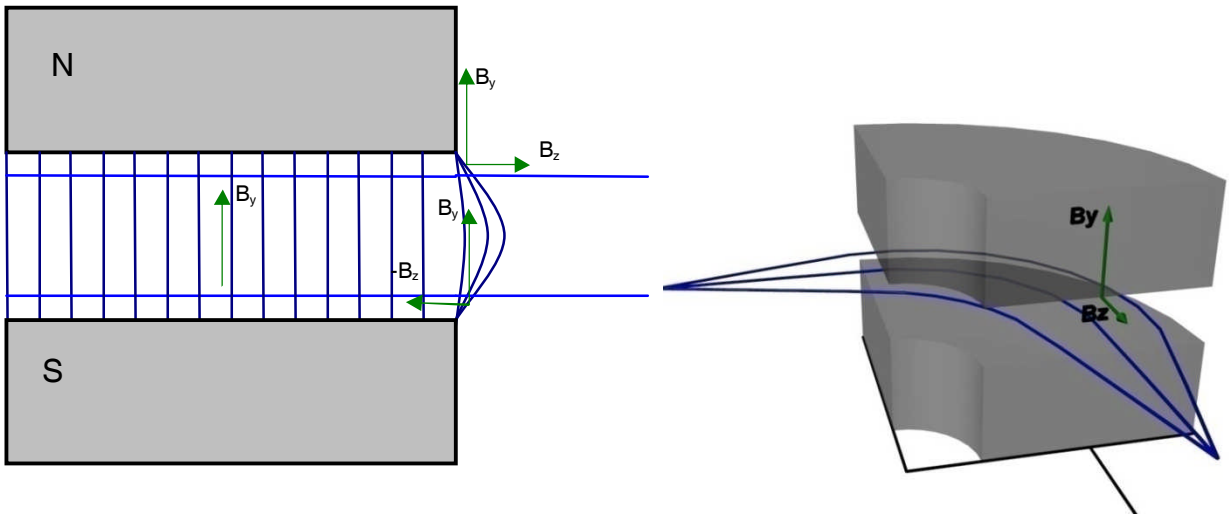

Fig. 3.1b. *Example of a magnet, with horizontal focusing properties only. The magnetic field lines between the poles are indicated.*

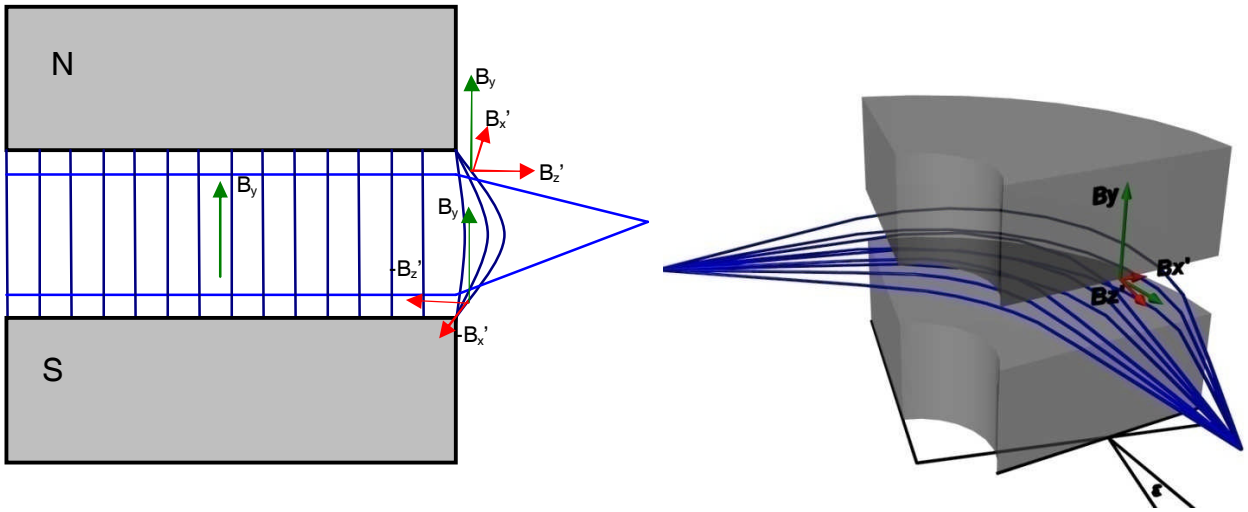

Fig. 3.1c. *Example of a magnet with a tilted pole-face, wit hthe magnetic field lines between poles indicated. The effect of the fringing field gradient is focusing the beam in the vertical plane.*

it converges the beam for ε > 0 (see fig. 3.1c). A horizontal magnetic field component perpendicular to the ion trajectories can also be generated by a field gradient in the magnet, induced by non-parallel pole pieces (see fig. 3.2). Fine tuning of the focusing properties in horizontal and vertical directions can be obtained by curvatures in the entrance and exit pole faces and by applying a calculated curved shape to the non-parallel planes of the pole shoes. By applying curved shapes of the entrance and exit pole faces, a plane (versus curved) focal plane can be obtained that is perpendicular to the beam. The focal plane comprises the focal points for the different energies. These points form a horizontal line for trajectories in the central horizontal plane. For other trajectories the focal point may be above or below the central focal line.

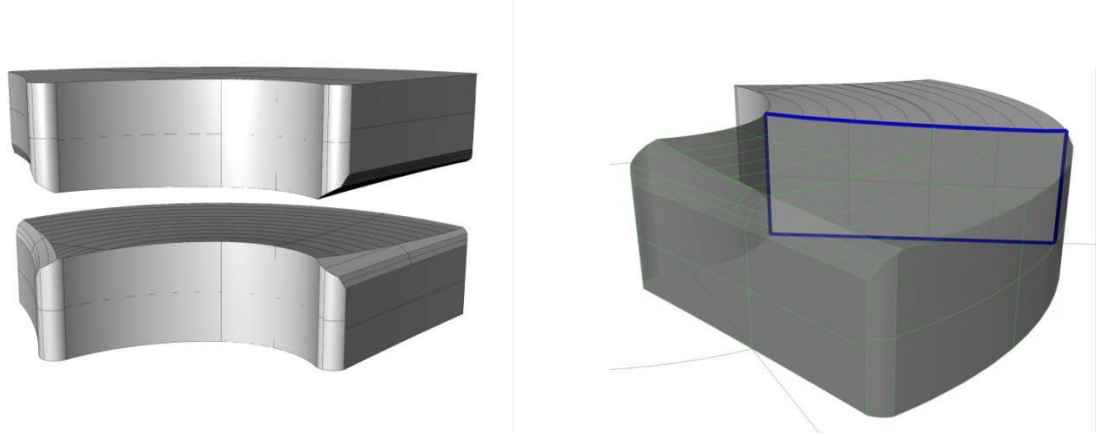

Fig. 3.2. *View of the non-parallel position and curved shape of the poles in the spectrograph magnet. The cross section indicated in blue in the right-hand figure shows the curvature of one of the pole pieces.*

As explained in the introduction the spectrograph should have a large acceptance angle. The "beam" of ions to be detected emerges from a small (~ 1 x 1 mm^2) spot on the sample. It would be possible to focus this diverging beam into the magnet using a large quadrupole lens, as in a number of large spectrograph systems developed for nuclear physics. The use of such a quadrupole would make the system extra large and expensive. In the present design it is tried to avoid the use of such a

lens. This implies that the object distance of the spectrograph should be short to limit the space needed for the beam between the pole shoes. The divergent beam entering into the magnet should be focused at the entrance pole faces to a parallel beam in the vertical direction as in fig. 3.1c.
For each energy, an image of the beam spot on the sample should be formed with a magnification < 1 in the horizontal direction. This image may be elongated in the vertical direction. The energy dispersion in the focal plane should be of the order of $\Delta E/E \sim 10\%$ over a length of 100 mm. It is possible to obtain relatively simple position sensitive detectors with a size of 100 mm. In addition the range of magnetic rigidities of the ions to be detected should be compatible with the use of the spectrograph for RBS and ERD. This implies that the maximum value of the product $B\rho$ should be of the order of 0.4 Tm. Taking into consideration that it is desirable to keep the dimensions of the magnet as small as possible and that a suitable value for the maximum magnetic field B is of the order of 1 T, we arrive at a bending radius ρ of 0.4 m.

3.3. Design of the magnet

To unite the properties mentioned above in one sector magnet was the most difficult and time consuming part of the design of the spectrograph. A large number of adjustable parameters should be included in the design. An obvious solution is to use a split-pole magnet as invented by Enge et al.[74,0]. Such a magnet has 4 pole faces, and thus 4 pole face angles and pole face curvatures. In addition it has two deflection angles, one for each of its sector magnets, yielding a total of 10 adjustable parameters. Another possibility is a single sector magnet provided with a field gradient and curved pole faces. In such a design there are 9 adjustable parameters: 2 pole face angles and curvatures, 1 deflection angle and 4 parameters associated with the pole face shape. For each configuration the magnetic field should be known in 3-dimensional space.

In principle there are three ways to determine this field:

- By measuring the field. This requires a precision XYZ table moving the field measuring probe between the magnet poles. Of course the field can only be measured for existing magnets. The results of such measurements (for instance the shape of the fringing fields) may be used for a new design.
- By calculating the field by solving the Maxwell equations in 3D for the magnetic configuration, including the coil configuration. Programs have been developed for this task, which use finite element methods [0]. This type of calculation is time consuming and cannot be used for large-scale parameter optimization.
- By applying (simplifying) models for the field calculation. In such models the field inside a sector magnet is constant if there is no field gradient. In the presence of a field gradient the field in the central plane of symmetry is given by:

$$B(x) = B_0\left(1 - n\,x/\rho + \beta(x/\rho)^2 + \gamma(x/\rho)^3 + \delta(x/\rho)^4\right) \qquad (3.1)$$

where B_0 is the uniform field in the centre and n, β, γ, δ are parameters.
The fringing fields at the entrance and exit of the magnet are given by the Enge function:

$$F(s) = \frac{1}{1+\exp\left[a_1 + a_2\left(\frac{s}{D}\right) + a_3\left(\frac{s}{D}\right)^2 + a_4\left(\frac{s}{D}\right)^3 + a_5\left(\frac{s}{D}\right)^4 + a_6\left(\frac{s}{D}\right)^5\right]} \qquad (3.2)$$

where a_i *(i=1,2,...6)* are six coefficients obtained by least-square fitting of measured field data in mid-plane, *s* is the distance from the effective field boundary EFB (Effective Field Boundary) measured along the central trajectory (see fig. 3.5) and *D* is the pole gap. At the EFB the value of the line integral of the (constant) magnetic field between the poles minus the actual field (calculated from a place where the field is constant going away from the poles) is equal to the value of the line integral of the field calculated from far outside the magnet going in the direction of the magnet (see fig 3.4). For the finite-element calculation the EFB does not enter into the equations.

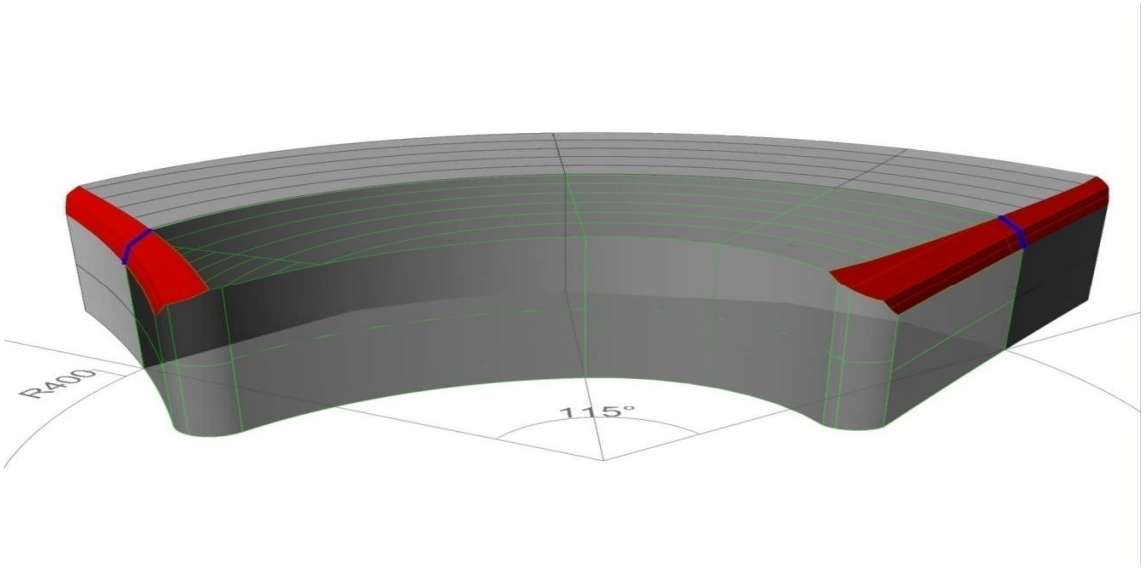

Fig. 3.3. *View of the pole shape as used in our final design. The Rogowski shape of the pole faces is indicated in red. This shape is highlighted by a blue line at the cross-section through the central trajectory. Both tilts and curvatures of the pole faces are visible.*

Formula 3.2 gives the field in the central plane of symmetry. The parameters of this function depend on the shape of the pole faces, for which normally an (approximated) Rogowski shape [0,0] is chosen. In fig. 3.3. the shape of the pole as used in our design is depicted. Here the Rogowski shape is approximated by three flat sections. The advantage of the use of a Rogowski shape is that the effective field boundary and the physical edge of the magnet pole coincide. This makes the designing process much simpler. The parameters of the Enge function are in part based on field measurements on magnets with this type of faces. The Enge function is also applied for describing the fringing field of magnets with a gradient field. Here it is important to note that it has been found that the focusing properties of a sector magnet do not depend critically on the shape of the fringing fields [0,0]. The magnet field along the central trajectory as calculated using the Enge function is indicated in fig. 3.4. Note that it deviates from the curve calculated with the finite element method (see below). The analytical description of the fields in the central plane of a magnet does not take into account the finite width of the poles (perpendicular to the central trajectory) and the resulting fringing fields on the sides. This implies that these descriptions can only be used in regions that are much farther away from the sides than the pole gap distance.

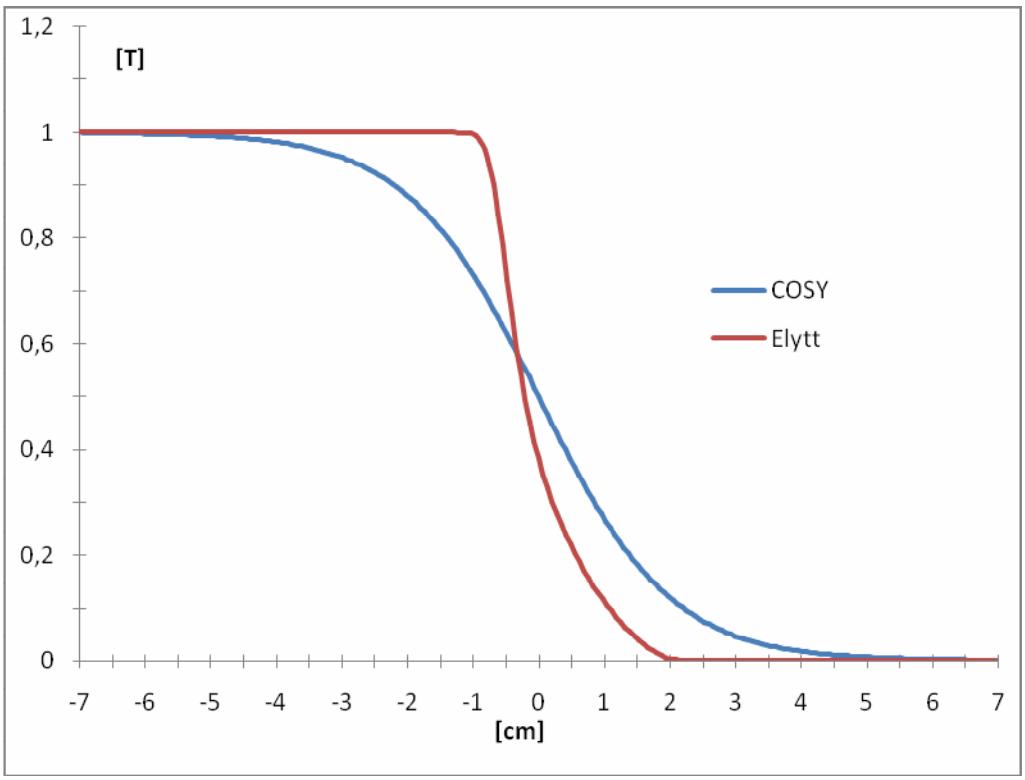

Fig. 3.4. *The fringing field in the mid-plane of the magnet with a pole gap of 11 cm. The origin of the horizontal axis is at the edge of the pole. The blue line shows the standard values from the program COSY (Enge function) and the red line shows the calculation with the finite-element method with the Rogowski profile as shown if the previous figure.*

Once the field in the central plane of a sector magnet is known from these models, the field outside the central plane is in principle known from the Maxwell equations in the entire vacuum between and outside the pole shoes [0,0,0,0].

In order to calculate the components of the magnetic field off the median plane, programs like RAYTRACE [0,11] take advantage of the symmetry of the optical element. The magnetic field components can each be expressed as a Taylor series in the transverse direction. By symmetry, we know that the transverse component will have only even terms, while the longitudinal components will have only odd terms. To third order in the RAYTRACE coordinate system, the expressions are given by:

$$B_x = (y/1!)\delta B_x/\delta y + (y^3/3!)\delta^3 B_x/\delta y^3 \quad (3.3)$$

$$B_y = B_y + (y^2/2!)\delta^2 B_y/\delta y^2 + (y^4/4!)\delta^4 B_y/\delta y^4 \quad (3.4)$$

$$B_z = (y/1!)\delta B_z/\delta y + (y^3/3!)\delta^3 B_z/\delta y^3 \quad (3.5)$$

Since the field B_y is only known as a function of x and z, we write, according to the Maxwell equations, for the partial derivates in these formula:

$$\delta B_x/\delta y = \delta B_y/\delta x \text{ and } \delta B_z/\delta y = \delta B_y/\delta z \quad (3.6)$$

Now the required derivates can be calculated numerically. For accurate calculations, or for magnets with a wide pole gap, higher order approximations are needed. Once the magnetic field is

known in 3D space, the ion trajectories can be calculated by numerical integration of the equation of motion in the field.

Alternatively, the properties of an ion-optical system may be described by a matrix, relating the vector describing the motion of an ion entering the system, with the vector at the end of the system. One of the best known programs using the matrix calculation method is TRANSPORT [0,12]. This program was also the reference for making other programs. Its notation is widely used in matrix calculations in ion optics.

In TRANSPORT notation (see fig. 3.5 for the coordinate system used) an ion trajectory is described at a certain point t_i, which is the distance along the assumed central reference trajectory, by a vector with six elements describing its position t measured along the "central ray", its distances x, y from the central ray, as well as the angles φ and θ the trajectory makes with the central ray in the yt and xt planes, the fractional momentum deviation δ of the ray from the assumed central trajectory and l the path length difference between the arbitrary ray and the central trajectory. Note that the central ray can be curved. Within a sector magnet it is part of a circle. The central ray is not necessarily a ray that can be followed by any ion. The ion-optical system is described by a number of elements at position t along the central trajectory, like a field-free space, a fringing field of a sector magnet, a quadrupole lens, etc. The action of each element is described by a matrix, converting the vector at position X_1 into a new vector at position X_2.

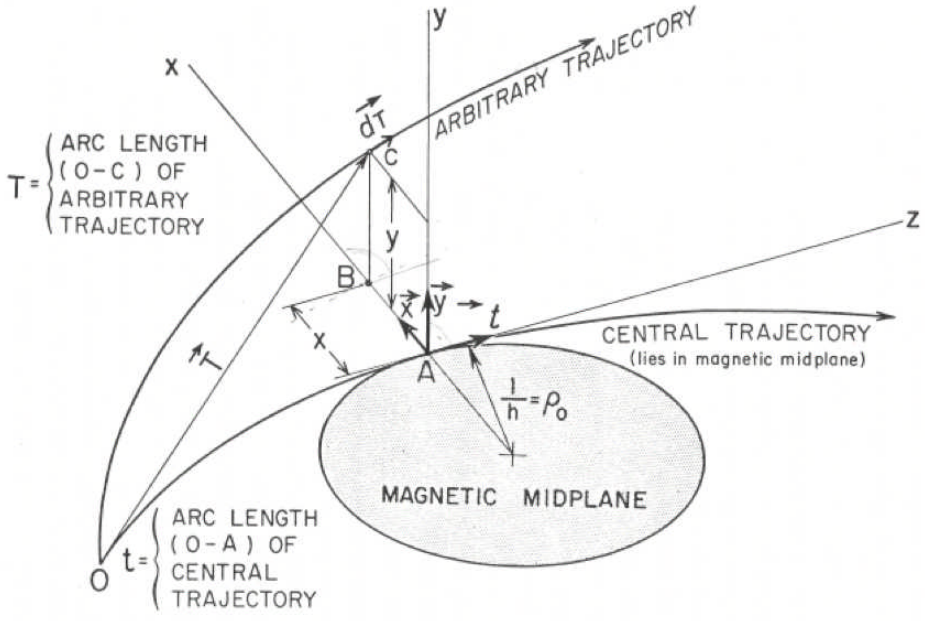

Fig. 3.5. *The original figure of the circular coordinate system used for deriving of the equation of motion for programs like TRANSPORT. This coordinate system together with notation is considered as a reference in most ion-optic programs.*

For the first-order calculations ion coordinates are described by a vector X_0 and the effect of an optical element is described by a matrix R. To first order the 6x6 matrix representing the optical element $X_1=R_0X_0$, can be written as:

$$\begin{bmatrix} x(t) \\ \theta(t) \\ y(t) \\ \varphi(t) \\ l(t) \\ \delta(t) \end{bmatrix} = \begin{bmatrix} R_{11} & R_{12} & 0 & 0 & 0 & R_{16} \\ R_{21} & R_{22} & 0 & 0 & 0 & R_{26} \\ 0 & 0 & R_{33} & R_{34} & 0 & 0 \\ 0 & 0 & R_{43} & R_{44} & 0 & 0 \\ R_{51} & R_{52} & 0 & 0 & 1 & R_{56} \\ 0 & 0 & 0 & 0 & 0 & 1 \end{bmatrix} \begin{bmatrix} x_0 \\ \theta_0 \\ y_0 \\ \varphi_0 \\ l_0 \\ \delta_0 \end{bmatrix} \quad (3.7)$$

There is a correspondence between the elements R_{ij} and properties of the ion-optical system:
R_{11} –magnification
R_{12} –focusing factor
R_{16} –dispersion
R_{26} –angular dispersion

The zero elements in the *R* matrix are a direct consequence of mid-plane symmetry. If mid-plane symmetry is broken, these elements will become nonzero.
The final position of an ion is given by matrix multiplication through all the elements in the system $X_n=R_nR_{n-1}...R_0X_0$. The precision of calculation is determined by the order of the Taylor expansion of the final coordinates of the particles as functions of the initial ones [0,0]. For example in TRANSPORT [19,20] notation, the Taylor expansion in $x_1,\theta_1,y_1,\varphi_1$ and σ for the x_2 element:

$$x_2(x,\theta,\varphi,\sigma) = (\delta x_2/\delta x_1)x_1 + (\delta x_2/\delta\theta)\theta + (\delta x_2/\delta\sigma)\sigma + (\delta x_2/\delta x_1^2)x_1^2 + (\delta x_2/\delta x_1\theta)x_1\theta + (\delta x_2/\delta\theta^2)\theta^2 + (\delta x_2/\delta x_1\sigma)x_1\sigma + (\delta x_2/\delta\theta\sigma)\theta\sigma + (\delta x_2/\delta\sigma^2)\sigma^2 + (\delta x_2/\delta y_1^2)y_1^2 + (\delta x_2/\delta y_1\varphi)y_1\varphi + (\delta x_2/\delta\varphi^2)\varphi^2 \quad (3.8)$$

This equation can be extended in a similar way to higher orders. For wide-angle sector magnets such calculations should be done up to about 9th order to get an accurate description of the system.

There are a few advantages to use a (higher order) matrix for the description of the focusing properties of an ion-optical system:

-Once the matrix is known, an arbitrary trajectory can be calculated very fast.

-A complicated ion-optical system may be split up into several components. The total response of the system is then obtained as a sequential matrix multiplication.

Also the system may be split along a plane (perpendicular to the central beam) at which information on the "beam" of ions transmitted through the system (such as beam divergence or diameter) is needed. In this way it is easier to get insight into the optical properties of a system than by ray tracing.

-The lowest order matrix elements have a specific meaning. It is good strategy to optimize (often minimize) the values of these matrix elements to design a system with certain properties. The momentum resolution depends on the terms affecting the image size of a monochromatic beam on the focal plane. For a small acceptance magnetic spectrograph, physical quantities as momentum resolving power, focal plane length and height, range of final angles and so on, are closely related with first- and second-order matrix elements. Such a description becomes more complicated for spectrographs with a large acceptance angle and additional, higher order terms are needed. But the first-order resolving power remains an important parameter to maximize during the process of designing of a spectrograph, and, once optimized, provides an easier starting point for higher-order corrections.

For the analytical functions describing the field as discussed above, analytical functions for the lower order matrix elements (up to 4th or 5th order) can be derived. With a computer program having the parameters of an analytic description of the field as input and having the (complicated)

expressions for the matrix elements in the code, an efficient optimization to 4^{th} or 5^{th} order of an ion-optical system is possible.

As a first step we chose the well-known and tested program TRANSPORT mentioned earlier, based on the matrix formalism. This program contains an analytical description of the magnet fields in the central plane, with parameters as described above. The field off the central plane is approximated by a second order Taylor expansion. The program also contains the code to describe the matrix elements relating the "ion vectors" at the entrance and exit of the system up to second order. The system may contain a number of elements, each described by a transfer matrix. In all present calculations "field clamps" are included, placed at a certain distance in front of and behind the spectrograph magnet(s). These rectangles of soft iron (see fig. 3.11) "quench" the field outside the magnets. The program also contains a description of how the beam envelope is changing during the propagation in the optical system. Each successful solution was tested with the program Turtle [13,14]. This program uses a similar matrix formalism, but instead of working with the beam envelope it is calculating the path for each ion up to third order. Finally we used a newer program COSY INFINITY [15,16,17,18], which can calculate transfer matrices up to sixth order and, after some modifications, up to ninth order. In this way two successful designs were obtained to be discussed in the next Sections. For the second design based on a single sector magnet, that was finally realized, the solutions were also tested with the program RAYTRACE [0,11] which solves with Runge-Kutta integration the equation of motion in the magnetic field as determined by the analytical description. Before producing this magnet, the calculated result was tested, because of the wide acceptance angle of the magnet. This was done by solving the Maxwell equation in 3D for the optimized configuration. In the calculation the shape and magnetic permeability of the soft iron of the poles and field clamps were taken into account, as well as the coil configuration. The total number of grid points on which the field was calculated was about $5x10^5$. Of course, use was made of the presence of a central symmetry plane. This test was executed by the Spanish company Ellyt [19], which finally also produced the magnet. Ellyt used the commercial program Ansys [0] for solving the Maxwell equations and an "own" raytrace program based on Runge-Kutta method to calculate the trajectories. We created also a similar program for ray-tracing ion trajectories based on the Verlet method to double-check the solution and to calculate the transformation matrix for ToF path length corrections. The Ansys program is not allowing the optimization of the magnetic field configuration to obtain optimum ion focusing properties. Because of that, the optimum solution can be found only by trial and error. In this procedure a 3D model of the dipole magnet is created. In the next step the magnetic field is found with the use of the Ansys program and finally the solution is tested by the ray-tracing program. To limit the number of calculations with the Ansys program, the only criterion applied to calculate the correction to the magnetic field was to obtain an approximate point-to point focus on the focal plane detector (100 x 15 mm) for all ions emerging from the sample and passing through the 2D detector foil at the entrance of the magnet.

3.4. Split-pole magnet design

The first design obtained with the described methods was an Enge-split-pole type of spectrograph [74,0,20] with flat and parallel poles. This solution was not tested with the Ansys program. The design is depicted in figs. 3.6 and 3.7. It consists of two sector magnets, both with a bending radius of 500 mm and bending the beam over 73º and 36.7º, respectively. The poles edges have an approximate Rogowski shape. The pole gap is 90 mm. The gap between the magnets is 200 mm. The object length (as measured from the EFB) is 750 mm and the distance from the end pole face (EFB) is 730 mm. The pole phase angles and curvatures of this design are indicated in fig. 3.8, together with the beam envelope inside this spectrograph.

In this design we obtained the conditions for perfect point-to point focusing on the focal plane detector with a magnification smaller than unity. It turned out that the realization of this

design would be very expensive, because of the total volume of the magnets. For this reason we tried to design a spectrograph with similar properties, but consisting of a single sector magnet.

It was found in continued efforts that a solution with a single sector magnet, with a field gradient and curved poles, was possible. Such a magnet is more compact and easier to produce. This leads to a large reduction of the costs.

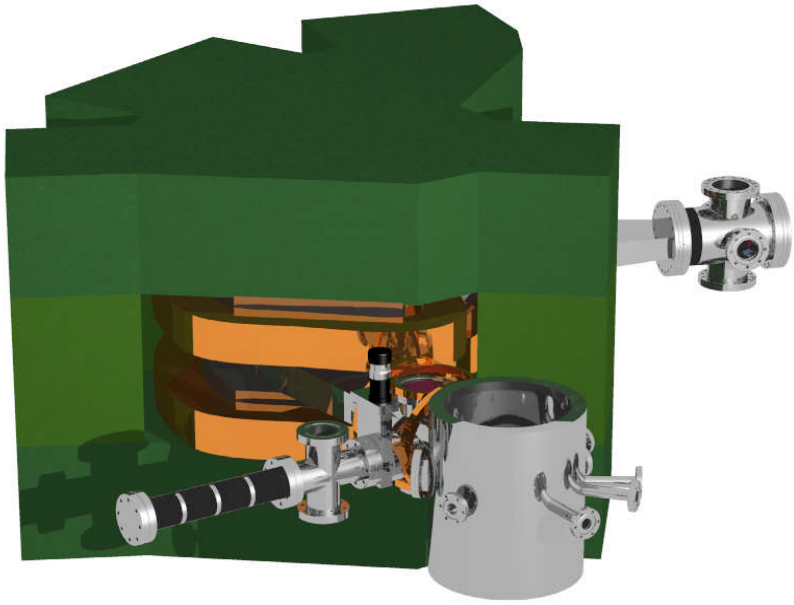

Fig. 3.6. *3D model of the split-pole magnetic spectrograph.*

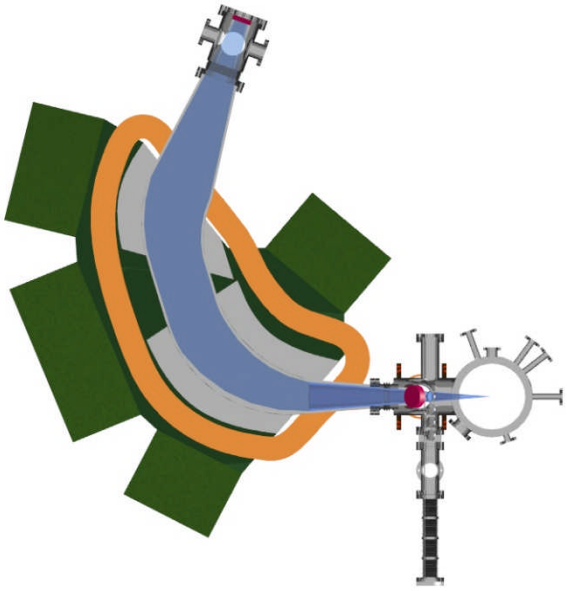

Fig. 3.7. *Cross-section of the split-pole magnetic spectrograph. The envelope of the ions emerging from the sample is drawn in blue and detectors are drawn in red.*

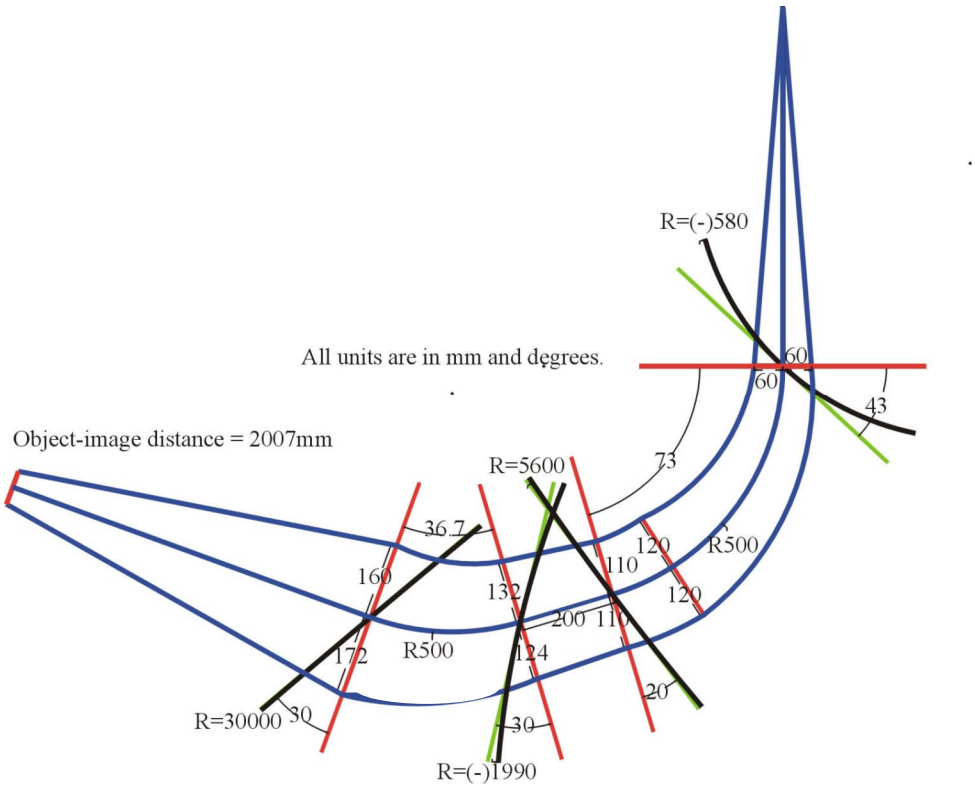

Fig. 3.8. *A cross section of the ion beam envelope in the split-pole magnet depicted with blue lines. The other lines indicate the design properties of the split magnet. The red lines are perpendicular to the central trajectory at the effective field boundaries. With respect to these lines the pole face angles are indicated by green lines. The actual curved shape of the pole faces is indicated by black lines. The values of the pole face rotations are indicated in degrees; the pole face radii of curvature are indicated in mm.*

3.6. Final design of the spectrograph with a single sector magnet

The final design was obtained using the sequence of programs TRANSPORT, Turtle, Raytrace, COSY as described earlier. To test the design, the Maxwell equations were solved in 3D space for the obtained configuration. This test showed that our result needed small, but important, modifications. The differences of the fields given by the parameters used in the analytical description and the field calculated by solving the Maxwell equations are shown in the figs. 3.9 and 3.10. The main cause for the differences seems to be the finite widths of the poles of the magnet. Another part of the deviation is due to the use of the Enge function to describe the field along the central trajectory (see also fig. 3.4). This part of the deviation is best visible in fig. 3.10. This last deviation may also be caused partly by the finite width of the magnet poles.

The solution obtained using the COSY program was corrected by the calculations by Elytt with the Ansys and ray-tracing program. They only changed the exit pole-face angle by 3.5 deg to compensate this difference. After this correction, the focusing properties were good enough to focus all ions into the focal plane detector.

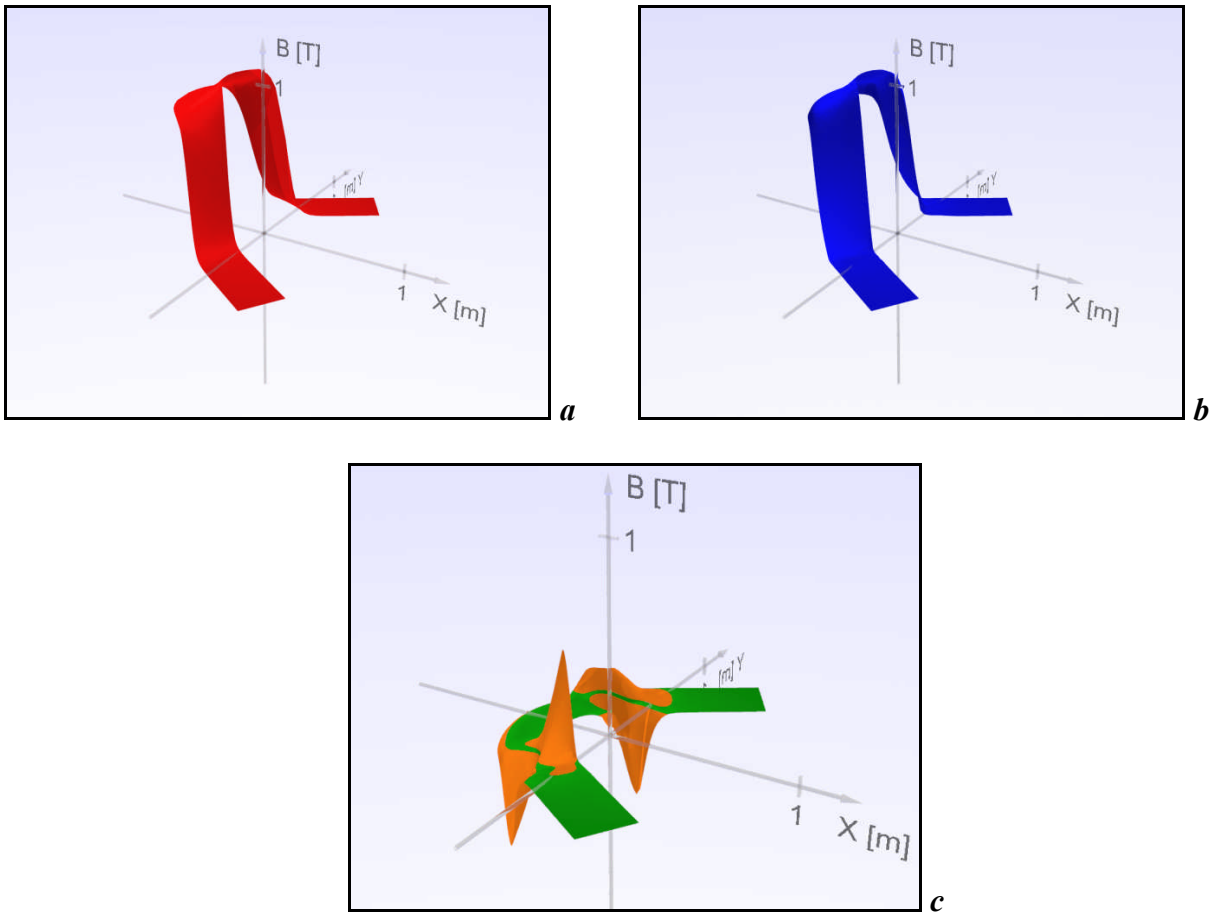

Fig3.9. a. *The magnetic field calculated using programs designed for ion optical calculation up to 9th order,* ***b****. the magnetic field calculated by solving the Maxwell equations in 3D,* ***c.*** *the difference between both calculations.*

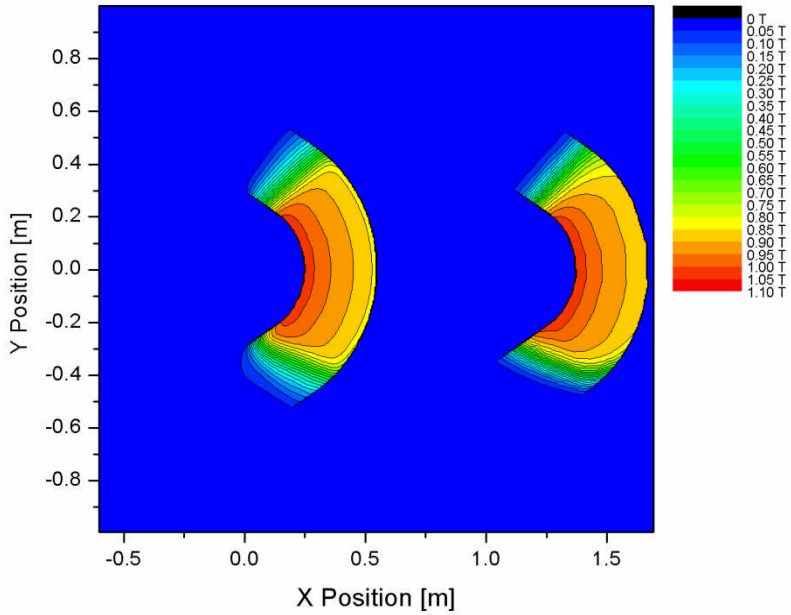

Fig.3.10. *Another comparison between magnetic field model used in matrix calculation based programs (left) with the magnetic field calculated by the finite element method program (right). In this figure the deviation due to the use of the Enge function to describe the field along the central trajectory (especially at the pole faces) is visible.*

The final solution obtained is a dipole magnet, with specially shaped poles as depicted in fig. 3.11. Details of the pole pieces are also shown in figs.3.2 and 3.3. The EFB of the magnet is at a distance of 800 mm from the sample. In the figure the field clamps can be seen. The bending angle of the central trajectory is 115º; its radius is ρ_0 = 400 mm. The maximum magnetic rigidity 0.4 Tm, corresponds to, for example, 2 MeV He^{+}, 8 MeV He^{++} or 4.56 MeV Si^{4+}. The edges of the poles of the magnet have an approximated "Rogowski" profile (approximated by two edges under angles 30º and 75º, respectively, with respect to the top plane of the pole, see fig. 3.3). The focal plane is flat and perpendicular to the central trajectory. Apart from the total bending angle and the distance of the focal plane, the following parameters were optimized to obtain an approximate point-to-point focus of the beam spot on the sample on the focal plane detector (15 mm high, 100 mm broad): 4 parameters describing the pole face angles and radii of curvature at the entrance / exit of the magnet and 4 parameters describing the shape of the pole planes. The figures of merit of the spectrograph are summarized in Table 3.6.1.

Table. 3.6.1. *Figures of merit of the magnetic spectrograph*

Max. field in magnet	1 T	Central gap	116 mm
Total deflection angle	115º	Pole face entrance angle	37°, curvature radius 1.15 m
Magnet radius	ρ = 400 mm	Pole face output angle	17.5°, curvature radius 10 m
Distance of EFB to sample Distance EFB- focal plane	800 mm 725mm	Magnetic field gradient	$B(x) = B_0(1-nx/\rho+\beta(x/\rho)^2+\gamma(x/\rho)^3+\delta(x/\rho)^4)$, n = 0.23, β = 0.22, γ = -0.1, δ = 0.2
Solid angle	14 msr ≈ 9º × 6º	Maximum rigidity	0.4 Tm
Energy resolution (as determined by the detector foil)	$\Delta E/E \approx 10^{-3}$	Angular resolution within solid angle	0.15º × 0.15º
Energy range	9%		

In Fig. 3.11 results of the trajectory calculations are presented for the final design. In fig. 3.12 the trajectories arriving at the focal plane detector are indicated in more detail. The spectrograph is not forming a precise point-to-point focus of the beam spot on the sample on the focal plane detector. The point of intersection with the focal plane depends of the angle with which the ion enters into the magnet as illustrated in fig 3.13.

Only the *x* position of the event is measured with the focal plane detector, it is also clear that the relation of this *x* position with the magnetic rigidity also depends on the *xy* position with which the foil was passed. This interdependence of the magnetic rigidity on both the *x and y* position in the first detector and the *x* position in the second detector can be taken into account in the data processing, if we assume that the trajectories are correctly reproduced by the transfer matrix.

Because the velocity of the ion is determined independently from the ToF, for each event the path length between the foil and the focal plane detector must be accurately known. Also this quantity can be calculated as a function of the position registered by the two detectors.

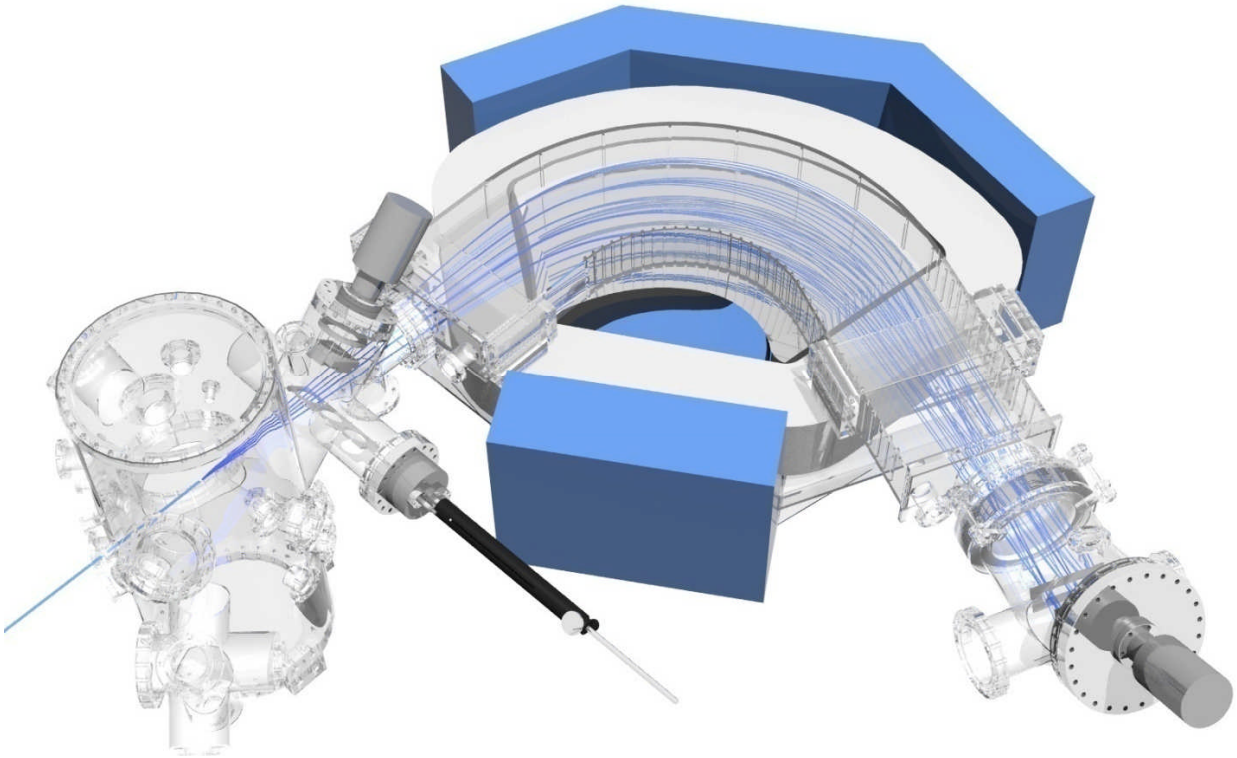

Fig. 3.11. *A computer-generated cross section through the magnetic spectrograph with ion trajectories (blue lines). The ion trajectories were calculated with a specially written finite-element program on the basis of the 3D magnetic field model as calculated by Ellyt. The field clamps before and after the magnet are indicated. Also the small plates fixed to the walls of the magnet chamber are visible. They serve to reduce forward ion scattering in the direction of the focal plane detector.*

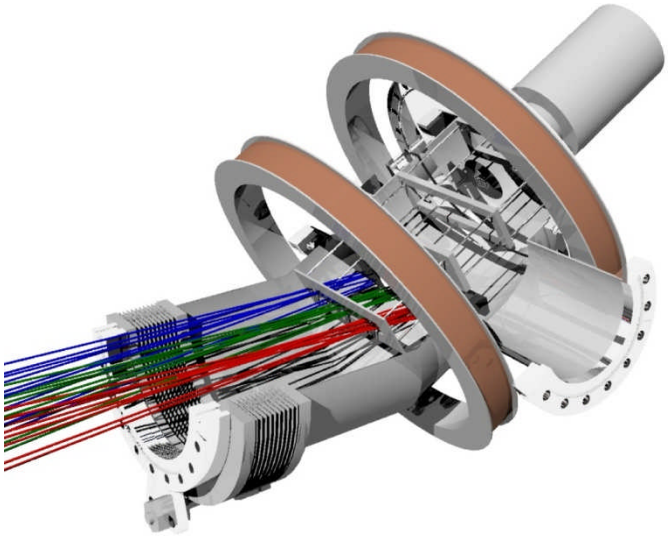

Fig. 3.12. *View of the ions (blue, green, red lines) entering with different energies the second detector mounted at the focal plane. The "detector" consists of a thin foil mounted on a grid through which the ions are penetrating. The secondary electrons emerging from this foil are accelerated to 300 eV by a voltage on a second grid placed at a distance of 1 mm behind the foil. As with the first detector (see below) the electrons are imaged on a channel-plate detector placed at a distance of 80 mm, using a magnet field generated by the indicated Helmholtz coils. This solution would give an almost 100% detection efficiency. Until now, this solution is not used, and the ions are hitting the detector directly. In this case the detector efficiency may be reduced by a factor of two.*

Detector frame

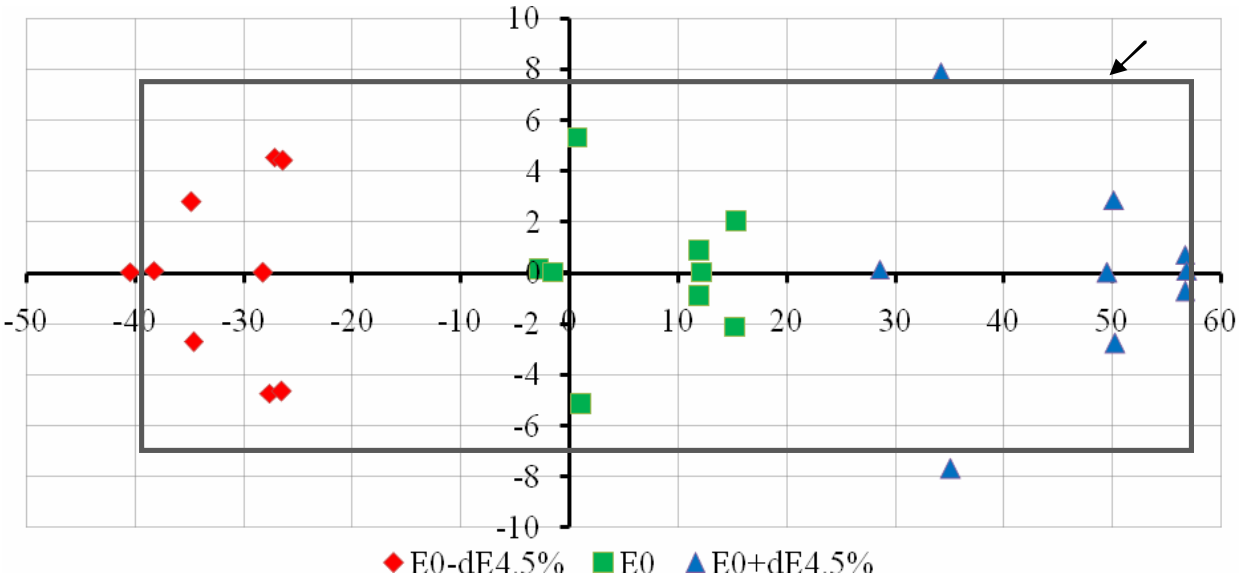

Fig. 3.13. *Points of impact of ions on the focal plane detector with a size of 100 x 15 mm. The points are calculated for 3 energies (differing by 4.5%) as indicated by colours and for 9 different angles per energy with which the ions are entering the spectrograph.*

3.7. Ion identification system

The problem with any spectrograph is identification of the mass m and charge q of detected ions [21]. For the ion identification a number of methods may be used. If electrostatic deflection is used, the deflection angle for a fixed transversal electric field applied over a certain distance, is proportional to q/E of the ions, where $E = \frac{1}{2} mv^2$ is the energy. If this is combined with magnetic deflection, which is proportional to q/mv, it is possible to determine m/q and v separately. Since q is quantized, both m and q can be determined separately as well, if cases like O^{4+} combined with C^{3+} are avoided. For ions with high energies in the tens of MeV range or higher the application of electrostatic deflection becomes difficult because of the required high field strengths. This method is used in some spectrographs in which a Wien filter is inserted as a velocity filter. In a Wien filter an electric field $\boldsymbol{E}$ and a magnetic field $\boldsymbol{B}$ are applied over a fixed length. Both fields are perpendicular to the main propagation direction of the ions and perpendicular to each other. The field strengths are chosen so that for the passing velocity v of the ions the perpendicular forces are equal and opposite, i.e. $q\boldsymbol{E} = -q\boldsymbol{v}\times\boldsymbol{B}$. Then $v = E/B$.

In some spectrographs part of the ion identification is achieved by using an energy dispersive silicon detector in the focal plane. Also a gas-filled ionization detector may be used. The specific energy loss of the ions in the gas can be determined in such detectors. Since this energy loss is a function of the charge number Z of the ion, the value of Z can be determined in addition to its total energy.

The ion identification in the spectrograph described in this thesis is achieved by measuring for each ion the magnetic rigidity mv/q and the velocity v. Again the mass m and the charge q of the ion can be determined separately from the measured data. The velocity v is measured by determining the Time-of-Flight (ToF) needed to cover the distance from the carbon foil at the entrance of the spectrograph to the focal plane detector. Ions emerging from the sample are passing through the foil and produce secondary electrons (see fig. 3.14). These electrons are focused with a combination of an electric and a magnetic field on a two dimensional (2D) position sensitive detector. This detector thus determines the angle of each incoming ion and is giving a timing signal, which is used, in combination with a timing signal delivered by the focal plane

detector, to determine the time of flight T. To find *v*, the path length of the trajectory is needed. As discussed later, this path length is derived from the trajectory length calculated using the transfer matrix of the spectrograph.

3.8. Main chamber and goniometer

The main chamber is attached to the vacuum chamber of the magnet via a short bellows, as shown in fig. 3.11. Its design was complicated by the restrictions in the distance between the sample position and the spectrograph. Two views of a 3D drawing of the chamber are presented in fig. 3.14.

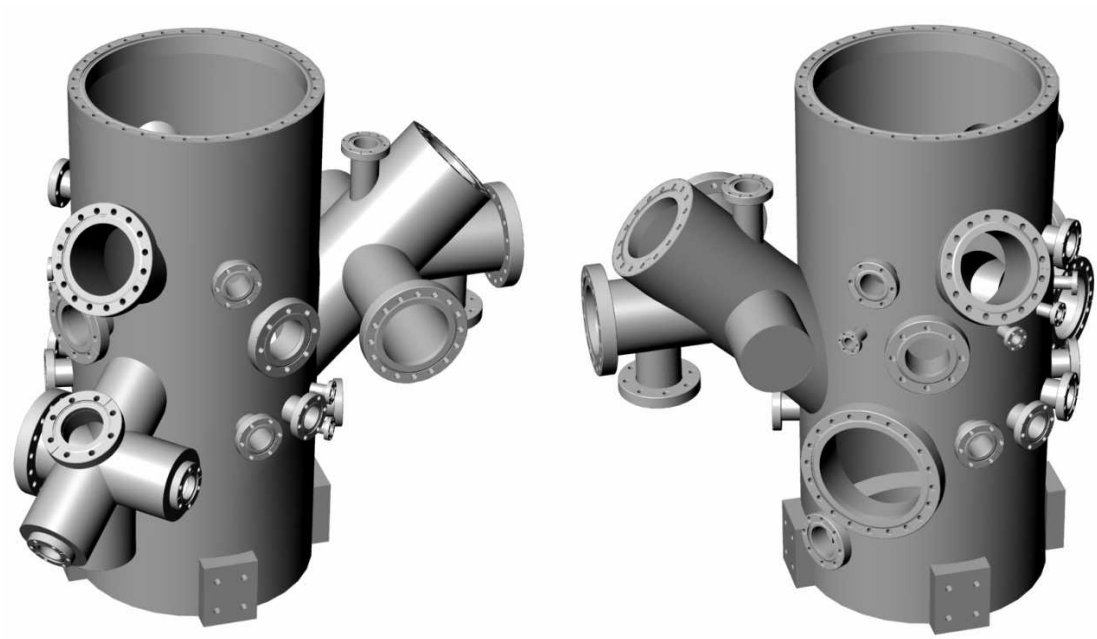

Fig. 3.14. *Views from different sides of the design of the main chamber.*

At the right of the left frame the side-pipe connecting the chamber to the spectrograph is seen. It contains the foil transfer system that can be moved horizontally. It also contains the 2D detector to be mounted on the flange at 45º with the horizontal plane, as well as the rest of the angle and event detection system (see next Section). A five axis goniometer (see fig. 3.15) is to be mounted on top. The size of this goniometer determines the diameter of the chamber, which is 355.6 mm. The sample introduction system (see Section 3.13) is to be mounted on the side-pipe on the front-left side of the left frame. The big flange above this structure is for a viewport. The big flange visible at the front side of the right frame is for mounting a 1200 l/s turbo pump. In addition there are flanges to mount Ti-sublimation and ionization pumps. The four small flanges visible at half height in the right-hand frame are for connecting the chamber to the beam line. In total there are five such flanges. The chamber is mounted on the spectrograph frame using the mounting pieces at the bottom.

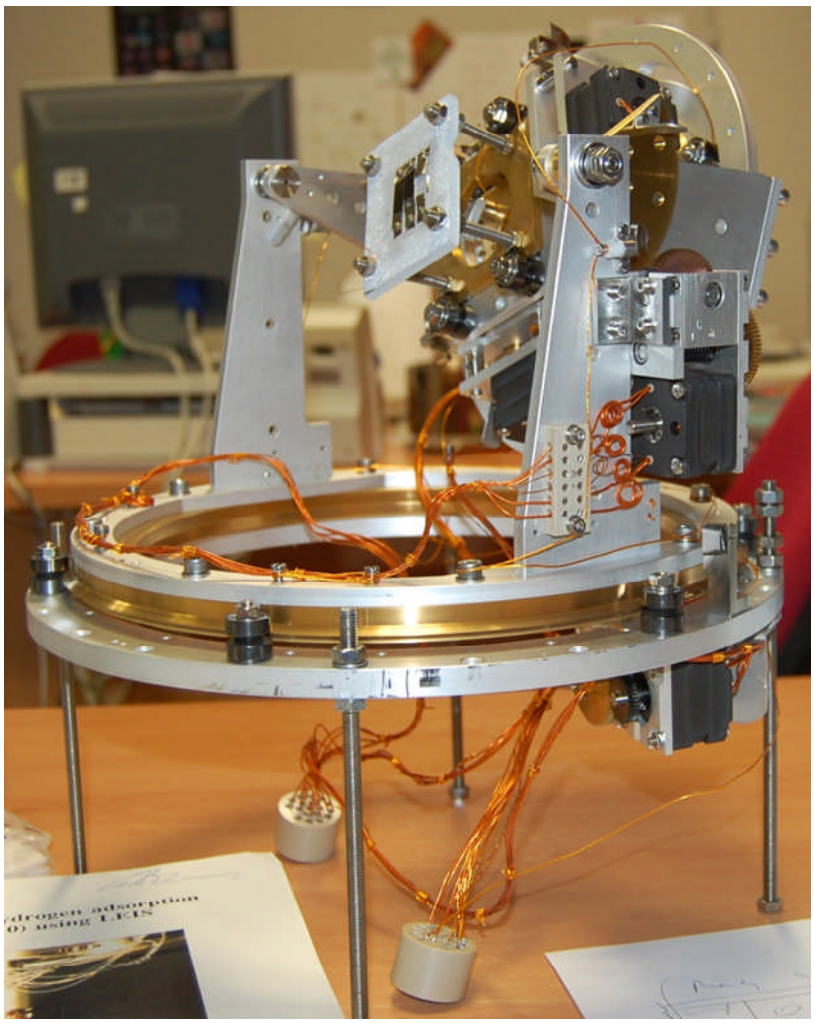

Fig. 3.15. *Photo of the 5-axes goniometer for the magnetic spectrograph. The UHV compatible goniometer is mounted (upside down) on the top flange of the main chamber of the spectrograph. It has a vertical axis, a horizontal axis and an inner "spin axis" for precision (reproducibility < 0.1°) sample orientation. All movements are activated by internal (UHV compatible) stepper motors (blue-grey boxes). In addition it has an X-Y translation table with a stroke of 15 mm, on which is sample holder is to be mounted. The goniometer was designed by L. Venema of the Groningen University.*

3.9. Angle and event detection system

3.9.1. Introduction

The ions are passing through a thin foil before entering the spectrograph.. A number of low-energy (E< 30 eV) secondary electrons are emitted from this foil upon the passage of an ion. These electrons are then focused on a 2-dimensional (2-D) position sensitive detector, such that a one-to-one image is formed, see fig. 3.16. The position of impact of the electrons on this detector determines the intersection point of the ion with the foil. The time of the passage of the ion is derived from the electronic response of the detector. This feature allows the use of a large solid angle of the spectrograph. With the known entrance angle of each ion, each event can be corrected for the shift in kinematic factor and length of ion trajectories in the sample, that both depend on the emission angle of the ion from the sample. With these corrections the concentration depth profile of isotopes in the sample can be determined in an efficient way. If the sample is mono-crystalline then

the intensity of the ions observed within the detection cone will exhibit an angular distribution (blocking pattern), characteristic for the crystal structure. For the observation of a relevant part of such blocking patterns the solid angle of the spectrograph (detection cone) should be larger than 5º x 5º. The angular resolution with which these patterns should be observed is about 0.1º.

The optimization of the solid angle was an important issue during the process of the design of the spectrograph. To avoid that the gap between the poles inside the magnet becomes too large, it is necessary to place the magnet close to the sample. The main vacuum chamber contains the sample mounted on a 5-axes goniometer, see fig. 3.15. The diameter of this chamber cannot be less than 355.6 mm. Another consideration is the maximum size of the foil and available 2-D detectors giving the required spatial resolution (~ 40 mm diameter). Finally it was decided to place the foil at 250 mm from the sample. The circular foil has a diameter of 41 mm and is tilted by 45º with respect to the central trajectory, to face the detector. The detector has a circular detection area with a diameter of 40 mm. This solution is giving an elliptical detection cone of 6º×9º (~14 msr) of scattered or recoiled ions which are passing through the foil, see fig. 3.16.

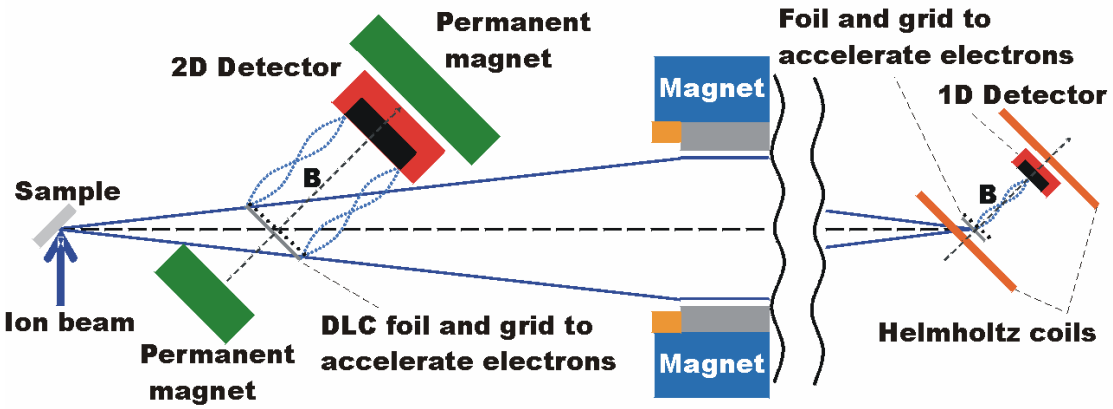

Fig. 3.16. *Schematic view of the detection system in the magnetic spectrograph.*

3.9.2. Detector foils

The next issue was the acquisition of the foil. The foil should be homogeneous and as thin as possible. The energy straggling in this foil is the factor which determines the resolution of the spectrograph. The minimum thickness available is about 4 nm. This thickness can be obtained for carbon or Mylar foils, supported by a fine mesh [22,23,24]. Such supported foils, but with much smaller lateral dimensions, are used in electron microscopy, and also in Time of Flight (ToF) detection systems for ions [25,26,27,28,29,30,31]. The foils are made by depositing the material (carbon, Mylar) onto a polished glass plate covered with a layer (Sugar, boron oxide) that can be dissolved in water. The foil can be stripped off the substrate by immersing the glass plate in water, possibly with some dissolvent added. The foil is then floating on the water and can be fished up with the supporting grid. We did not try to develop this technique in our laboratory. Instead we were seeking collaboration with dr. Liechtenstein (Kurchatov Institute, Moscow), who finally has produced the foils. The 5 nm thick diamond like carbon (DLC) foils with a diameter of 41 mm are mounted on supporting Cu meshes with a pitch of 50 µm and with a wire thickness of 6 µm . The foil is shown in fig. 3.17.

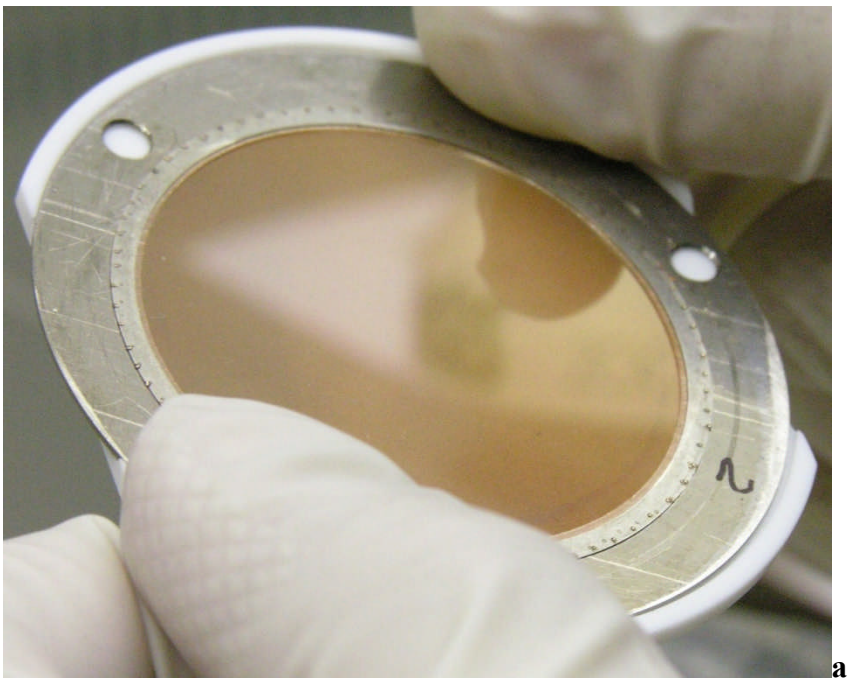

a

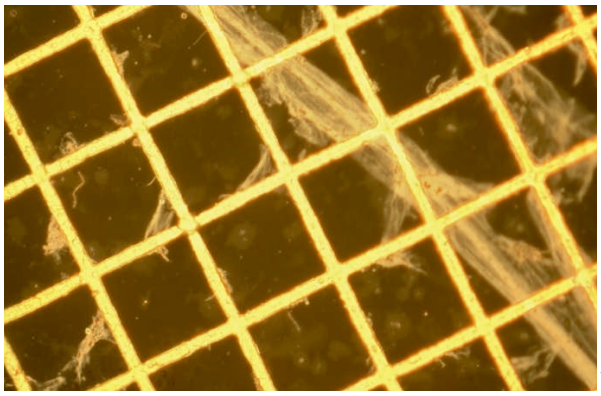

b

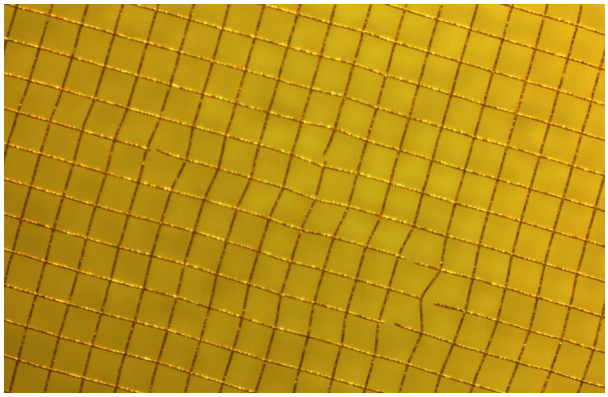

c

Fig. 3.17*. Photo and microscope images of the foil.* ***a*** *Foil on a supporting mesh mounted in a ring which is placed in a wider ceramic ring.* ***b*** *Detail showing broken parts and some dirt.* ***c*** *Detail, showing broken wires of the mesh.*

The foil with the grid has a transparency of approximately 70%. A second grid with a transparency of 80% is mounted at a distance of 1 mm from the foil, to accelerate the electrons. The total transparency of some 55% is not a problem. A fixed part of the ions entering the spectrograph is intercepted. This loss of efficiency can be easily compensated by increasing the beam intensity. Transportation, moving and any operation with the foil should be done extremely careful to avoid damage. The setup contains three DLC foils mounted on a transfer rod, see fig. 3.18. In case a problem occurs, the foil can then be replaced, without breaking the vacuum. When the thin foils are stored in the ambient, a layer of water, CO_2, etc. is absorbed, which adds significantly to the thickness. This layer should be removed by baking the foil in vacuum [32,34]. We have not tried this so far, because there are other problems with the foils as evidenced by inspection under a light microscope, see fig. 3.17. As can be seen in the microscope images there are three types of problems:

-At some places the grid is broken. At these places the foils have tears.
-The surface is covered with some dust. The estimated fraction of the area covered is probably less than 1%

-Large areas of the foil are covered with something appearing to be small crystallites. Possibly this is the residue of something dissolved in the water used for stripping. This will have a major influence on the homogeneity of the energy loss and straggling.

The thickness, smoothness, energy and angular straggling of similar foils from the same supplier were tested at the Jyväskylä Accelerator Laboratory with ToF (private communication with A. Muñoz Martin). A variation in the energy loss and straggling was found, exceeding by far the mean energy loss value claimed for the foil.

Recently we purchased (from Precision-eforming, Cortland, NY 13045 USA) grid made by electro-deposition on a micro-patterned substrate. They have a "wire" thickness of 20 μm, a pitch of 82 μm and a transparency of 66% [33]. They will be covered with Mylar or with carbon foils with a thickness of 5 nm.

The energy resolution of the spectrograph is determined by the energy straggling in the foil. Also inhomogeneities will contribute. The calculated energy straggling for a foil thickness of $\sqrt{2}$ x 5 nm is about 2 KeV for 1 MeV He ions, meaning that the relative energy resolution is $\Delta E/E \approx 2\times10^{-3}$ for low energy He ions. The energy and angular scattering were calculated doing simulations of ion trajectories and energy loss processes using a program created by V. A. Khodyrev [35], and with SRIM [36,37]. Examples of the output of the programs are plotted in fig. 3.19. For a spectrograph without a foil this resolution can be better by an order of magnitude. Still the calculated resolution is sufficient to obtain a resolution in depth profiling of better than 1 nm. This is also true for different ion energies or species. Here the straggling may be larger, but then also the stopping power is larger. To first order it is the ratio between these quantities that determines the depth resolution. As can be seen in fig. 3.19, the angular straggling is for He less than 0.1º for a foil thickness of 7 nm ($\approx 5\sqrt{2}$). The angular spread decreases with increasing energy, and with the mass of the ion. The spread is lower than the angular resolution of the spectrograph.

Fig. 3.18. *3D design of the holder on a linear transfer system, with 3 rings containing the foils. In each position a ring with the foil on a mesh is mounted in a ceramic ring. In addition a second ring with a mesh is mounted at a distance of 1 mm from the foil grid. The foil is at a potential of -300 Volt, so that the electrons emerging from the foil are accelerated towards the second foil which is at ground potential.*

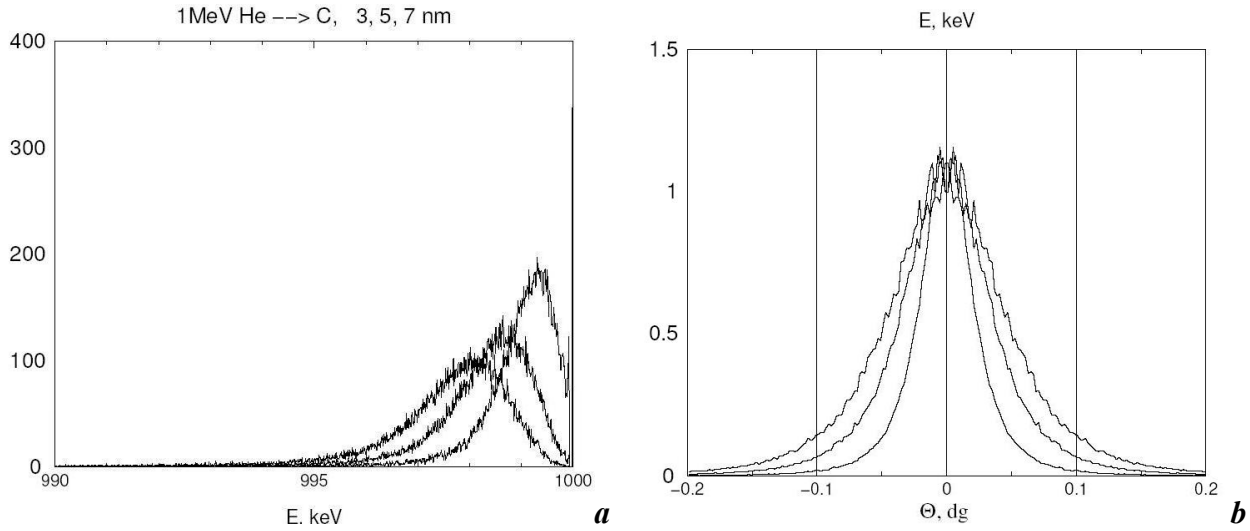

Fig. 3.19. *Simulation of energy (**a**) and angular straggling (**b**) of He ions after passing an amorphous DLC foil with various thicknesses as indicated*

3.9.3. Secondary electron generation

The emission of secondary electrons is closely related with the electronic energy loss. Like in electronic energy loss, two main mechanisms contribute to the emission of secondary electrons upon the passage of an energetic ion through the foil. Part of the electrons is emitted as a result of electronic excitation by the electro-magnetic field of the fast ion. These electrons have a kinetic energy << 100 eV. Another process is kinetic emission, caused by direct transfer of kinetic energy from the impinging projectile to the electrons in the target material. The resulting δ electron can have a much higher energy, up to some 5 keV. These high-energy electrons are emitted in forward direction and produce in their turn secondary electrons with a lower energy. The total number of electrons emitted in the primary processes is proportional to the electronic energy loss per unit path length dE/dx. The total yield of low-energy electrons is higher in forward directions than in backward directions [38,39], however in forward direction a fraction of the electrons will have energies which are in excess of 100 eV. The number of electrons is also determined by the mean free path of the electrons in the foil. Using the data of reference [38] we calculated that a 2 MeV He ion creates on average 5 electrons in forward direction. For heavier ions like He, N, O, Ar, Si, in the energy range of interest the number of low-energy electrons emitted in forward direction is even higher. Only for H this average number of electrons is ~1, so that some H ions are not detected with the first detector. As can be seen in fig. 3.16, we placed the detector after the foil to detect electrons emitted in forward direction.

3.9.4. Charge equilibration

As stated above, a clear disadvantage of using a foil is the loss of energy resolution, while the clear advantage is the ability to measure the angle of the ions entering the spectrograph. However there is an important additional advantage in using the foil. The foil is thick enough for charge equilibration. This means the charge distribution of ions emerging from the foil is independent of the charge state of the ions before the foil as illustrated in fig. 3.20. In a spectrograph without a foil only one charge state of the scattered or recoiled ion is measured. This is a big problem for the measurement of concentration depth profiles, because the fraction of the measured charge state (compared to all charge states) should be known. In general this is not the case. For structure determination by comparing measured angular distributions with simulated results obtained for trial structures the problem is even bigger. The angular distribution will be

different for different charge states. This is because the charge state depends on the precise trajectory of the ion. This problem is removed because we measure effectively the sum of all charge states before the foil, by detecting only one charge state after the foil. The fraction of ions with a specific charge state after the foil is entirely determined by the foil. The charge distribution of ions (and also the charge equilibration) is well investigated for carbon foils, because these have been used since decades as stripper in tandem accelerators. A small remaining item is that the number of secondary electrons generated by the ion depends slightly on the charge state of the ion. Because the number of secondary electrons will be >> 1, this will hardly influence the detection efficiency for the different charge states.

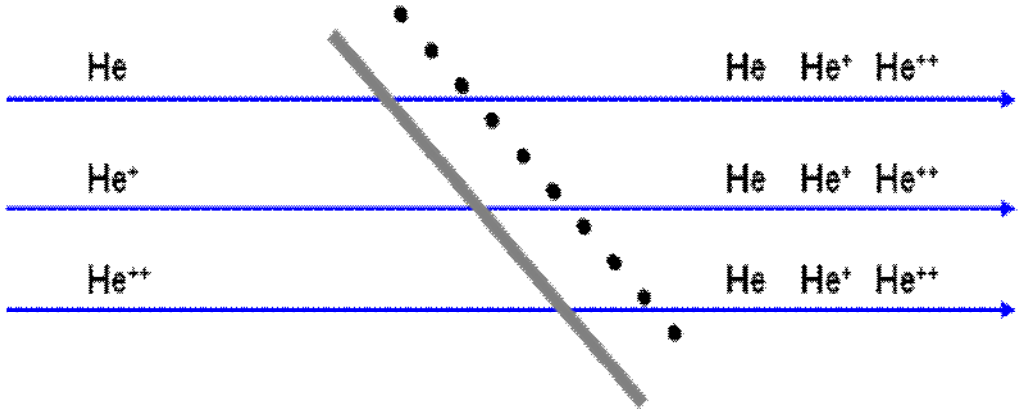

Fig. 3.20 . *Schematic concept of the charge equilibration process in the magnetic spectrograph. The DLC foil is indicated in grey and the black dots indicate the acceleration grid.*

3.9.5. System for focusing of electrons on the detector

Downstream of the foil, at a distance of one mm, a metal grid is placed. The secondary electrons emitted from the foil after the passage of an ion are accelerated to 350 eV, by applying a negative potential to the foil grid and ground potential to the metal grid. The foil and metal grids are mounted on a holder connected to a transfer rod which is also providing the electrical connections (see fig. 3.18). The foil and metal grid are separated and isolated by ceramic rings. The accelerated electrons are focused with a 50 Gauss magnetic field generated by permanent magnets onto a 2D position sensitive micro-channel plate (MCP) detector, placed at a distance of 80 mm from the foil. The direction of this guiding field is normal to the plane of the foil and detector (see fig. 3.16). The implementation of the focusing system in a side-pipe of the main chamber is shown in fig. 3.21.

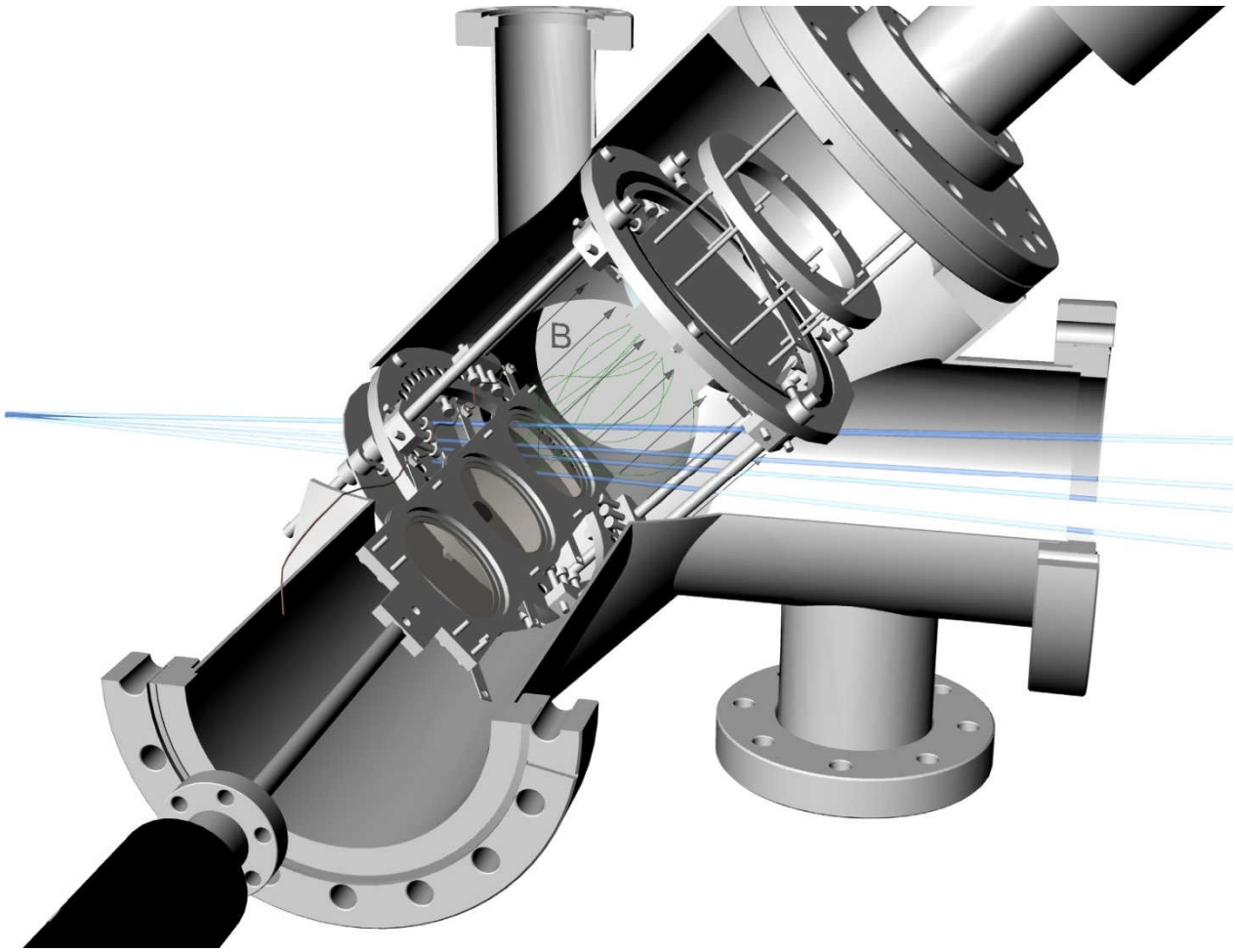

Fig. 3.21. *View of the focusing system. The "beam" of ions passing through the foil is indicated with blue lines. The magnet field B is depicted by vectors, around which the spiralling trajectories of the electrons are drawn in green. The detector is to be mounted at the height of the upper ring with magnets at a distance of 80 mm from the foil.*

The method of focusing of electrons emerging from the foil onto the detector is as follows: for the selected distance *d* from the carbon foil to the detector, the accelerating voltage U_y and the guiding magnetic field B_y normal to the foil plane are chosen in a such way that secondary electrons make one full turn around the helix that corresponds to their trajectory (Lorentz focusing). Electrons are emitted from the foil with energy E_e and components of the velocity Δv_x in the plane of the foil and Δv_y normal to the foil. With m_e the electron mass, q_e the electron charge, R the radius of the helix and T the time for one turn (and for covering the distance *d*), we get:

$$R = \frac{m_e \Delta V_x}{q_e B_y} \qquad T = \frac{2\pi R}{\Delta v_x} = \frac{2\pi m_e}{q_e B_y} \text{ independent of } R. \tag{3.9}$$

If this time is equal to the time $\frac{d}{v_y}$ needed to cover the distance to the detector, there will be perfect focussing. With $v_y = \sqrt{\frac{2q_e U_y}{m_e}}$ the relation between U_y and B_y for focussing is obtained as:

$$\frac{q_e B_y^2 d^2}{8\pi^2 m_e} = U_y \tag{3.10}$$

For d = 80mm and B_y = 50 Gauss we get U_y = 356V. In the derivation it is assumed that Δv_y is zero. If Δv_y is finite, then the spiral is not completed when the electrons hit the detector. The hitting point is missed (as measured along the projected circle of the spiral) by a distance

$$a = 2\pi \frac{\Delta v'_y}{v_y + \Delta v'_y} R \cong \frac{\pi m_e}{q_e B_y} \frac{\sqrt{\frac{m_e}{2}} \Delta v_y^2 \Delta v_x}{v_y \sqrt{q_e U_y}} \qquad (3.11)$$

The extra velocity acquired by the electrons with initial velocity Δv_y after being accelerated in the field between the grids is here approximated as $\Delta v'_y \approx \frac{1}{2} \Delta v_y \sqrt{\frac{E_y}{q_e U_y}}$. Here E_y is the kinetic energy corresponding to v_y. **In addition we have $\Delta v'_y << v_y$.**

For $\Delta v_y^2 + \Delta v_y^2$ fixed by the energy E_e of emission from the foil, a maximum value for $\Delta v_y^2 \Delta v_x$ (see eq. 3.10) is obtained for an emission angle of 35.26º with the normal of the foil. This gives $\Delta v_y = \frac{\sqrt{2}}{3} v_e$ and $\Delta v_x = \sqrt{\frac{1}{3}} v_e$. **Here v_e is the velocity corresponding to E_e.** Now, we can write:

$$a_{max} \cong \frac{2}{3} \pi \frac{E_e}{q_e U_y} R, \qquad with\ R = \frac{\sqrt{\frac{2}{3} m_e E_e}}{q_e B_y}. \qquad (3.12)$$

For the values used in our setup ($B_y = 50$ Gauss and U_y = 356 V) we get the results depicted in Table 3.9.1.

E_e (eV)	R (mm)	a_{max}
10	1.18	0.07
20	1.16	0.19
60	2.88	1.00
120	4.07	2.82 (2.70)

Table 3.9.1. *The spiral radius R and the maximum deviation a_{max} (measured along the circle of the projected spiral) tabulated as a function of the electron energy E_e of emission from the foil. The linear deviation (if different) is indicated in brackets.*

For emission energies in excess of 20 eV the (maximum) blurring by the focusing system beyond 0.2 mm is a problem. In practice the blurring can be limited to 0.2 mm if U_y is lowered so that the system is tuned for perfect focusing for E_e = 20 eV. Then only emission energies > 40 eV give rise to inaccurate focusing.

There are a few options to tackle this problem.

The first option is to reject events in the data manipulation phase. This could work if, besides the electron with a too high energy, also low energy electrons would hit the detector simultaneously, as would be normally the case. Then the position is not uniquely determined and the "sum check" (see section 3.9.8) could fail. However, it is questionable if the sum check can be made sufficiently stringent.

The second option is to place the detector at the backside of the foil, where the high-energy electrons are absent. Maybe this is the best solution. The realization of this option is not compatible with the application of a Wienfilter as discussed in Section 3.9.7.

The last option, to increase U_y and B_y is incompatible with the use of the channelplate detector. If this detector (see Section 3.9.6) is placed in a magnetic field in excess of some 50 Gauss, the position resolution will be affected.

The best solution to create a uniform tuneable magnetic field as needed for the system is the application of Helmholtz coils to be placed outside or inside the vacuum chamber. However, there is no space for the coils at these locations. Therefore, we chose to create the field using permanent magnets. Since the permanent magnet configuration is rotational symmetric, it was calculated in 2D using the finite element method with the program FEMM [40]. The solution was found by trial and error. The final system consists of two rings with 800 mm diameter each containing 53 small rectangular permanent CoSm magnets of dimensions 10x6.5x4 mm, magnetized in a radial direction. One ring has the magnetization vector pointing outwards and the second one inwards (see fig. 3.22). In addition there are two small disc-shaped magnets with a diameter of 10 mm and a thickness of 2 mm, magnetized in axial direction, to obtain a correction of the magnetic field. We chose CoSm as the material for the magnets because of its high magnetization, and good vacuum properties. The material can be baked up to 300C° without losing its magnetization. The whole system is clamped with screws against the wall of the chamber (pipe) for the detector. It also contains a diaphragm with a circular opening to prevent (scattered) ions and electrons outside the detection cone to reach the foil or the detector. These particles would give rise to additional counts in the detector. This diaphragm is made from two parts placed at a certain distance from each other in order not to reduce the pumping speed of the system.

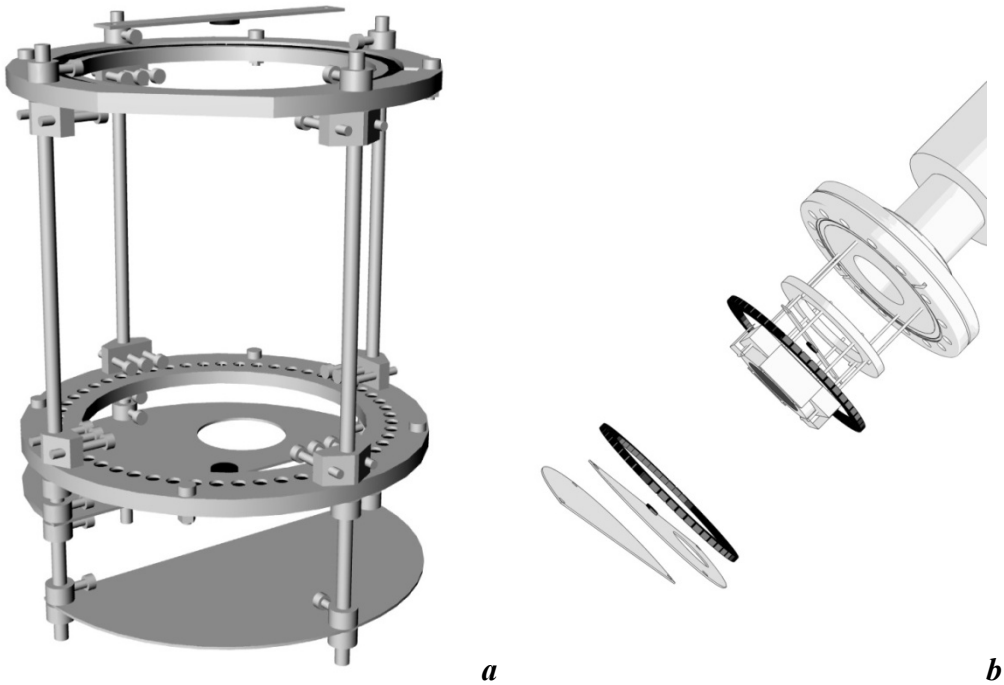

a ***b***

Fig.3.22. a *3D image of the permanent magnets holder together with the magnet rings and the two permanent magnets (in black)* ***b*** *configuration of the permanent magnets (black) together with the 2D detector, which is at the height of the top magnet ring.*

The map of the magnetic field generated by the magnets can be seen in fig.3.23.

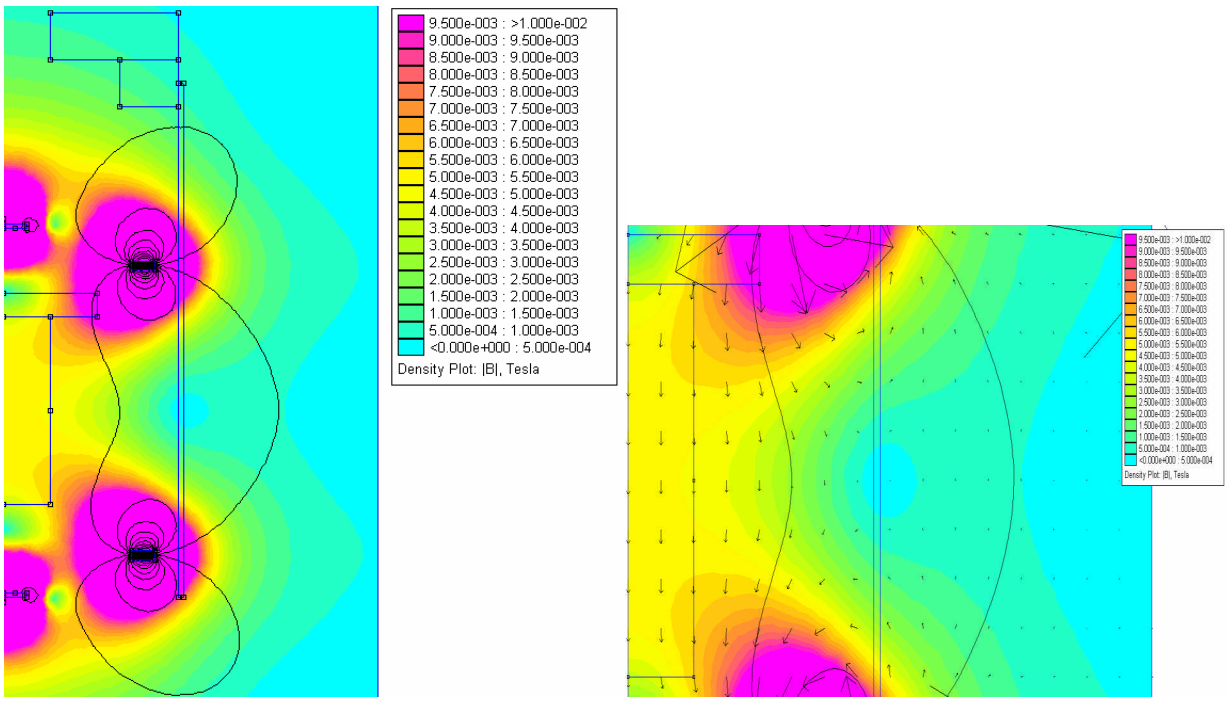

Fig.3.23. *2D maps of the rotational symmetric magnetic field generated with the program FEMM. The picture at the right is a magnification of the central part. A homogenous field region of ~50 Gauss is present in the rectangular areas on the left side of the pictures (yellow). Regions with a high magnetic field (purple) are present around CoSm magnets. The positions of the 2D detector and of the walls of the vacuum chamber are indicated.*

3.10. The position sensitive channelplate detectors

The spectrograph is provided with a 2D position sensitive detector to detect the electrons emerging from the foil, and a second, 1D position sensitive, detector to detect ions in the focal plane of the spectrograph. Both are multi-channelplate (MCP) detectors, provided with delay-lines [41] for the determination of the impact position. This type of detector was chosen because of its short recovery time (20 ns), the good position resolution (0.15 mm in X and Y directions for the 2D, and 0.3 mm for the 1D detector) and the steepness of its electronic pulses, allowing accurate timing of the events. The count rate capability of this type of detector is a few Mega counts/s.

The channelplates of 1 mm thickness are made from lead glass capillaries joined together into a matrix (see fig. 3.24). Typically the capillaries make a small angle (~8º) with the surface normal to prevent channeling effects for perpendicular incidence of the irradiation. The capillaries or channels are coated to obtain a high secondary electron coefficient and some small conductivity allowing charge replenishment. When charged particles or photons with sufficient energy collide with the channel walls one or more secondary electrons can be generated, that are accelerated to the back side of the channel by an electric field generated by a DC voltage of approximately 1 kV applied over the plate. The accelerated electrons have sufficient energy to knock out further electrons upon their frequent collisions with the capillaries, so that an avalanche of electrons is created. The top and bottom surfaces are coated with metal to provide parallel electrical contact. To increase the electron multiplication efficiency, two channelplates are used in tandem with the plates rotated by 180º so that the channels are in a chevron configuration. Electron multiplication factors of up to 10^6 are achievable with such composed detectors.

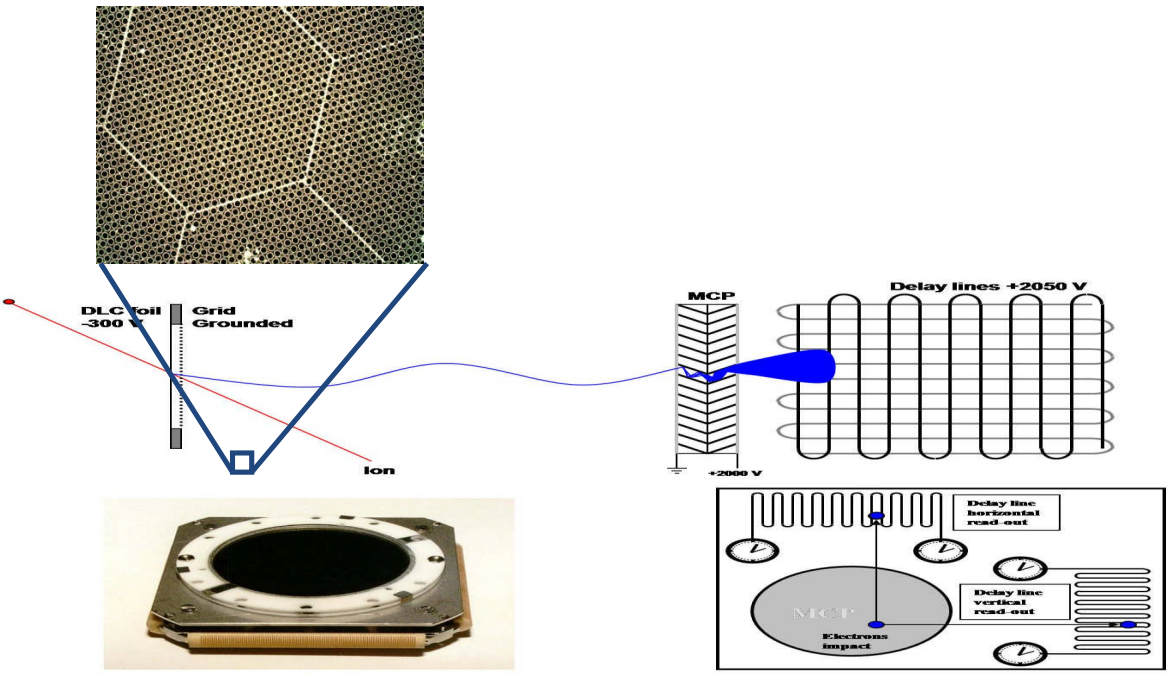

Fig. 3.24. *2D position sensitive MCP detector mounted on the delay-line structure and a scheme of the signal read-out. At the top a microscope picture of the pore structure is shown. The system was delivered by Röndeck, Frankfurt, Germany.*

The 2D detector is mounted at a distance of 80 mm from the foil, which is enough to be outside the cone of detected ions (see fig. 3.21). This detector has a diameter of the active area of 42 mm, it consists of two MCP´s of 1 mm thickness with a pore size of 25μm and a pore angle of 8º. The MCP´s are mounted in a chevron configuration. The detector is the most efficient for electrons with energy around 300 eV [42].The efficiency is then around 70-80 %. This figure will rise to close to 100% when more than one electron hits the detector.

The cloud of electrons emerging from the backside of the second plate is slightly accelerated towards two interwoven flat coils of delay line mounted behind the MCP at a distance of ~5 mm. The two coils (delay lines, see fig.3.24) are wound in perpendicular (XY) directions. Actually, each of the two lines consists of two isolated, interwoven and identical coils at different bias voltages with respect to the backside of the channelplate. These biases are chosen such that the second (reference) coils intercept only a small fraction of the electron cloud, while the other (signal) coil receives the major part of the electrons. The reference coils are used to reduce the electronic noise, as explained later. The pitch of one wire loop in each of the four coils is 1mm. The electron cloud emerging from the plates is accelerated in such a way that a number of wires of each coil are receiving a fraction of the charge. In each coil the charge is propagating towards both ends of the coil. By measuring the difference in arriving time of the signals at the ends of the coils, the position of impact of the cloud is determined. This can be done with a resolution of 0.15 x 0.15 mm, which is a much smaller value than the pitch of the coils. This better value can be obtained due to the division of charge over several coil windings (averaging effect). The total delay per coil is 35 ns. The difference in arrival time of the pulses at both ends of the coils must be determined with a precision of better than 100 ps for a coil length of 50 mm, to obtain a resolution of 0.15x0.15 mm.

The 1D position sensitive detector, mounted in the focal plane at a distance of 725 mm from the magnet and at an average distance of 1528 mm from the foil. The size of the sensitive area of this detector is 100mm long (position sensitive direction) x 15 mm high. The working principle of this detector is similar to the first one, but here the ion position is registered in a horizontal plane only. The position of the ion on this detector corresponds to the magnetic rigidity. The signal from this detector is also used as a stop signal for the ToF measurements. With a total delay of the line of

100 ns, the position resolution is ~0.2 mm. The detection efficiency for ions depends slightly on the mass and charge of the ion, and is around 50-70%. A photo of this detector is shown in fig. 3.25.

As an option a foil may be placed in the focal plane and the electrons emerging from this foil may be focussed on the detector. With this option the efficiency of the detection of ions may be increased to close to 100%, because more than one electron per ion is generated. The expected count rate needed for this detector is in the order of a few kilo counts/s.

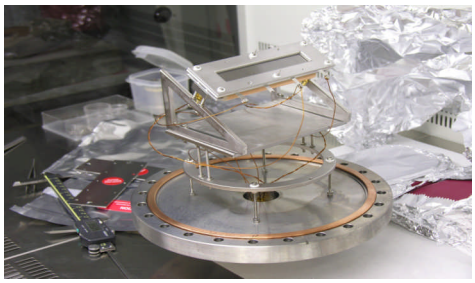

Fig. 3.25. *Photo of the focal plane MCP detector.*

3.11. Count rate considerations

When the magnetic spectrograph is placed at a forward detection angle, all ions scattered or recoiled from the sample within the detection cone are counted by the first detector system. Only a very small fraction of these ions are within the chosen window of the magnetic rigidity *mv/q*. A fraction of this fraction will acquire the correct charge state after passing the foil, coinciding with the magnetic rigidity to which the spectrograph is tuned. This gives rise to a high count rate ratio of events in the first and second detector. The situation may be even worse in case only a mono-layer of a light element is to be measured on top of a heavier matrix.

To estimate the count rate ratio to be expected we calculate the number of ions emerging from a Si sample covered with a mono-layer of oxygen, bombarded with 4 MeV He ions. We assume that the cross sections for scattering and recoiling are all given by the Rutherford formula. Using the program SIMNRA [44] based on the formula [2.20] discussed in Chapter 1, we arrive at the following number of counts for a number of He^{2+} ions corresponding to 1μC:

He ions scattered from Si: 2.09812E6

Recoiled Si ions: 2.09794E6

Recoiled O ions: 174

If we estimate that a fraction of 30% of the O ions have the correct charge state after passing through the foil, the expected number of detectable recoil O ions is: 52

Allowing a total count rate in the first detector of $2x10^6$ counts/s, the estimated count rate of detected O ions in the second detector is: 25

The conclusion is that the discrimination of unwanted events in the data manipulation system should be quite rigorous. This point is discussed in the next section.

The situation may be improved by placing a “weak” mini-Wienfilter in the “beam” of ions entering the spectrograph, close to the sample. A (retractable) Wienfilter could be constructed in the future with a length of 15 cm, a tuneable electric field of up to 1.5 MV/m and a constant magnet field of ~1000 Gauss produced by permanent magnets. Such a Wienfilter could be used to remove ions with low velocities (25% of the pass velocity) from the “beam” of detected ions, thereby reducing by at least an order of magnitude the count rate in the first detector.

3.12. Electronic system and data processing

As mentioned in Section 3.9.7, the electron cloud emerging from the backside of the MCP is attracted to a coil (or a set of two perpendicular coils in the case of the 2D position sensitive detector). Each coil actually consists of two interwoven coils, the signal coil and the reference coil, each with a pitch of 1 mm. A large fraction of the charge of the electron cloud is intercepted by the signal coil and only a small fraction by the reference coil. The ends of the reference coil and the signal coil are connected with twisted cables to the vacuum feedthroughs. At the outside of the feedthroughs the cables are connected to high-voltage capacitors, and after this the cable ends are united through the primary coil of a miniature transformer. Since the coils are identical, they will have largely the same cross talk with the signal on the backside of the MCP and also the same pick-up of electro-magnetic noise. The noise and pickup is eliminated for the major part in this way, because the signals on the lines are effectively subtracted. A clean signal is delivered to the secondary winding of the transformer. The two (or four) signals from the ends of the coils, as well as the signal from the backside of the MCP are then sent into an amplifier with a bandwidth of 2 GHz, to obtain signals with a rise time of few ns. As indicated in fig. 3.26, the 5 signals of the 2D detector and the 3 signals of the 1D detector are introduced into an 8-fold amplifier/constant fraction discriminator (Röntdeck). The NIM pulses from this unit are then sent into a 16- fold Time-to-Digital converter (TDC) (CAEN) [45] placed in a VME crate. Two inputs are used for each pulse to increase the time resolution. In this mode of operation the best time resolution achievable with this TDC is 40 ps. In practice we obtain a resolution of 75 ps for "synthetic" pulses from a pulse generator. This is still better than required to obtain the specified resolution. The digital output of the TDC is stored in a file of a PC used for data acquisition. The events in this file are labelled with the time and the channel number of the TDC.

The data manipulation process starts when a count at the backside of the focal-plane MCP appears. First it is tested if this event is accompanied by events on the channels corresponding to the coil ends of this detector. It is tested whether the sum of the delays of the coil signals with respect to the prompt pulse of the back side of the MCP is equal to the total delay of the coil ~100 ns. If this sum check fails, the event is rejected. Otherwise, these events are processed to determine the x position of the impact on this detector. This value determines the magnetic rigidity mv/q of the detected ion. The spectrograph is set for detection of a certain ion species, say O^{2+}. Assuming that the event is indeed due to O^{2+}, q/m is known, so then also v is known. From v and the known average distance between the foil and the second detector the flight time T is estimated. Then the program searches events preceding the event in the second detector by a time $T \pm \Delta T$ ($\Delta T \approx 20$ ns). T is on the order of 1 μs. If one (or more) quintuplets of events are found within this time domain, the sum check of the time delays is executed as with the second detector. In case this test is passed, the XY position of this event is determined. As mentioned in Section 3.9.5, part of the events corresponding to ill-focused high-energy electrons may be removed in this test. From this position and the x position on the second detector a more precise value of the magnetic rigidity (and thus for v) is determined from the Taylor expansion discussed in Section 3.6. Similarly, the precise value of the length of the trajectory is determined. From this information v is determined from the measured ToF, being the time difference between the matching events corresponding to the signals of the backside of both detectors. This value is compared to the value determined from mv/q. If there is a precise fit (within a time of 200 ps) the event is accepted, otherwise the event is rejected. An event will be rejected if the assumption made about the mass and charge of the detected ion is wrong. Note that this correspondence of the velocities determined by ToF and from the measured mv/q is not affected by the energy straggling in the foil. This implies that the rejection criterion is quite sharp, as needed to discriminate against the large amount of unwanted events (see Section 3.9.7). The determination of v from the flight time is probably more precise than from the determination from mv/q, via the position on the second detector Rejected events could be created by an ion with

the same value of *mv/q* but a different value of *v*. In this example it could be a C ion with a lower energy.

After this step in data manipulation the XY position on the foil and the velocity *v* is known for each event. To obtain a depth profile the data of accepted events is further manipulated to take into account the variation of the kinematic factor *K* and the path length inside the sample with the emission angle of the ion from the sample. The tabulated values for stopping forces S_1 (ingoing path) and S_2 (outgoing path) for the sample material are then used to relate the event with a certain depth in the sample. Also a 2D map of the measured intensity corresponding to a certain depth range in the detector can be created. In case the sample is mono-crystalline, a blocking pattern would be visible in such a map.

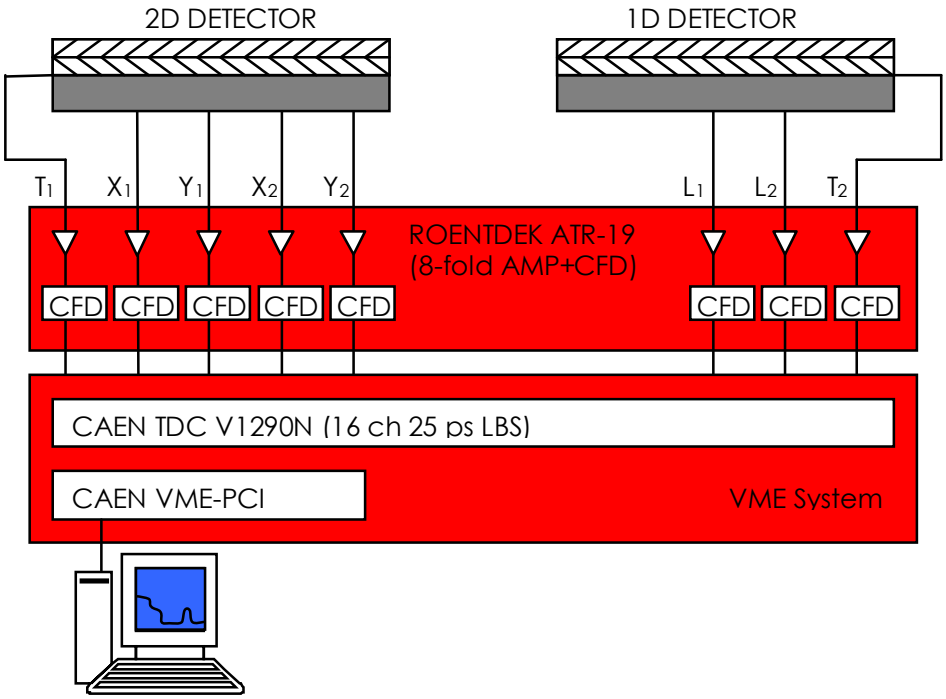

Fig. 3.26. *Schematic diagram of the fast electronic system used for collecting data from the two MCP detectors of the spectrograph.*

3.13. Overview of the complete magnetic spectrograph set-up

The complete system is shown in the fig. 3.27. The system consists of a central vacuum chamber, with the spectrograph attached to one of the side flanges of this chamber. The central chamber is mounted on a vertical axis, so that it can be rotated together with the spectrograph. For this reason the support of the spectrograph is mounted on a circular rail. The vertical axis is adjusted so that the beam intersects this axis (tolerance of less than 0.5 mm). The central chamber is provided with 5 small side flanges provided with valves. The beamline can be connected to any of those 5 flanges, so that the spectrograph can be at angles of: 0º, 20º, 45º, 70º and 135º with respect to the beam direction. Those angles were chosen for optimum conditions for depth profiling with RBS or ERD with high cross sections (see chapter 2). The 0º option allows special experiments to study ion-solid interactions. The beamline connects the spectrograph to the 5 MV tandem accelerator of the CMAM. The tank of the Tandem accelerator is visible in fig. 3.28.

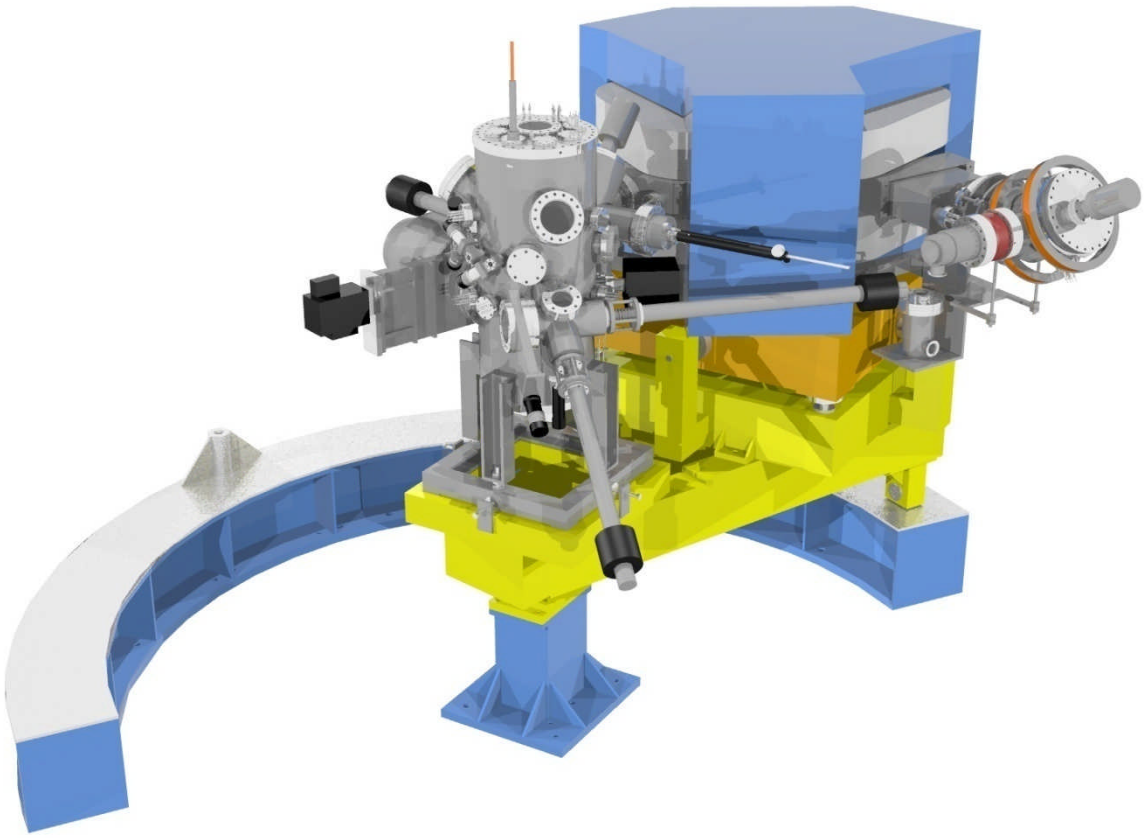

Fig. 3.27. *General view of the magnetic spectrograph. On the left of the magnet the main chamber can be seen, with the sample introduction system in the foreground. The sample is inserted on the 5-axes goniometer (see Section 3.8), that is mounted on the top flange. The foil and first detector are in a small chamber between the main chamber and the magnet (only partly visible). On the right of the magnet the chamber containing the focal plane detector ican be seen. The beam can enter into the main chamber (rotating with the magnet) through one of the five entrance ports. At the left the sample-introduction chamber can be seen, to which the "vacuum suitcase" can be mounted.*

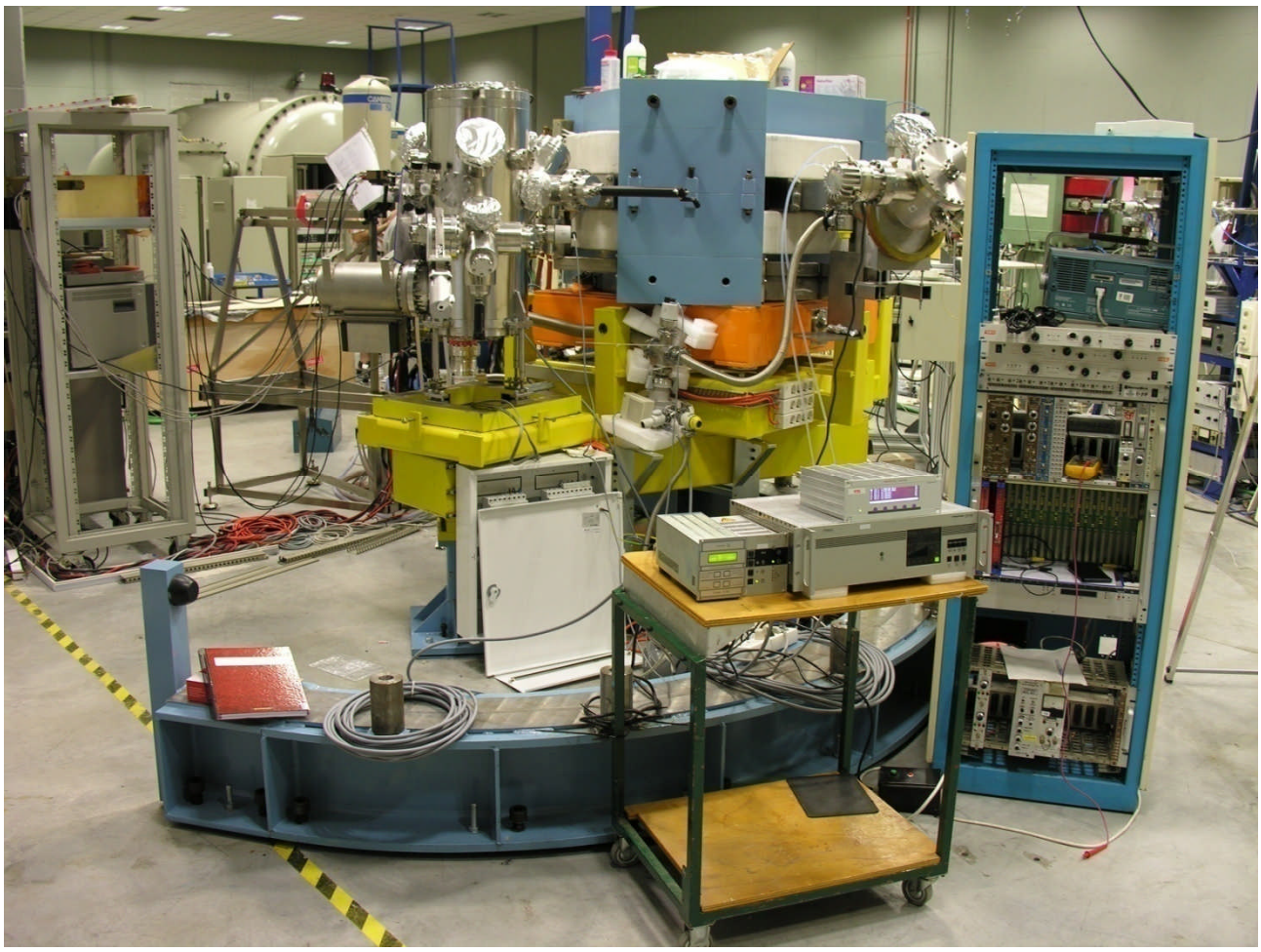

Fig.3.28. *View of the magnetic spectrograph line, with the 5MV CMAM tandem accelerator in the background. At the time of writing the spectrograph was in the testing phase.*

The chamber for the focal plane detector is connected to the magnet chamber with an edge-welded bellow allowing adjustment of the detector position. The whole system, including the chambers between the magnet poles and the chambers for the detectors is pumped to ultra-high vacuum (UHV) in the 10^{-10} mbar range (after baking to 180 ºC). The UHV is needed to work with samples with a clean and well defined surface. The vacuum is obtained using two turbo-molecular (TM) pumps in parallel, one mounted on the central chamber, and the other on the chamber of the focal plane detector. The pre-vacuum of these pumps is in the 10^{-6} mbar range. This vacuum is obtained by one common small TM pump with an oil-free scroll pump as the final pre-vacuum pump. In addition the system is pumped by two titanium sublimation pumps and an ionization pump. For the baking internal halogen bulbs will be used, in addition to external heating cords.

The precision 5 axes goniometer (see fig. 3.15) is mounted on the top flange and can be adjusted for alignment proposes. The goniometer is aligned so that its vertical axis coincides with the system axis, with the intersection point of the three rotation axes of the goniometer at beam height. The system is not equipped with any sample preparation system. Instead, samples can be introduced from a “vacuum suitcase” (see fig. 3.27). This is a small vacuum chamber, provided with a valve and pumped to UHV by a Zirconium absorption pump. Up to three samples prepared in external UHV systems can be loaded in this small chamber. The chamber is then attached to the load-lock chamber of the spectrograph system. After pumping the load-lock chamber and opening the valves the sample can be moved with a combination of two transfer rods and mounted onto the head of the goniometer. Optionally, up to three samples can be stored in special holders in the spectrograph system. The transfer rods are coupled by permanent magnets to an external magnet.

With this last magnet the rod can be moved manually. The samples are 3” wafers, or samples with this shape. During transport they are clamped between magnetically operated tweezers, mounted at the end of the transfer rods. Samples can also be introduced from the ambient by the use of the load-lock system.
In figure 3.29 the last part of the beamline before the spectrograph can be seen. Also this vacuum system is pumped by a TM pump, backed up by the same pre-vacuum system as used for the main chamber. The beamline contains a retractable Faraday cup mounted behind two pairs of adjustable slits (horizontal and vertical).

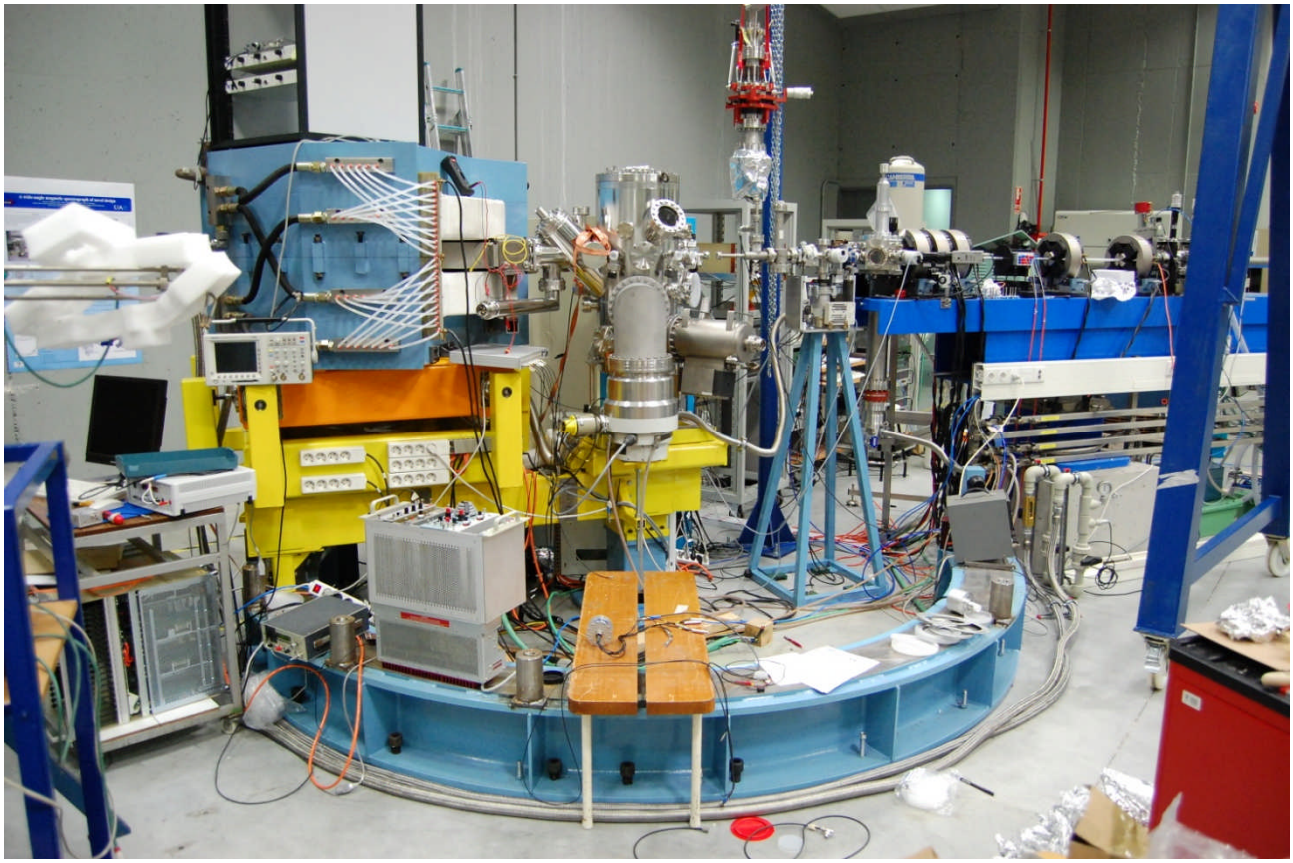

Fig. 3.29. *Another view of the magnetic spectrograph line. On the right part of the beam line is visible, connecting the system to the beam line for scanning proton microscopy.*

3.14 First test results

At the time of writing of this chapter, the spectrograph was only partially tested. The spectrograph was aligned so that its rotation axis intersects the beam position within 0.5 mm. It was tested that the maximum field of 1 Tesla is achieved with a current in the coils of close to 100 Amp´s. The last part of the beamline was aligned, and a beam can be guided into the chamber. The vacuum system was tested. The vacuum achieved in the whole system using the two turbo-molecular pumps was 2.10^{-9} mbar, so that it is to be expected that the design value of 2.10^{-10} mbar will be met after baking, and maybe after installing the sublimation and ionization pumps. The electronics and the data acquisition programs were developed by Dr. A Guirao and Dr. V. Joco. The time resolution of the TDC was measured to be 75 ps at a count rate of 3.10^{6} counts per second, using pulses from a pulse generator. These characteristics are more than sufficient to meet the design properties of the spectrograph. Finally the focussing properties of the spectrograph were tested in the 0^{o} position, by guiding a 2 MeV He beam through a 1mm diameter diaphragm at the sample position directly into the spectrograph. A plate with photo-luminescent layer was placed at

the position of the focal plane detector. In fig. 3.30[c] a number of small spots can be seen on this plate. Each spot corresponds to a different discrete value of the magnetic field. The spots are estimated to be of the same size as, or smaller than, the size of the diaphragm, in accordance with the calculations.

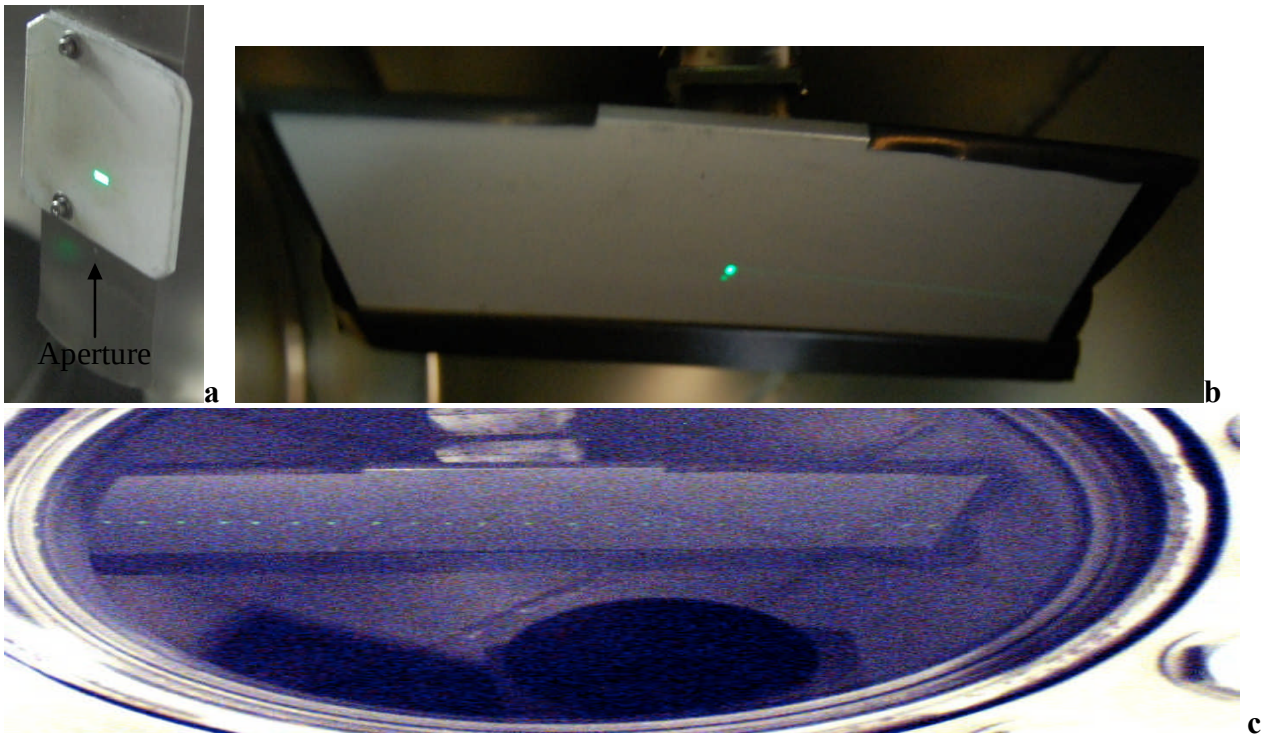

Fig.3.30. a *The spot of the He beam on the photo-luminescent layer placed at the sample position on the XY table of the goniometer. The rectangular shape is the result of collimation by the slits in the last part of the beamline. Later the plate was lifted so that the beam passes through the indicated 1mm diameter aperture.* ***b*** *The plate covered with a photo-luminescent layer placed in the focal plane. The beamspot is focused with a magnification near to 1. The spot is somewhat blurred, because the camera was hand-held. The faint line to the right is due to He ions with a lower energy. They are possibly scattered at the rims of apertures.* ***c*** *Photograph taken with repeated exposure of the plate installed at the focal plane while it was hit by the beam, with the magnet field varied in discrete steps around its central value.*

3.15. References

1. P. Neumaier et al., Nucl. Instr. and Meth. B 183 (2001) 48.
2. J. C. Vermeulen, J. van der Plicht, A. G. Drentje, L. W. Put and J. van Driel, Nucl. Instr. And Meth. 18 (1981)93.
3. S. Shimoda, T. Kobayashi, Nucl. Instr. And Meth. B 219 (2004) 573.
4. D. Bazin et al., Nucl. Instr. and Meth. B 204 (2003) 629.
5. A. M. Stefanini et al., Nucl. Phys. A 701 (2002) 217c.
6. A. Latina et al., Nucl. Phys. A 734 (2004) E1.
7. A. Cunsolo et al., Nucl. Instr. and Meth. A 484 (2002) 56.
8. H. Savajols, Nucl. Phys. A 746 (2004) 260c.
9. H. Savajols, Nucl. Instr. and Meth. B 204 (2003) 146.
10. H.A. Enge, Nucl. Instr. and Methods 28 (1964) 126.

J. E. Spencer, H. A. Enge, Nucl. Instr. and Meth. 49 (1967) 181.
http://www.ansys.com/.
D.C. Carey, Optics of Charged-Particles Beams, Harwood, Chur, Switzerland, 1987.
H. Wollnik, Charged Particle Optics, Academic Press, Orlando, FL, 1987.
H. v. Helmhlotz, J. Reine Angew. Math. Crelle's J. 55 (1858) 25.
P.M. Morse, H. Feshbach, Meth. Theor. Phys. Part I and II, (1953).
P.L. Walstorm, Nucl. Instr. and Meth. A 519 (1-2) (2004) 216.
M. Venturini, A.J. Dragt, Nuc. Instr. and Meth. A 427 (1999) 387.
S. Kowalsky, H.A. Enge, RAYTRACE. Technical Report, MIT, Cambridge, MA, 1985.
11. S.B. Kowalski and H.A. Enge, Nucl. Instr. and Methods in Physics Research A 258 (1987) 407.

Karl L. Brown, SLAC Report-75, 1982.
12. K.L. Brown, F. Rothacker, D.C. Carey, and Ch. Iselin, CERN Raport No. CERN 80-04, 1980, http://weblib.cern.ch/.
13. K.L. Brown, Ch. Iselin, D.C. Carey: Decay Turtle, CERN 74-2 (1974).
14. D.C. Carey, K.L. Brown, and Ch. Iselin, SLAC Report No. SLAC-R-246, 1982.
15. M. Berz, Los Alamos Report No. LA-11857-C, 1990, p. 137.
16. R. Degenhardt, M. Berz, Nucl. Instr. and Meth. A 427 (1999) 151.
17. K. Makino, M. Berz, Nucl. Instr. and Meth. A 558 (2005) 346.
18. http://www.bt.pa.msu.edu/
19. Ellyt Energy, Madrid Office, http://www.elytt.com/.
20. A. G. Drentje, R. J. de Meijer, H. A. Enge and S. B. Kowalski, Nucl. Instr. and Meth. 133 (1976) 209.
21. H.A. Enge, Nucl. Instr. and Meth. 187 (1981) 1.
22. V. Kh. Liechtenstein, T. M. Ivkova, E. D. Olshanski, R. Repnow, J. Levin, R. Hellborg, P. Persson and T. Schenkel, Nucl. Instr. and Meth. A 480 (2002) 185.
23. V. Kh. Liechtenstein, T. M. Ivkova, E. D. Olshanski, R. Golser, W. Kutschera, P. Steier, C. Vockenhuber, R. Repnow, R. von Hahn, M. Friedrich and U. Kreissig, Nucl. Instr. and Meth. A 521 (2004) 197.
24. V.Kh. Liechtenstein, T.M. Ivkova, E.D. Olshanski, R. Repnow, P. Steier, W. Kutschera, A. Wallner and R. von Hahn, Nucl. Instr. and Meth. A 561 (2006) 120.
25. G. Gloeckler and K. C. Hsieh, Nucl. Instr. and Meth. 165 (1979) 537.
26. E. C. Pollacco, J. C. Jacmart, Y. Blumenfeld, Ph. Chomaz, N. Frascaria, J. P. Garron and J. C. Roynette, Nucl. Instr. and Meth. 225 (1984) 51.
27. Marcus H. Mendenhall and Robert A. Weller, , Nucl. Instr. and Meth. B 40 (1989) 1239.
28. Ch. Klein, J. Trötscher and H. Wollnik, Nucl. Instr. and Meth. A 335 (1993) 146.
29. J. K. Kim, Y. S. Kim, G. D. Kim, H. W. Choi, H. J. Woo, S. Y. Cho and C. N. Whang, , Nucl. Instr. and Meth. B 140 (1998) 380.
30. M. Döbeli, R. M. Ender, V. Liechtenstein and D. Vetterli, Nucl. Instr. and Meth. B 142 (1998) 417.
31. A. Razpet, P. Pelicon, Z. Rupnik and M. Budnar, Nucl. Instr. and Meth. B 201 (2003) 535.
32. J.O. Stoner Jr., J. Appl. Phys. 40 (1969) 707.
33. http://www.precisioneforming.com/
34. G. Both, E.P. Kanter, Z. Vager, B.J. Zabransky, D. Zajfman, Rev. Sci. Instr. 58 (1987) 424.
35. V.A. Khodyrev, V.S. Kulikauskas, C. Yang, Nucl. Instr. and Meth. B 195 (2002) 259.
36. J.F. Ziegler, J.P. Biersack, U. Littmark, The Stopping and Ranges of Ions in Solids, Pergamon Press, 1985.
37. http://www.srim.org/
38. Z. Vidović, A. Billebaud, M. Fallavier, R. Kirsch, J.-C. Poizat, and J. Remillieux, Phys. Rev. A 56, (1997) 4807.

39. N. Pauly, A. Dubus, M. Rösler, H. Rothard, A. Clouvas and C. Potiriadis, Nucl. Instr. and Meth. B 230 (2005) 460.
40. D. Meeker, http://femm.berlios.de/.
41. O. Jagutzki, V. Mergel, K. Ullmann-Pfleger, L. Spielberger, U. Spillmann, R. Dörner and H. Schmidt-Böcking, Nucl. Instr. and Meth. A 477 (2002) 244.
42. Manual for DLD40, Roentdek Handels GmbH, http://www.roentdek.de.
43. G. D. Kim, W. Hong, J. K. Kim, H. W. Choi and H. J. Woo. Korean Phys. Soc. 42, 305, (2003) .
44. http://www.rzg.mpg.de/
45. http://www.caen.it/

Chapter 4. THE COMPUTER SIMULATION PROGRAM TRIC

4.1. Introduction

As discussed in chapter 2, energy spectra of ions with energies in the keV- MeV range scattered or recoiled from a (crystalline) sample can, in principle, be simulated by calculating many trajectories of ions entering the solid and ending in the detector. The problem is that only a small fraction of the ions makes it to the detector because of the small cross sections for scattering and recoiling. For this reason such "direct" simulations are impossible with the exception of simulation of low-energy ion scattering from a few layers only, using programs like MARLOWE [1] or SARIC [2]. Also the program MATCH [3] may be used for this purpose. For the direct simulation of spectra involving many layers and energies of light ions in the MeV range, the number of trajectories to be followed to obtain sufficient statistics in a small-angle detector placed at a backward angle would be on the order of 10^{12} and three to four orders of magnitude less for ions in the keV energy range. For this reason the concept of the close-encounter probability (CEP) was introduced and applied in a number of simulation programs like LAROSE [4], FLUX [5], XTRIM [6], UPIC [7], FullSim [8]. With these programs channelling spectra with reasonable statistics can be obtained by calculating 10^4-10^5 ingoing ion trajectories. Whenever the ion trajectory comes close to the equilibrium position of an atom, the CEP is calculated as the overlap integral of the ion trajectory and the distribution of thermal displacements of the position of the considered atom. The yield in the detector is supposed to be proportional to the CEP and is optionally weighed with the cross section for scattering from the direction of the trajectory to the direction of the detector. A requirement for this approximation is that the typical impact parameter for the large-angle scattering in the direction of the detector is much smaller than the thermal vibration amplitude, as is the case for scattering of medium- or high-energy light ions. In this approach the single scattering model is applied to the outgoing part of the trajectory and also channelling/blocking effects on this part of the trajectory are ignored. With some of the mentioned programs [5,7] also blocking spectra can be simulated using the same concepts in time-reversed mode.

Medium-energy ($\approx$ 100 keV) scattering of H or He ions is often used to probe the composition and structure of a number (< 10) of atom layers near the surface of crystalline samples. Commonly the measuring geometry is chosen such that the incoming beam and the direction of the detector are both in axial or planar directions in the crystal, so that programs like FLUX cannot be used for the simulation. For the simulation of this type of data the program VEGAS [9,10] was developed. For each type of atom at a given depth the CEP, summed over all incoming trajectories, is calculated. The same is done in time-reversed mode for the outgoing trajectories. The scattering yield from the atom is supposed to be proportional to the product of both CEP´s multiplied with the cross section for scattering over the angle between in- and out-going trajectories. In a separate

program this output is used to construct the energy spectrum, taking into account the energy losses on the ingoing and outgoing parts of the trajectories. Also this approach bears heavily on the applicability of the single-scattering model. In fact, the incoming and outgoing ion fluxes are "matched" at the position of the atom at which the scattering takes place. In this matching the misfit in energy and scattering angle is ignored. Although this kind of simulations reproduces well experimental scattering patterns for near-surface layers, the level of inaccuracies due to multiple scattering remains uncertain. For the simulation of blocking patterns of recoiled ions as to be measured with the magnetic spectrograph this type of programs will not be suitable, because multiple scattering cannot be ignored in this case. This was the reason that at the CMAM a new type of simulation program was developed, in which multiple (and also plural) scattering is taken into account. The program (TRIC) was developed by dr. V.A. Khodyrev and it was tested in a number of applications by a small team of physicists of the CMAM. In this chapter the principle of the program is described and a number of test results are discussed.

4.2. The program TRIC

The program TRIC (Trajectories of Ions in Crystals) combines the exact treatment of the classical binary collision model with a speed of computation that is higher compared to direct simulation by a factor of 10^4 -10^6 depending on the case. Trajectories of scattered and recoiled ions propagating in the solid are calculated, starting from a randomly chosen point of impingement located at some distance above the surface. The calculation is ended when the ion energy has dropped below a pre-defined value, or when the ion leaves the sample. It can be applied for simulation of energy spectra measured in LEIS, MEIS and HEIS and also for ERD spectra. Application of this program allows interpretation of scattering or recoil data for basic studies or for structure analysis.

In the program ion trajectories are calculated relatively fast in classical approximation as a sequence of elastic binary collisions, treated in the asymptotic approximation, of the ion with atoms at thermally displaced positions (see, for example, Ref. [1]). A properly screened Coulomb potential is used to describe the ion-atom interaction. The screening function is parameterized as a sum of four exponentials, so that any type of screening function $\varphi(r/a)$ with adapted screening radius a can be selected, for instance the Molière function [11], the ZBL function,[12]or screening functions calculated with the Hartree-Fock method [13]. In numerous works it has been shown that this description is sufficient for the mentioned range of ion energies. The scattering and time integrals (see section 2.5) are calculated to establish as a function of the impact parameter the angle of scattering or recoiling and the intersection point of the asymptotes of the trajectories before and after the collision. The interaction sphere is restricted to $r < r_0$ with the interaction radius r_0 taken as half the distance between nearest neighbours in the crystal lattice. The ion trajectories start at a plane at some distance above the surface to enable that the interaction with the top atomic layer is calculated without a restriction in the interaction radius.

Multiple scattering on electrons is taken into account as a (very small) fluctuation of the scattering angle (see section 2.4.4). The nuclear energy loss per collision is determined by the kinematic factor. The impact-parameter dependent inelastic electronic energy loss per collision is calculated according to simple models. For low energies in the keV range the Oen-Robinson model [14] is used while, at medium at high energies, the energy loss is assumed to be proportional to the local electron density as sampled along the trajectory. This density consists of a uniform distribution of valence electrons (which number is defined by the tabulated Fermi energies [Ziegler], and the density of atomic core electrons. The latter, in turn, is defined by the interaction potential by solving the Poisson equation with the possibility to optimize the screening radius. By varying the value of the screening radius, the non-local character of the energy loss can be reproduced to certain extend. Finally, the electronic energy loss averaged over the impact parameter is normalized to the values tabulated by Ziegler et al[zz]. All characteristics of the binary collisions

depending on energy and impact parameter are tabulated at the preliminary stage of simulation and are evaluated using a spline fit of the tabulated data. For technical reasons the scattering angle is calculated using the impulse approximation, if this angle is smaller than approximately 1 degree. It is worthwhile to notice that it would be easy to implement more features into the program, like charge exchange or energy loss straggling per collision.

A special effort was made to select in an efficient way the next collision partner, since this is the most time-consuming process in the program. The next collision partner is the closest atom in forward direction, for which the impact parameter $b < r_0$. It is important to restrict the number of possible candidates for the next collision. This is done by presenting the crystal structure as a set of Wigner-Seitz cells. Then the possible next collision partner is in an adjacent cell in forward direction. At the lower level, TRIC operates with the crystal structure described in this way. With this approach, in principle, any structure can be described.

The higher speed is achieved by importance sampling [xx,yy, see the two refs I give under refs.]. This concept has not been used before in this type of simulation. For atoms, that are close to the ion trajectory, a small volume is defined such that scattering from atoms placed in this volume leads to trajectories within a wide cone with the detector position in the centre. The method is illustrated in fig. 4.1. By sampling several atom positions from the (assumed Gaussian) distribution of atom displacements in this volume, a shower of "secondary" ion trajectories is generated. Also the "primary" trajectory is continued by sampling the atom displacement from the rest of the distribution of displacements. Secondary trajectories have a much bigger chance for ending in the detector than primary trajectories. Further showers can be generated along primary trajectories, but not along secondary ones.

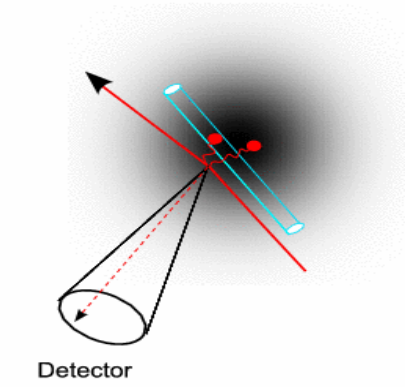

Fig. 4.1. *Illustration of the process of shower formation. The thermal distribution of atom displacements is depicted as a cloud with varying grey scale. The primary ion trajectory is shown in red. When the atom position is within the volume indicated in blue, scattering into the cone around the detector would follow. The opening angle of the cone is much larger than that of the detector.*

The preferred sampling is compensated by assigning weighing factors to each trajectory, with W_0 as initial value. When the i^{th} shower is generated, the weighing factor is updated to $W_i = (1-P_i)W_{i-1}$, where P_i is the probability for the atom to be displaced in the "hot" region from where scattering into the cone follows. A weight $w_i = W_{i-1}P_i/n_i$ is assigned to each of the n_i secondary trajectories in the shower. The important condition of conservation of ion flux is obviously fulfilled, $W_i + n_i w_i = W_{i-1}$. We choose $n_i = P_i W_{i-1}/ w_0$, so that $w_i = w_0$ is a constant. The fractional part of this number is taken into account by drawing one extra trajectory with a chance equal to the fractional part. It is crucial to have constant weights to suppress fluctuations in the accumulated spectra. With these choices it is also prevented that trajectories are calculated with a too small weighing factor, leading to inefficient use of computer time. Finally we choose $w_0 = P_{max}/n_0$, where P_{max} is the integral weight of the most intense shower and is the number of ions in the most intense shower, defined in the input of the program. Usually a value for n_0 between 200 and 1000 is chosen. Application of

these special sampling methods leads to simulation of smooth spectra, consisting of many events with a small weight, contrary to a few events with a weight of unity. If we choose W_0=1, the expectation value of the total yield in the spectrum is the same as without shower generation and equal to the expectation value in the experiment. This point is illustrated in fig. 4.2. Instead of $w_0=P_{max}/n_0$ we choose finally w_0=1, multiplying thereby the intensity in the spectrum by a large and known factor n_0/P_{max}. Like in the experiment, the calculated spectrum is then a histogram with integer numbers of counts, which mimics to certain extend the experimental situation.

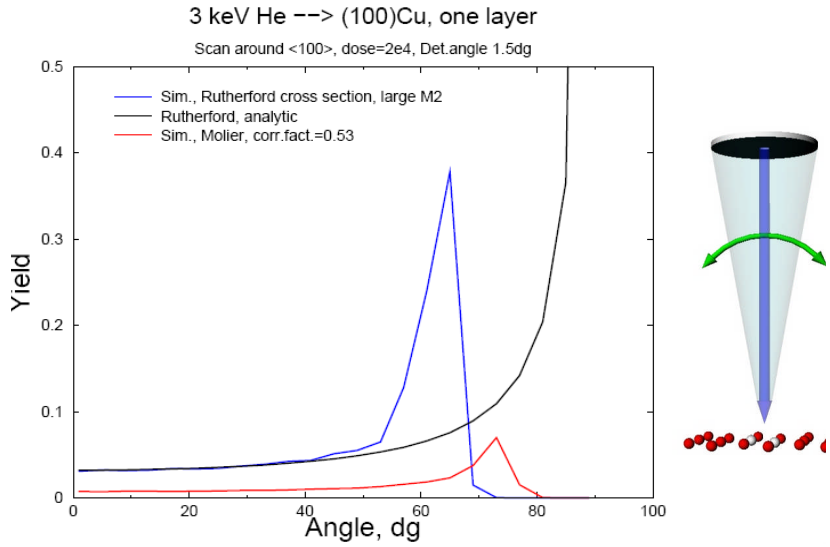

Fig. 4.2. *Simulation of scattering of 3 keV He ions from a single layer of Cu(100). The geometry is depicted in the diagram at the right. The opening angle of the detector is 1.5°. The blue line indicates on the absolute scale ($w_0 = P_{max}/n_0$) the simulation result for 2.10^4 incoming ions for the Coulomb potential for the ion-atom interaction. The simulated yield beyond an angle of 70° between the surface normal and the direction of the beam is zero because of blocking. The maximum at 62° is due to focusing. The black curve is calculated using the Rutherford formula and the same size of the detector as in the simulations. This curve coincides with the simulation result in the angular range where blocking or focusing effects are absent. The simulation result obtained with the Molière potential with a screening-radius reduction factor of 0.53 is indicated in red.*

When plural scattering is important, violent statistical fluctuations in the calculated spectra may occur as follows. It may happen that a primary trajectory is scattered in a direction close to the cone mantle. When later a shower is generated from this primary trajectory, the number of trajectories in this shower can be very large because the "hot" region can be large (forward scattering) and not necessarily far away from the equilibrium position of the atom. The resulting fluctuations are illustrated in fig. 4.3, top frame. To resolve this problem, we introduce a second, wider cone, concentric with the first cone. Now, upon the generation of a shower, two small, nested volumes are defined, one corresponding to scattering into the inner cone, and a second corresponding to scattering into the solid angle between the two cone mantles. In addition to the "normal" shower, a second shower consisting of one or a few trajectories is generated into the latter solid angle with the appropriate weighing factor. With this procedure of "stratified" sampling it is prevented that primary trajectories with a large weighing factor propagate close to the first cone. Instead, such trajectories, which are treated as primary trajectories in the rest of the simulation, have now a small weighing factor. With a proper choice of the sizes of the first and second cone widths, spectra with much smoother statistics are generated (see fig. 4.3, bottom frame). With the realized algorithm it would be easy to generalize this procedure for an arbitrary number of nested cones.

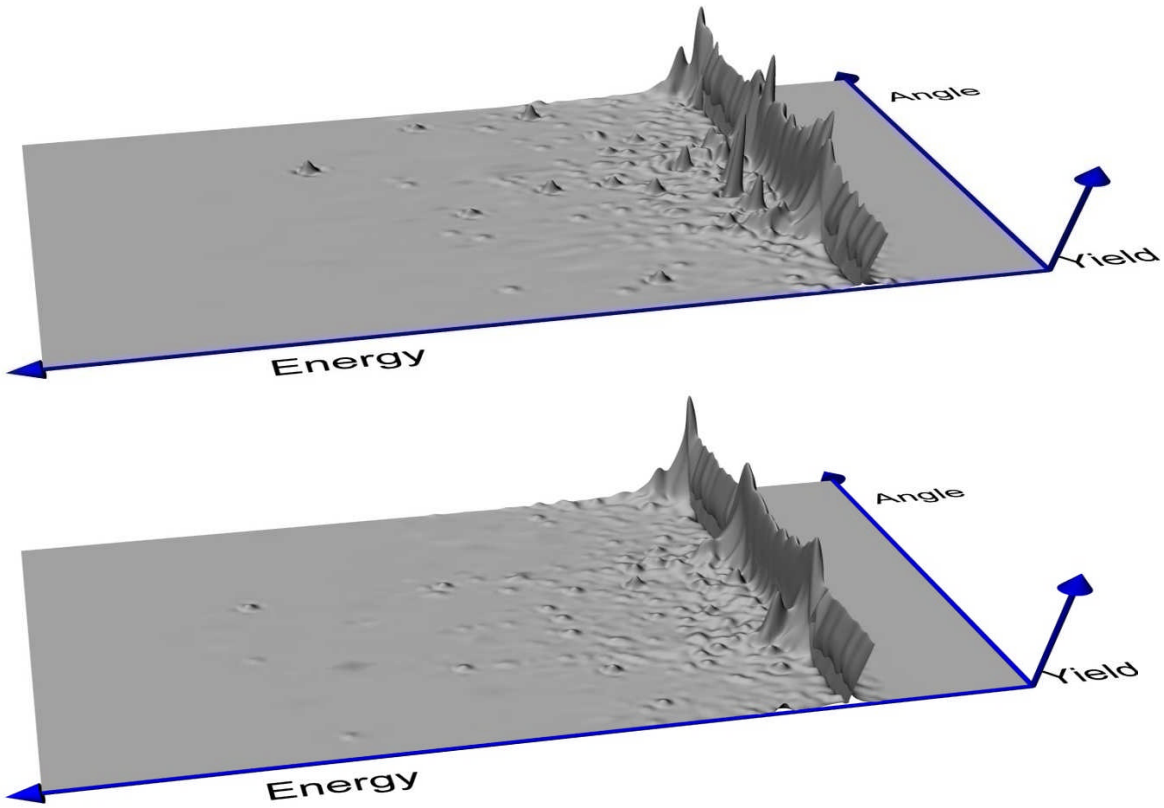

Fig. 4.3. *Example of the result of a simulation of an azimuth scan of 3 keV He^+ ions scattered from a Cu(100) crystal. The beam is in the (010) direction normal to the sample. The sample is rotated around this same direction and spectra are recorded, using a fixed detector at a scattering angle of 129^o, in steps of 2^o, from azimuth angles running from 15^o to + 110^o. Here 0^o and 90^o coincide with the (010) surface string directions .The simulated yield is plotted in a 3-D picture as a function of the energy and the azimuth angle. The simulation in the top frame was carried out with one cone for shower generation. The simulation in the bottom frame is with two nested cones. Both simulations were done with 10^5 initial ion trajectories. As can be seen the corrugation is much higher in the top frame than in the bottom frame.*

It is interesting to notice that the concepts of “importance” sampling and “stratified” sampling are also used in the familiar method used to improve the speed of numerical Monte-Carlo calculations of integrals. (xx,yy)

The developed program TRIC is written in FORTRAN code supplied with GUI where the shower generation is described in the recursive algorithm. It provides the possibility to solve a wide class of simulation problems, including scattering from crystals with a complex structure or with reconstructed or stepped surfaces. The unit cell used to describe the atom positions can be of large size to make this possible. Empty sites (vacancies) may be introduced to describe the surface structure.

Also amorphous structures can be introduced by rotating the sample randomly after each interaction. The model for the ion- atom interaction (potential, inelastic energy loss, multiple scattering on electrons) can be varied. As output, energy spectra of scattered or recoiled ions, optionally subdivided in the yield per layer, can be generated as a function of the measuring geometry. Also angular distributions of scattered or recoiled ions as measured within a certain energy window by a 2-D position sensitive detector can be simulated. With the applied method, in particular this type of simulation can be done in a time-efficient way. This last application would be very relevant for the simulation of blocking patterns as could be measured with the 2-D magnetic spectrograph detection system described in chapter 3.

At high energies a technical problem is encountered in the calculation of the “hot” regions, which become very small (in the plane transverse to the trajectory). As a result, also the probabilities P_i are very small ($\approx 10^{-10}$ for 100 keV protons in Si), so that the accuracy of numerical calculations could become a decisive factor. In the developed algorithm this problem is solved in the following way: when the diameter of the "hot" region turns out to less than some predefined value (conventionally, $0.01u_1$ with u_1 the mean amplitude of thermal vibrations), the procedure of generation of the showers is inverted. Instead of the atom displacements, the angle of scattering is uniformly sampled within the cone. The associated weighing factor is assumed to be constant over the transverse plane. The longitudinal component of the atom thermal displacement (within the narrow "hot" region) is independently sampled. It determines the point of crossing of the scattering asymptotes. Though here a small approximation is made, this approach is adequate for medium- and high-energy simulations.

In the program the option is available to also sample by importance the positions of impact of the ions on a crystalline sample. This makes sense because different initial positions result in a different contribution to the accumulated statistics. An example is the simulation of channelling where the backscattering yield is mainly from ions with a significant transverse energy, i.e. from positions near to strings of atoms. Thus, it seems reasonable to sample these positions more often. The optimum distribution for sampling is not known *a priory*. In the developed algorithm this problem is solved by starting the simulation with the uniform distribution of impact points. This distribution is subsequently deformed according to the accumulated information on the effectiveness of different initial coordinates. The final non-uniform distribution is taken as a constant plus the deformed distribution. To obtain the correct result, the trajectories are weighed inversely proportional to the sampling density. It was found that this procedure results in an increase of the speed of simulation of up to one order of magnitude in specific cases.

4.3. Examples of application

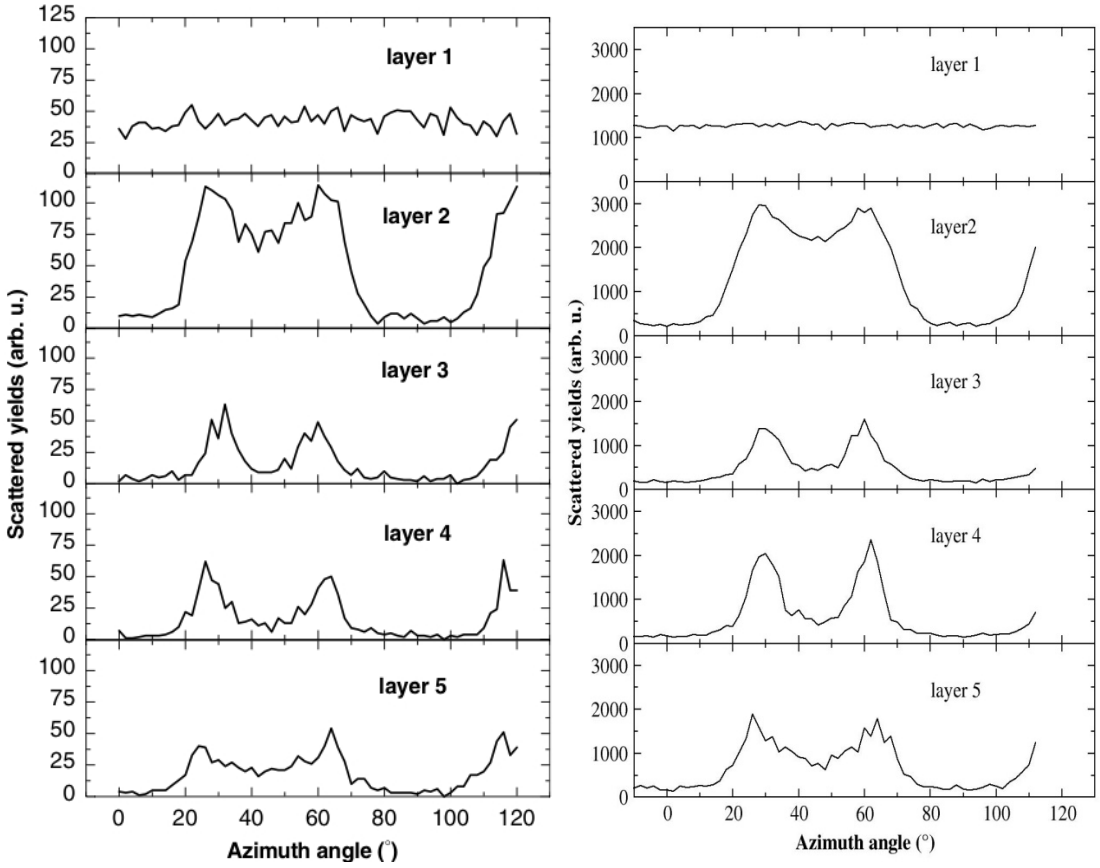

Fig. 4.4. *Simulation of an azimuth scan of 3 keV He ions scattered from a bulk-terminated Cu(100) crystal. The rotation was around the (100) surface normal, which was also the beam direction. The detection angle was 129°. On the horizontal scale 0° and 90° coincide with (110) surface string directions. The simulations were done with the program Marlowe (left) and with the program TRC (right). In both cases the Molière potential without a reduction of the screening radius was used. Notice the large difference in the accumulated statistics. Within the statistical uncertainties the results appear to be equal. The simulations with Marlowe were taken from a paper by the group of Bauer .*

As stated, the program TRIC can be used to simulate LEIS, MEIS and HEIS data. In this section we compare the output of TRIC with experimental data that were also simulated with one of the other simulation programs mentioned in the introduction.

A first comparison between the output of TRIC and MATCH concerns the simulation of an azimuth scan of 2 keV He ions scattered from a bulk-terminated Cu(100) crystal with the beam and rotation axis perpendicular to the sample and the detector at a scattering angle of 129°. The simulations with the program Marlowe were done by the group of Bauer [xx]. In the left frame of fig. 4.4, the simulated azimuth scan of the scattering yield from the first 5 layers of the sample is plotted separately for each layer. In the frame on the right the same scans as simulated with TRIC are shown. Both simulations were done with the Moliére potential. Within the statistical uncertainties (which are large for the MARLOWE simulations) the results appear to be equal, as is to be expected.

Next the output of the program TRIC is compared with the output of MATCH. Angular distributions of the scattering of 5 keV Ar^+ ions from a clean Ag(100) surface were measured for two geometries as shown in fig. 4.5. The experimental scans were obtained by integrating the scattering peak in the ToF spectra at each angle. The (non-reconstructed) structure of this surface and the vibration amplitudes of the surface and bulk atoms are well known. The ion-atom potential is well described by the Molière potential with a screening-radius reduction factor of 0.8. The data and the simulations with MATCH (calculated with these parameter values) are taken from the thesis of dr. Langelaar, Groningen University . In fig. 4.5 the simulation results obtained with MATCH and with TRIC are compared. A number of 10^4 ion trajectories were used in both simulations, not counting the secondary trajectories used in TRIC. The number of near-surface layers considered in both simulations was 6. The simulation with TRIC is slightly faster than with MATCH: the whole simulation of 45 points of the scan took 2h on a normal PC working at a frequency of 3 GHz. It is clear that the experimental data are reproduced within the uncertainties of the measurement, mainly consisting of small (few tenths of a degree) deviations from the ideal measuring geometry.

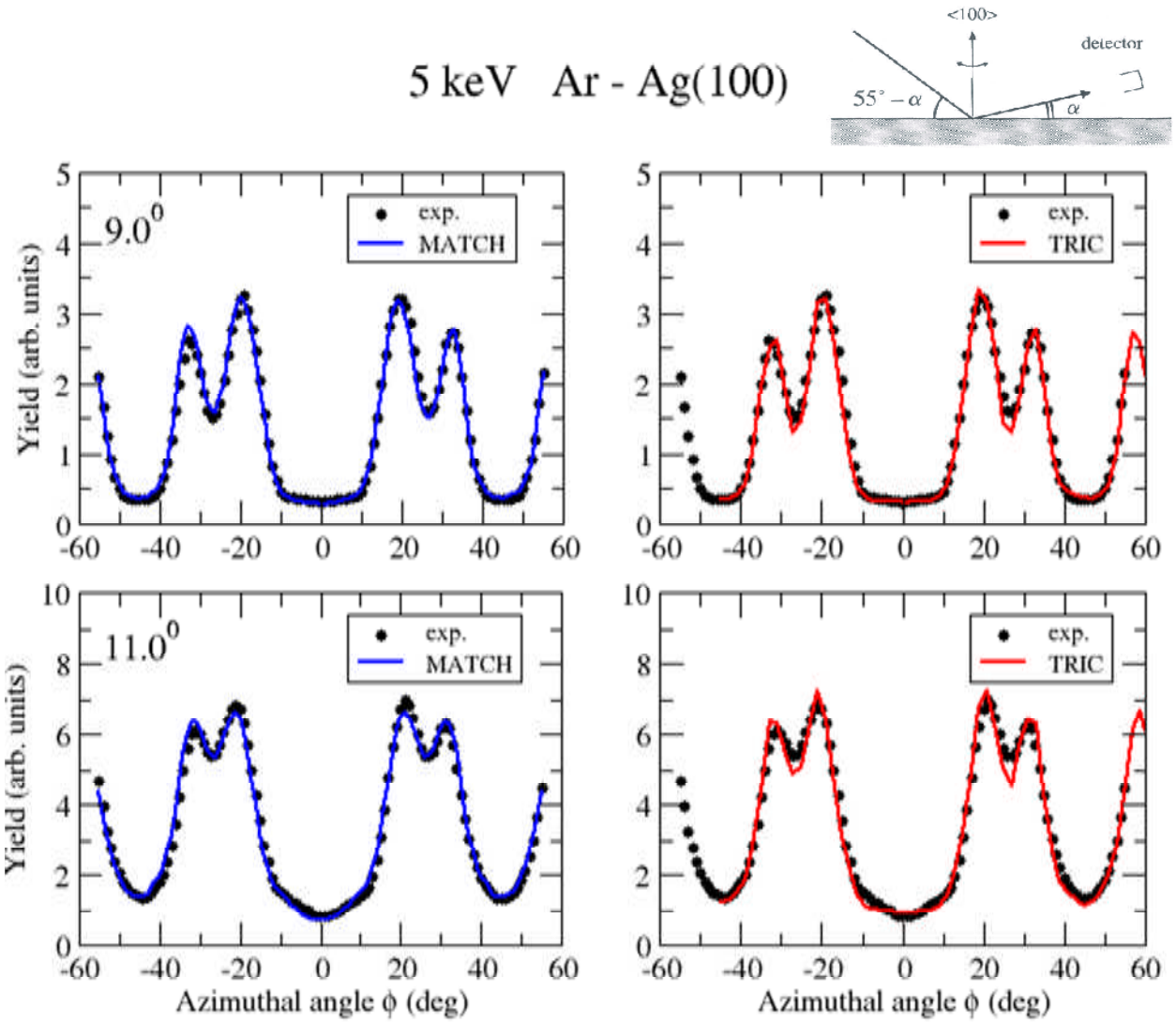

Fig. 4.6. *Comparison of experimental angular scans of the scattering of 5 keV Ar ions from a clean Ag(100) surface. The ToF data was measured by dr. M. Langelaar, University of Groningen [ref thesis Langelaar]. On the horizontal scale 0° coincides with the (110) surface string. The angle α of the measuring geometry, indicated in the insert, is slightly different for the top frames (α = 9.0°)*

as compared to the lower frames (α= 11º) revealing the strong dependence on the geometry. In the simulation with MATCH this geometry is slightly adjusted.

The small deviations between the output of MATCH and TRIC may be explained by a difference in the optimization of the measuring geometry.

Another example concerns the bombardment of a (c-2x2) bulk-terminated (100) Fe_4N surface with 4 keV Ar ions and the measurement of azimuthal scans of scattered Ar atoms and recoiled N and Fe atoms. In these scans the crystal was rotated around its (100) surface normal. The beam was at an angle of 12º with the surface; the scattering angle was 54º. A ToF spectrum, summed over all measured angles, is shown in fig. 4.6. At each angle of the scan the scattering or recoiling intensities were extracted from the spectra by fitting the respective peaks in the spectra with Gaussians.

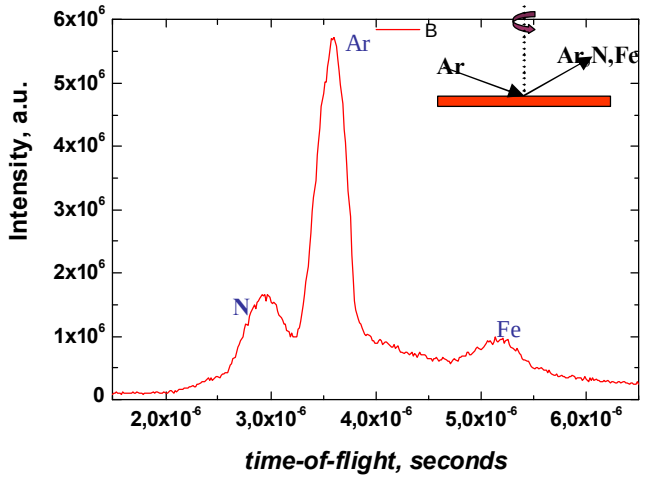

Fig. 4.6. *ToF spectrum, summed over all angles measured in an azimuth scan of 4 KeV Ar ions scattered from a (c2x2) (100) Fe_4N surface. The beam makes an angle of 12º with the surface; the scattering angle is 54º. In the spectrum the scattering peak and the peaks due to the recoiling of N and Fe atoms are labelled.*

In fig. 4.7 the angular scans of scattered and recoiled atoms, extracted from the measured spectra, are compared with a scan simulated with the program MATCH. The data were measured by Dr. Grachev of the Groningen University [S. Y. Grachev, Thesis, University of Groningen, 2003 + publication]. Again the Molière potential was chosen for the ion-atom interactions, with a screening-radius reduction factor close to 0.8. To obtain the fit, the vertical position of the N atoms above the surface was adjusted to 0.24 Å. Also a comparison between simulations carried out using identical conditions with MATCH and TRIC is shown. Both simulations agree within the experimental uncertainties with the experimental data. The causes for the small deviations between the simulations with TRIC and MATCH are unknown. They may be due to the approximation corresponding to the matching procedure applied in MATCH.

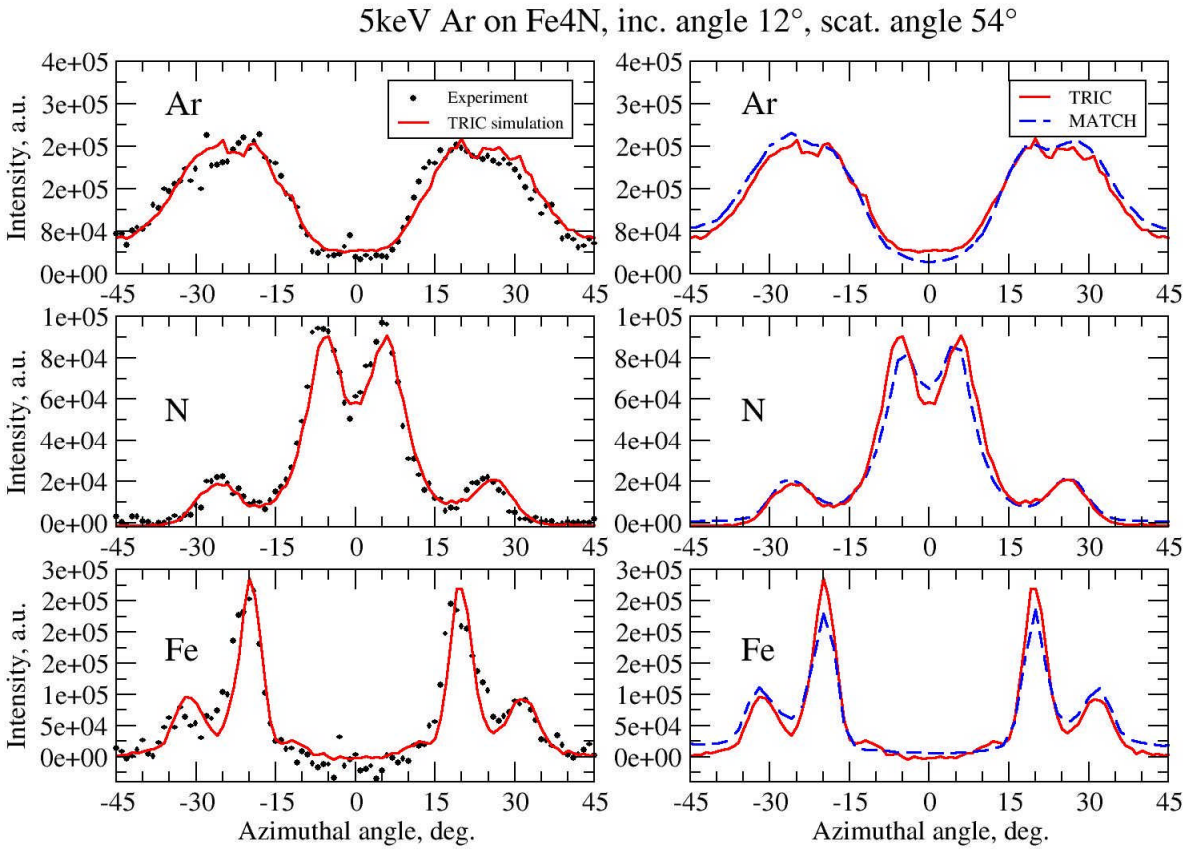

Fig. 4.7*. Comparison between experimental azimuth scans with simulation results obtained with the programs Match and TRIC, as indicated. The data are from the thesis of dr. Grachev [Thesis Grachevx]. The experimental data should be symmetric around 0° (coinciding with the (110) surface string). The small deviations reveal a small error in the measuring geometry.*

Next we turn to the simulation of scattering data of 100 keV H from Si. The data were taken by dr. Xxyy of the University of Lodz and simulated with the program sirbs6, which works in a similar way as FLUX (give all the references). In the experiment the yield of 100 keV H^+ ions incident into the normal (100) direction and backscattered over an angle of 135° was measured, using a single channel discriminator, as a function of the azimuth angle. The (100) Si crystal was rotated in steps around an axis close to the (100) normal direction. Some variation of the axial direction occurred during the experiments due to an imperfection of the goniometer used. The thickness of the sample probed by the chosen window in the discriminator corresponds to 60 nm in Si. All simulations were done for the ZBL??? potential and for 60 nm, corresponding to 220 layers of Si. A 2-D plot of the yield in a 5° x 5° area of the inner cone used in TRIC is shown in fig. 4.8. The point in the centre of this angular area is at an azimuth angle of 86° on the azimuth scale as used in fig. 4.9. At this azimuth angle the detector is close to an axial direction, as is visible from the blocking pattern in the figure. In the figure also the energy spectrum summed over the points of the 2-D angular area is shown. Note that the size of the detector is only xx x yy degrees, which constitutes a small fraction of the cone area. The comparison of the measured scan and scans simulated with the program sirbs6 and with TRIC is shown in fig. 4.9.

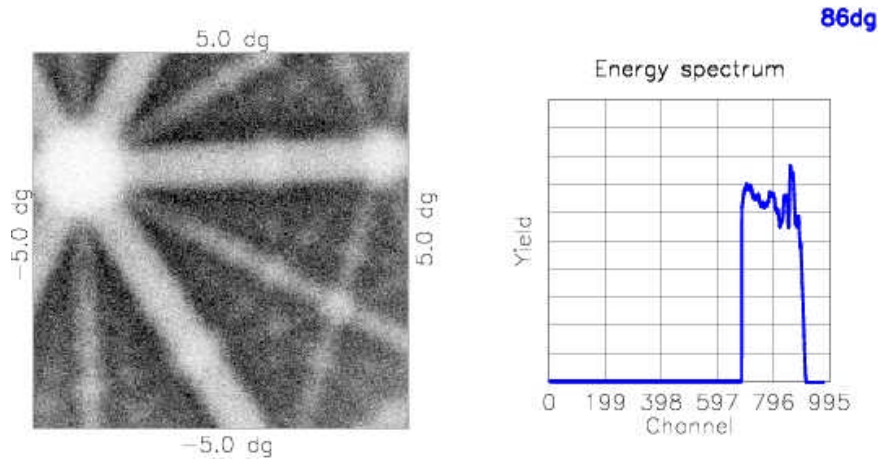

Fig. 4.8. *A 2-D plot of the yield of a 5^o x 5^o area corresponding to the inner cone used in TRIC and taken at a (central) azimuth angle of 86^o on the azimuth scale as used in fig. 4.9. Note that such a 2-D blocking pattern of the yield is calculated at each azimuth angle. The yield in the detector is only a small fraction of the total yield in this 2-D area. At this azimuth angle the angular area of the cone includes an axial direction. The energy spectrum summed over the points of this 2-D plot is also shown.*

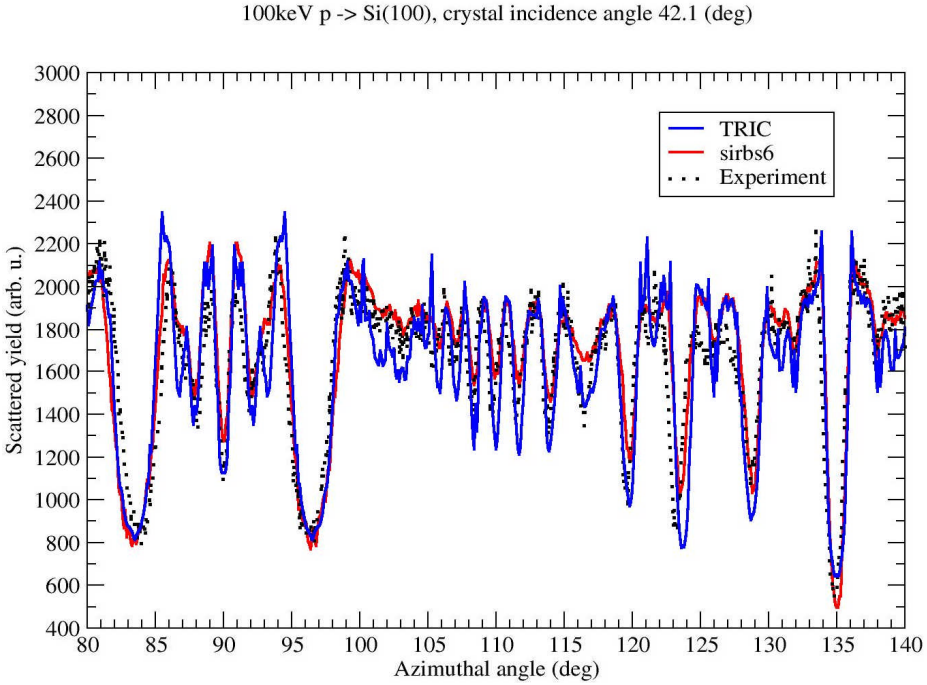

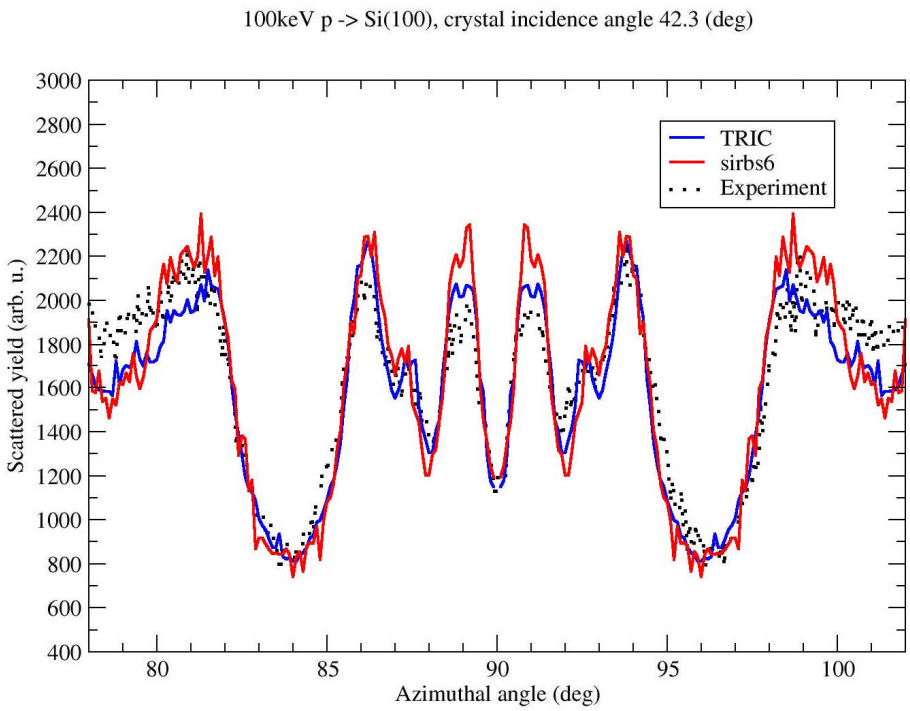

Fig. 4.9. *Measured and simulated azimuth scans for the scattering of 100 keV H+ ions from a (100) Si crystal. The rotation axis is close to the (100) normal direction. The detector is at a scattering angle of 135°. The azimuth angle 0° corresponds to the (010) surface string direction. The simulations were done with two programs (TRIC and sibs6), as indicated. In the upper frame the comparison is shown for a wide angular range of 60°. The rotation axis was not in a constant direction during this scan. In the lower frame simulations are shown in a smaller angular range, with an optimized direction of the rotation axis.*

As can be seen from the upper frame of the figure, the overall agreement between the two simulations and the experimental results looks satisfactory. In the lower frame a part of the azimuth scan is compared with simulations executed with an optimized geometry. In this more detailed picture, there are significant deviations. The deviation of the results obtained with sirbs6 as compared to TRIC is probably due to the partial application of single scattering theory as discussed in the introduction. The deviation of the simulations from the experimental results may be due to experimental causes, like the presence of a thin surface oxide, which increases the angular spread of the beam, or a deviation of the experimental energy window from the window applied in the simulations. Note also that there are deviations in the experimental data from the symmetry around 90° (=(010) surface string direction) as given by the crystal structure.

Finally we compare the scattering of 100 keV H^+ ions , this time from the first 20 double-layers of a bulk-terminated Si(111) crystal as simulated with TRIC and the program VEGAS (see introduction). The output of VEGAS is weighed with the cross section for scattering. The Vegas simulations were done by Dr. C Eames and Dr. S.P. Tear, Department of Physics, University of York, U. K. for precisely the same conditions as used for the TRIC simulations. The results are shown in fig. 4.10. Significant deviations between the two simulation results can be seen. Probably they are due to the approximations made in VEGAS. To investigate further the nature of the deviations, both programs were also used to simulate the backscattering of 100 keV H^+ ions from a single layer of Y-silicide grown on top of a Si(111) sample. The yttrium atoms form a single layer underneath a top layer of Si. This time the deviations between the two simulations are very small. This may be explained by the fact that for scattering from the second layer multiple scattering effects are hardly present. Also the experimental data are shown in the figure. The Vegas

simulations and the experimental data were generated by dr. Wood et al., Department of Physics, University of York, U. K. [ ].

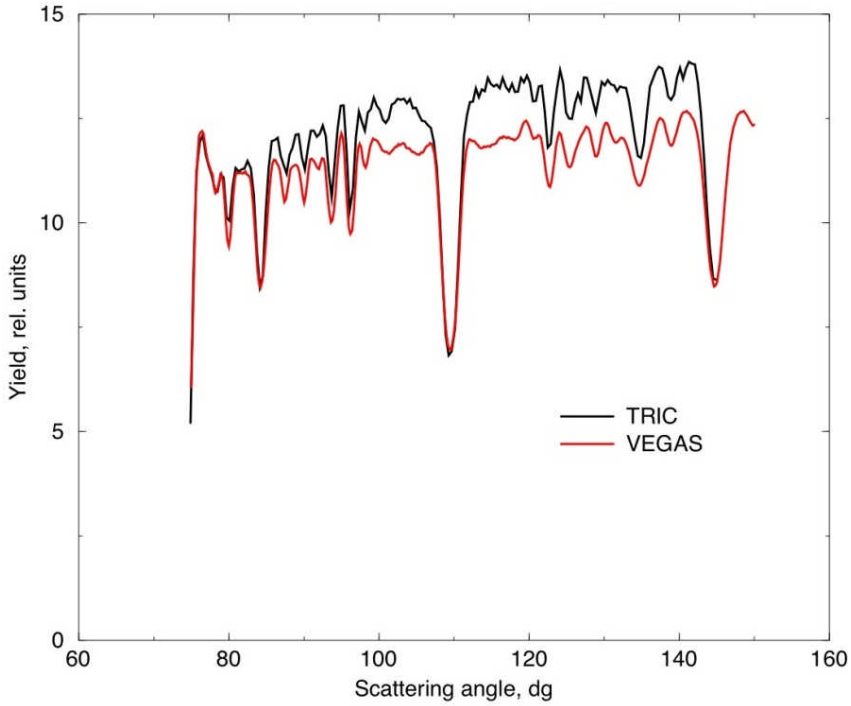

Fig. 4.10. *Comparison of simulations for 100 keV He^+ ions on Si(111), carried out with TRIC and with VEGAS for 20 double layers of bulk terminated Si(111). The beam was in the <411> axial direction and the scan is made by varying the detector angle in the (110) plane. The input parameters to both programs were equal: the Molière potential was chosen to describe the H-Si interaction; the thermal vibration amplitude was 0.15 Å; the detector opening angle was +/-0.64^o . In Vegas, electronic or nuclear stopping was not taken into account. The simulations with VEGAS were done by Dr. C Eames and Dr. S.P. Tear, Department of Physics, University of York, U. K. The TRIC simulations were done by Dr. V. Khodyrev.*

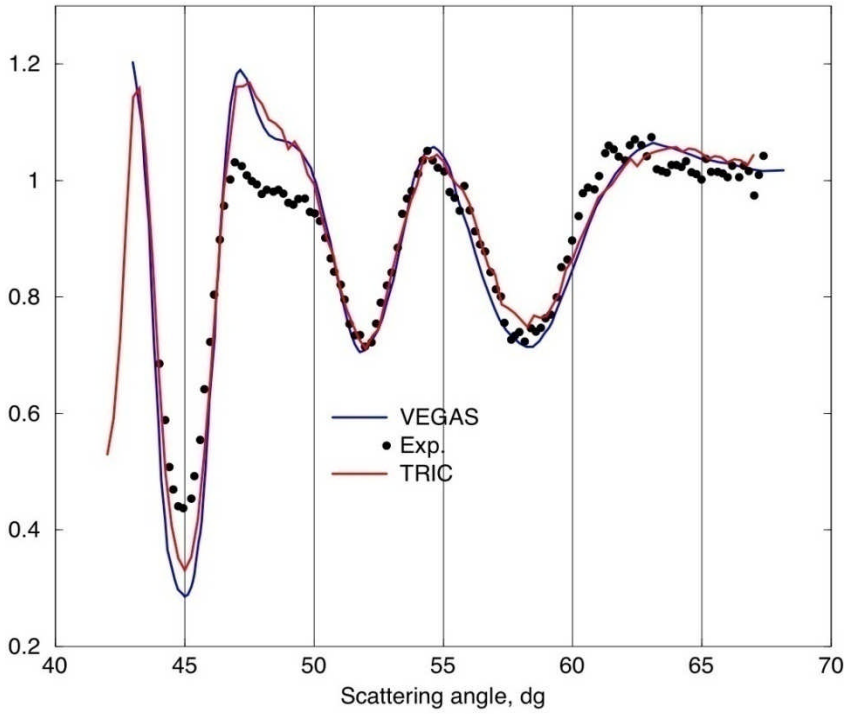

Fig. 4.11. *Comparison of an angular distribution of 100 keV H+ ions, scattered from Y, with simulations carried out with the programs TRIC and VEGAS. The sample is a Si(111) crystal, with a monolayer of Y-silicide on top. The top layer of the sample is Si, the Y is in the second layer. The beam was in the <100> axial direction; the angular distribution of the H+ ions was measured along the (110) plane. The data and the VEGAS simulation are taken from ref.[xx]*

T.J. Wood, C. Bonet, T.C.Q. Noakes, P. Bailey and S.P. Tear, Surf. Science 598 (2005) 120

4.4. Concluding remarks

The new computer simulation program TRIC can be used to simulate energy spectra of scattered or recoiled ions without any approximation, with the exception of the binary collision model and the model used for the inelastic energy loss to electrons. The program was tested successfully for LEIS and MEIS by comparing with measured data and with data generated by other simulation programs. The deviations of measured and simulated data could be explained by experimental uncertainties. The deviations between simulation results obtained with TRIC and MARLOWE were found to be small for the one case that was investigated. In principle the two programs should give identical output for the same input. Very small deviations between simulations made using TRIC and MATCH were seen. These might be due to small differences in the input as indicated above. Part of the deviations might be explained by the approximation inherent to the matching process applied in MATCH. The deviations between TRIC simulations and simulations with the program sirbs6 were found to be larger and must be due to the partial application of the single scattering model in the program sirbs6. The deviations between simulations carried out with TRIC and with VEGAS are larger. The deviations were found for simulations of scattering of 100 keV protons from a Si (111) sample consisting of 20 double layers. It should be noticed that commonly VEGAS is used for the simulation of thinner layers, were the deviations will be smaller.

Comparisons of simulation results with measured or simulated HEIS data are still underway. Simulation of a RBS spectrum, for a depth range in the sample of several hundreds of nm, takes up

to a week of computation time on a normal PC. It would be desirable to reduce this time by at least an order of magnitude. An obvious way to realize this is by running the program on a multi-processor computer as developed for modern computer games. This requires translation of the program from Fortran into C++. An increase in the computation speed by one or two orders of magnitude may be obtained. A possible second improvement of the computing efficiency may be achieved by allowing the formation of showers in the direction of the detector from trajectories within the inner cone as defined above. Given the importance of TRIC simulations of experimental data without the approximations or limitations mentioned above, the efforts to optimize the speed of TRIC would be worthwhile.

4.5. References

1. M.T. Robinson and I.M. Torrens, Phys. Rev. B 9 (1974) 5008.
2. Bykov, C. Kim, M.M. Sung, K.J. Boyd, S.S. Todorov and J.W. Rabalais. Nucl. Instrum. Phys. Res. B 114 (1996) 371.
3. M. H. Langelaar, M. Breeman, A. V. Mijiritskii, D. O. Boerma, Nucl. Instr. And Meth. B 132 (1997) 578.
4. J.H. Barrett, Phys. Rev. B3 (1971) 1527.
5. P.J.M. Smulders, and D.O. Boerma, Nucl. Instr. and Meth. B 29 (1987) 471.
6. M. Posselt, Crystal-TRIM, May 2004, http://www.fz-rossendorf.de/.
7. V. A. Khodyrev, V. Ya. Chumanov, K. K. Bourdelle, G. P. Pokhil, Nucl. Instr. and Meth. B 94 (1994) 523.
8. J. Czerbniak, G. Pudłowski, M. Moneta, Radiation Physics and Chemistry 76 (2007) 529.
9. R.M. Tromp and J.F.V. der Veen, Surf. Sci. 133 (1983)159.
10. J.W.M. Frenken, J.F. van der Veen and R.M. Tromp, Nucl. Instr. Meth. B 17 (1986) 334.
11. G. Moliere, Z. Naturforsch. 2a (1947) 133.
12. J.F. Ziegler, J.P. Biersack and U. Littmark, The Stopping and Range of Ions in Solids, Pergamon, New York (1985).
13. J. P. Perdew and Y. Wang, Phys. Rev. B 45 (1992) 13244.
14. O.S. Oen and M.T. Robinson. Nucl. Instr. and Meth. B 132 (1976) 647.
15.

Chapter 5.

ANALYSIS OF LOW-ENERGY HE-CU SCATTERING : THE ROLE OF THE POTENTIAL, SURFACE STRUCTURE AND MEASUREMENT GEOMETRY

5.1 Introduction

It has been demonstrated frequently that Low-Energy Ion Scattering (LEIS) combined with Time of Flight (ToF) detection of not too light ions like Ne or Ar is an ideal technique to probe the near-surface composition and structure of crystalline samples [xxxx]. Azimuth and polar scans show a sharp dependence on the scan angle and reflect the structure of the outermost layers. For light ions (H, He), with energies in the low keV range, the probing depth is much larger. The composition and structure of the first 10-20 layers of crystalline samples could be studied by measuring energy spectra and angular distributions of the scattering yield for such light ions. To determine the structure from the scans, computer simulations of the energy spectra and the angular scans have to be performed for trial structures and compositions. In the simulations the trajectories of many ions have to be calculated, starting from the point of impingement on the sample and ending when either the energy of the ions is below a pre-determined value, or when the ion leaves the sample. The ion trajectories can be well described in classical approximation, using the binary collision model in the asymptotic approximation. A number of simulation programs based on such trajectory calculations has been developed. Many of these programs make use of additional approximations, based on single scattering theory, to limit the time needed for simulations to practical values. These programs cannot be used for the analysis of LEIS data in which multiple and plural scattering cannot be neglected. Three types of programs exist in which approximations beyond the binary collision model are not (or hardly) present: MARLOWE, MATCH and TRIC. With these programs LEIS data can be well reproduced, provided that a proper screened potential is used to describe the binary collisions. In MARLOWE (and programs working on the same principle, like SARIC) the trajectories are followed directly, without measures to speed up the calculations. Since only a small fraction of the ions is making it to the detector, these programs need to be run on a supercomputer in order to calculate a full angular scan from the spectra generated at each measuring point. Also the layer thickness of the sample from which scattering is taken into account should be limited to < 10 layers. It would be too expensive to generate with MARLOWE many scans as needed for optimization of the parameters describing the structure or the potential. In the program MATCH the ingoing part and outgoing part (in reversed time mode) are calculated separately and then matched if the trajectories (almost) intersect and if the energies of the ingoing and outgoing parts of the trajectory correspond to each other within narrow tolerances. The large efficiency obtained for simulations of angular scans is at the cost of a minor uncertainty that could

be introduced by the matching process. In addition the program becomes slow when more than some 8 atom layers of the sample must be included. In the newly developed program TRIC these restrictions are not present. The program was described in the previous chapter.

In this chapter we report on the use of the program TRIC to simulate azimuth and polar scans of low-energy (2, 3 and 5 keV) He^+ ions scattered from a (100) Cu surface. The experimental data was taken at the University of Linz, Austria. Part of the data was analyzed before by comparison with computer simulations carried out with the program MARLOWE [ ], but a good agreement between measured and simulated data was not obtained. In these simulations the Molière potential with an optimized screening radius reduction factor of 0.53 was used to obtain the best fit.

In the present study the simulations were carried out for many different values for the parameters determining the shape of the angular distributions: the inter-atomic interaction potential, the relaxation of the top two layers of Cu(100) and also the measuring geometry. We used a potential obtained from Hartree-Fock (HF) calculations [ ], that were performed for this study by Dr. V. Kuzmin, Joint Institute for Nuclear Research, Dubna.

5.2 The He-Cu interaction potential

For the He energies used in this work the ion velocities are lower by a factor > 30 as compared to the Bohr velocity. This implies that the interaction potential may be calculated with the HF method [ ], or the Density Functional Theory (DFT) model [ ], in which full polarization of the electron configuration is assumed for all relevant He-Cu distances. This dynamic potential is presented as the product of the Coulomb potential and a screening function φ(r). In fig. 5.1 the function φ(r) is given for different methods of calculation for a neutral He-Cu pair and also for the interaction between a He^+ ion and a Cu atom. In the calculations for He^+ it was found that, already at large He-Cu distances, two electrons are on the He atom, with an electron missing on the Cu atom. Since the Cu atom is embedded in the metallic bulk, this missing electron will be replenished almost immediately. For this reason we used the potential calculated for neutral He-Cu in the simulations. Small differences between the screening functions calculated by first principles methods are visible in fig. 5.1 for a separation distance > 1 Å. Within the bulk of Cu the interaction radius is limited to half the nearest-neighbor distance, i.e. to values < 1.3 Å. Only for projectiles approaching the surface an interaction radius of 2 Å may be used. Since at distances beyond 1 Å the potential is weak, the influence of the small deviations in this region is minor. In addition solid state effects will be present at these distances. For the simulations we used a fit to the calculated 2D HF points, using the function:

$\phi(r/a_F) = \sum_{i=1}^{3} C_i \exp(-b_i r/a_F)$, with a_F the Firsov screening function given by:

$$a_F = \frac{0.88534138 a_0}{(Z_1^{1/2} + Z_2^{1/2})^{2/3}}$$

where a_0 = 0.529 Å is the Bohr radius, Z_1 and Z_2 are the atomic numbers of the elements involved. The coefficients obtained from the fit are:

C_1 = 0.1553 b_1 = 0.3450095 C_2 = 0.71459 b_2 = 0.8110852 C_3 = 0.13011 b_3 = 4.5114415.

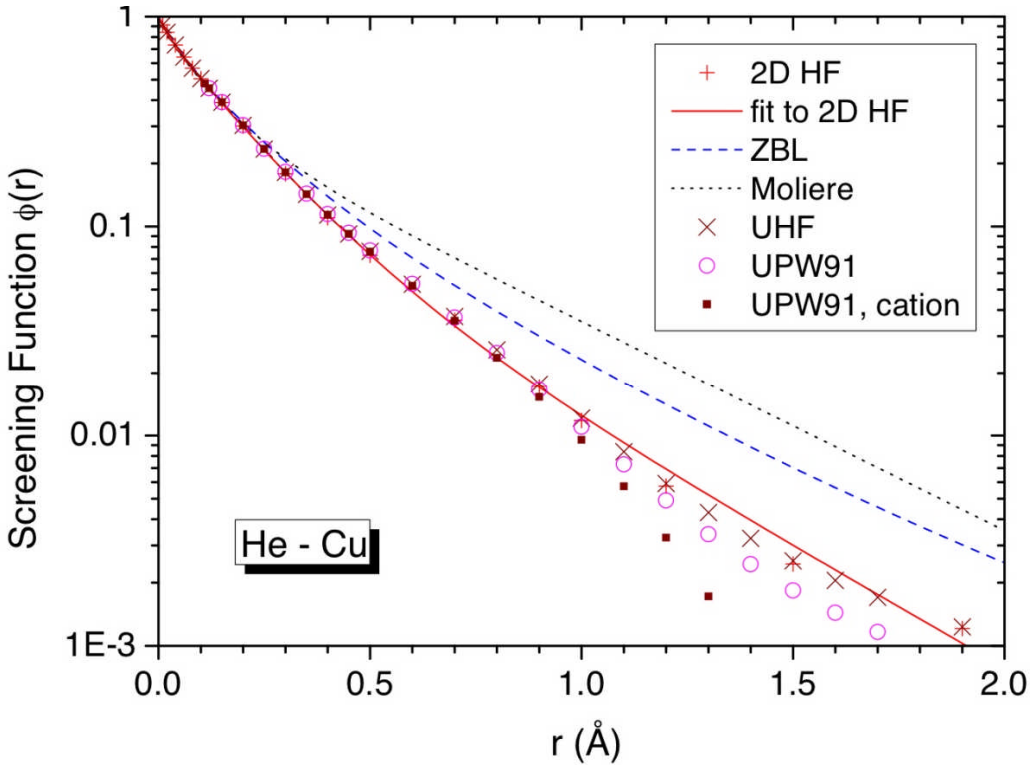

Fig. 5.1. *Screening functions for the He-Cu interaction calculated with different methods. The points calculated with the HF method using a finite set for expansion of the wave functions (2D HF) are indicated by red crosses (+). The red line results from a fit to the 2D HF points. This screening function was used in the simulations. Screening functions, calculated by unrestricted Hartree-Fock (UHF) methods (X) and by DFT (O) (corresponding to PW91 exchange-correlation potentials [see mail Kuzmin]) are also indicated. The brown squares are the result of DFT calculations for a He-Cu pair with one missing electron. For comparison also the Molière and the ZBL screening functions are shown. All calculations were done by Dr.V. Kuzmin.*

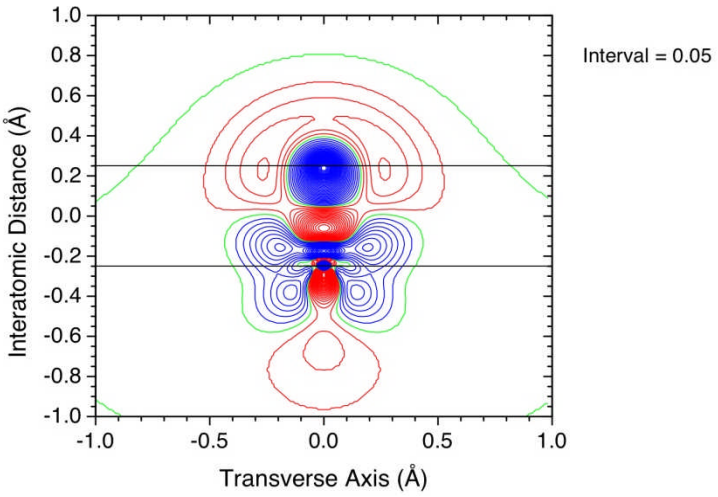

Fig. 5.2. *Difference of electronic density as computed with the DFT model and the density obtained by superimposing the atomic densities. The coordinates of the He atom are (0, 0.25) and of the Cu atom (0, -0.25). Extra charge is indicated in blue; charge depletion is in red.*

In fig. 5.3 the HF screening function for neutral He-Cu is compared with screening functions calculated for the Molière potential with the full screening radius and with a screening radius reduced by a factor of 0.53 as used in the previous simulations with MARLOWE. This last

screening function deviates strongly from those based on model calculations. Also static potentials were calculated by Dr. Khodyrev, in which polarization effects are neglected. The associated screening functions are also depicted in fig. 5.3.

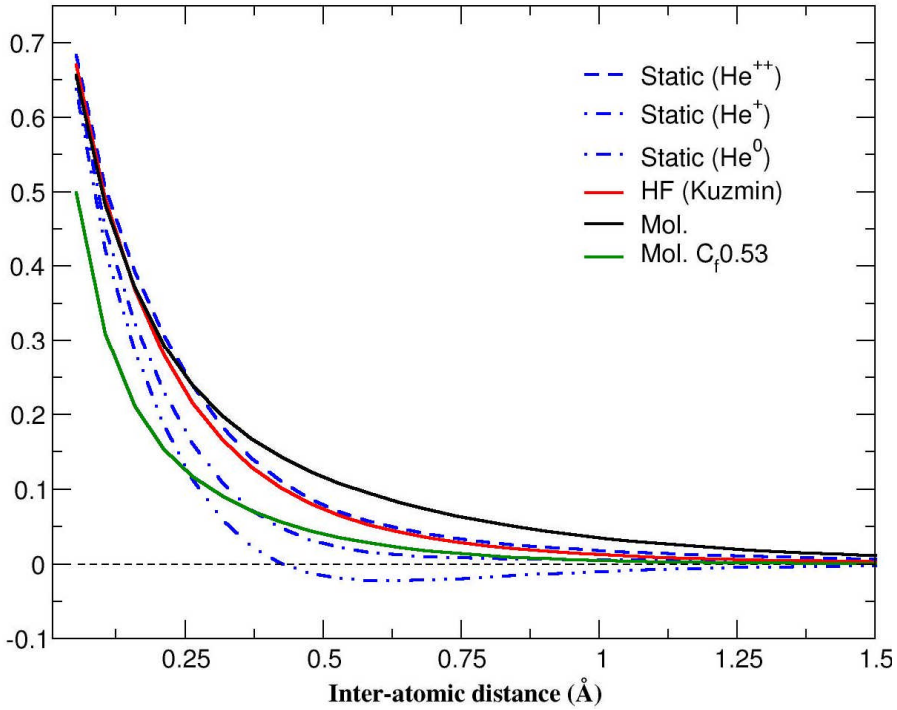

Fig. 5.3. *Screening functions for the He-Cu interaction calculated for static potentials compared with the HF screening function and screening functions for the Molière potentials with and without a screening radius reduction factor of 0.53 applied.*

These potentials were calculated using the electron wave functions for a Cu atom and a He atom or He ion as tabulated in ref. [ ]. The potential was calculated from the sum of the mutual Coulomb interactions between the nuclei with their electrons. In the calculations summations over the contributions of separate electrons were replaced by integrations over the respective electron densities. It is remarkable that the static screening function calculated for a He ++ ion and a Cu atom is close to the HF result.

5.1 Experimental data

The data was measured and made available to us by the group of prof. P. Bauer, Institute for Experimental physics, Johannes-Kepler University, Linz. Part of the data was published before in a number of papers [ ].The experiments were performed using the Time-of-Flight (TOF) LEIS setup ACOLISSA [7] with a fixed scattering angle of 129^o and a detector acceptance angle of 0.92^o. The angular precision of the manipulator is ± 0.1^o and ±0.2^o for polar and azimuth scans, respectively. The time resolution of the system is set to typically 10–25 ns. A post-acceleration voltage was applied along part of the flight path between sample and detector to separate backscattered ions from neutrals. The primary beam current was set to 25–100 nA in full beam mode, yielding 5–20 pA in the chopped beam mode. At normal incidence, the beam spot on the sample was smaller than 1 mm in diameter. From this it was concluded that, for beams at an angle < 65^o with the surface normal, the full irradiated spot is visible for the detector. The measurements were performed using a Cu(100) single crystal surface. The sample was prepared by repetitive sputtering-annealing cycles, performed with 3 keV Ar^+ ions and subsequent heating to 650 K. The purity of the sample and the

crystal structure were checked by Auger electron spectroscopy (AES) and low-energy electron diffraction (LEED). A beam of He^+ ions with an energy of 3 keV was used to measure an azimuth scan, with the beam in the (100) direction normal to the sample surface. The sample was rotated around the (100) normal in an angular range from -10^o to $+ 110^o$ and spectra were taken at 2^o intervals. On this angular scale, 0^o coincides with the (110) surface string direction. The ToF spectrum recorded at 0^o (corresponding to the (110) surface string direction in the scan) is shown in fig. 5.4.

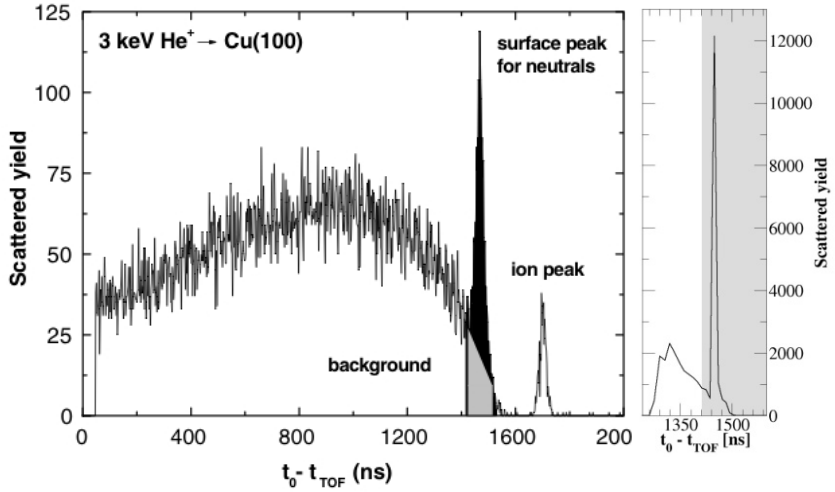

Fig. 5.4. *ToF spectrum recorded at 0^o (corresponding to the (110) surface string direction in the scan). As copied from ref. [xx]. The window corresponding to the energy window to obtain the azimuth scan is indicated. In the right frame the corresponding simulated spectrum, converted to a time scale, is shown, with the window used in the simulations. Notice that, due to the finite resolution of the experiment, the surface peak in the simulated spectrum is much higher and narrower than in the experiment.*

The spectrum is composed of a surface peak with a continuous background at lower velocities. In addition a peak formed by post-accelerated He^+ ions is formed at a higher velocity. This peak is entirely due to scattering from the surface [brongersma, bauer PRL]. The energy resolution of this spectrum is 60 eV as calculated from the ion peak width. The azimuth scan is obtained by plotting, as a function of the scan angle, the sum of the channel contents in the window from 2365 keV to 2722 keV) indicated in fig. 5.4, containing the surface peak, plus the content of the He^+ ion peak. In a similar way a polar scan was measured with 2 keV He^+ ions by rotating the sample around a (010) surface string direction. Spectra were recorded in 2^o steps for a polar angle range of -90^o (beam parallel to the surface) to $+20^o$ (detector direction at 20^o from the surface). Here the detector resolution was 109 eV and the energy window containing the surface peak was from 1.576 keV to 1.778 keV. Also a (010) polar scan was taken under the same conditions with 5 keV He^+ ions. Here the energy window containing the surface peak was from 3.951 keV to 4.387 keV and the resolution was 84 eV.

5.4. Comparison of experimental data with simulations.

Using the program TRIC simulations of the spectra measured in the angular scans were carried out for the same geometries as used in the experiments and for the same opening angle of the detector. The simulations were done, using 10^6 primary trajectories for each spectrum, for 20 layers of Cu in the (100) configuration, with a vibration amplitude of 0.084 Å for Cu atoms in the bulk. The vibration amplitude of the Cu atoms in the top layer was taken as 0.106 Å (perpendicular to the

surface) and 0.151 Å (parallel to the surface . The relaxation of the first and second Cu layers was taken as + 1.6% (expansion) and – 1.7% (contraction), respectively [ ]. To compare the result with the measured spectrum, as shown in fig. 5.4, the energy scale was converted into a time scale using the flight path (0.65 m) as used in the experiments. The result is shown in the right panel of fig.5. 4. As can be seen, the window corresponding to 20 Cu layers is approximately a factor of 2 broader than the window taken for the azimuth (and polar) scans.

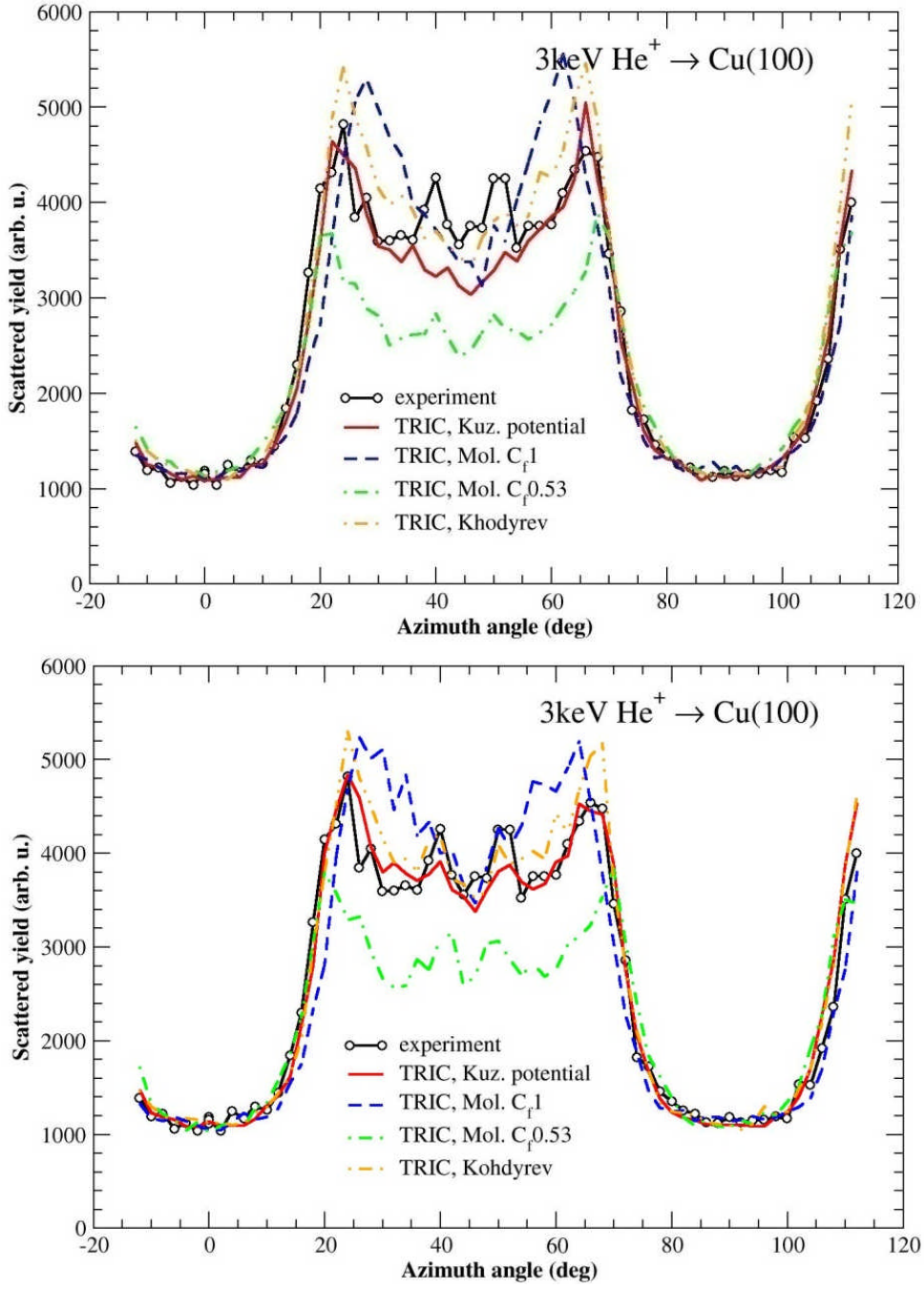

Fig. 5.5. *The experimental azimuth scan compared with simulations using 4 different potentials as indicated: Kuz.= HF potential, Mol. C_f 1=Molière potential , C_f 0.53=Molière potential with screening radius reduced by a factor 0.53, Khodyrev= static potential for a He^{++}-Cu pair. In the top panel the original measuring geometry with the rotation axis in the (0,0.1) normal direction was used. In the bottom panel the rotation axis is in the (0.017,0,1) direction. The direction of the (110) and (1-10) surface strings correspond to 0^o and 90^o, respectively. At these angles broad dips are centered, which are due to blocking.*

Azimuth scans were obtained by integrating the simulated yield using the same energy windows as in the experiment. This was done for 4 different potentials, described in Section 5.2. A scaling factor of the yield was fitted in the comparison with the experimental scan shown in the top panel of fig. 5.5. It turned out that the scaling factors obtained for the best fits were equal within the statistical uncertainties. This was the reason to use one single scaling factor for all 4 potentials. As can be seen, the best fit is obtained for the HF potential (Kuz. Potential). The overall features are reproduced, but the detailed structure in the broad peak between azimuth angles of 20^o to 70^o is not well reproduced. To improve the fit we decided to introduce a small deviation from the geometry as used in the experiments, assuming that the rotation axis used to measure the azimuth scan was not precisely coinciding with the (100) crystal direction. It is clear that there is a small imperfection, since the measured scans reveal some deviation of the 4-fold geometry expected for the fcc Cu structure. After some optimization of the coordinates of the rotation axis, the result shown in bottom panel of fig. 5.5 was obtained. Here the rotation axis is in the (0.017,0,1) direction instead of in the (0,0,1) direction, meaning that the deviation is 1^o. We suppose that such a small deviation is within the experimental uncertainties. With the small change of geometry an almost perfect fit is obtained for the HF potential, while the deviations between the measured and simulated scans for the other 3 potentials are statistically significant.

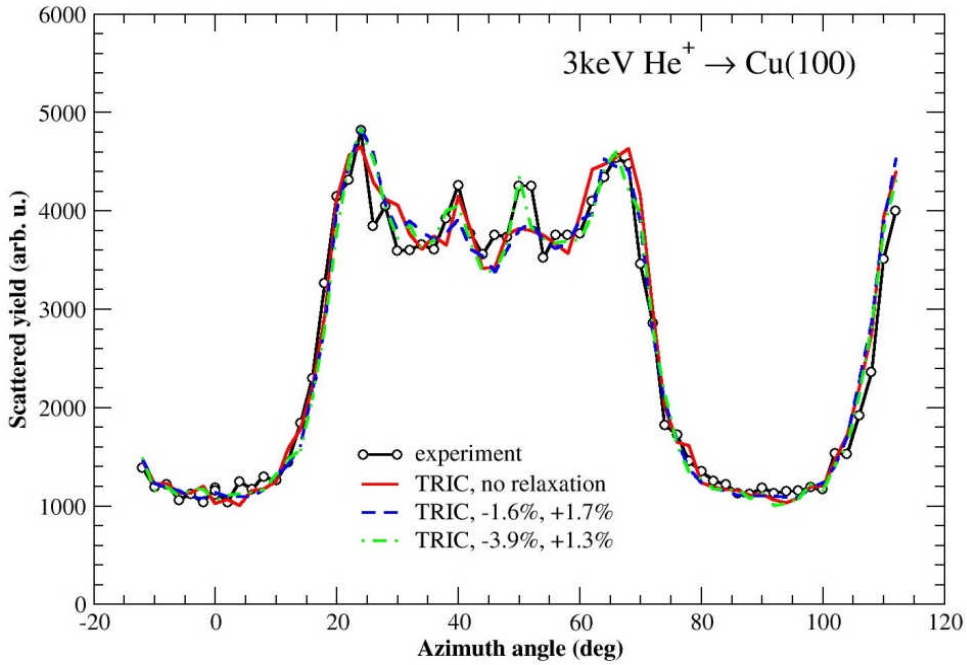

Fig. 5.6. *Comparison of the experimental azimuth scan with simulations carried out for 3 different sets of values for the relaxation as indicated.*

To test the sensitivity of the scans to the surface structure, we performed simulations with the HF potential and modified geometry for 3 different sets of values for the relaxation of the surface layers: the (recommended) values of +0.16%/-0.17% used before, no relaxation and a relaxation of 3.9% of the outer layer combined with an inward relaxation of 1.3% for the second layer.

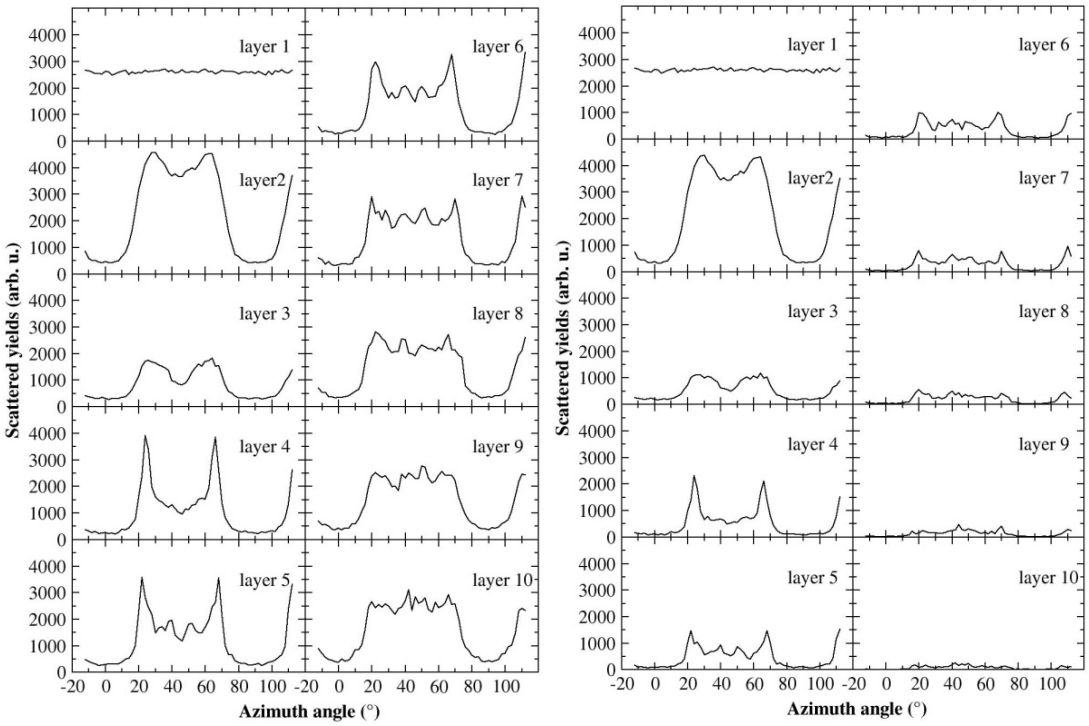

Fig. 5.7. *Simulation for the parameter values mentioned in the text of the yield per layer. The results in the left panel are obtained without a restriction to the energy of the detected particles; in the panel at the right an energy window as used for the experimental azimuth scan is applied.*

This last set of values was used in work of Draxler et al. [ ].The comparison with the measured scans is depicted in fig 5.6. The differences are very small, but it might be concluded that the larger relaxation gives a better fit. It is hard to judge if the difference is relevant.

To test further the surface sensitivity, the simulated yield per layer is plotted in fig. 5.7. The simulations were done with the HF potential, modified geometry and relaxation values of +1.6%/-1.7%. At the left side of this figure the results are shown with no restriction on the energy; at the right side the results are shown with the energy window as applied for the azimuth scans. From the figure it is clear that the contribution to the scans of layers deeper than the 10^{th} layer may be neglected. It is interesting to see that the two small peaks visible in the azimuth scan at angles of 40^{o} and 50^{o} are due to contributions from layers 5-7.

In fig. 5.8 simulations are shown that were carried out for 10 and 20 layers, respectively, with the same parameters as used for fig. 5.7. Also from this picture it is clear that the contribution from layers beyond the 10^{th} layer is not important.

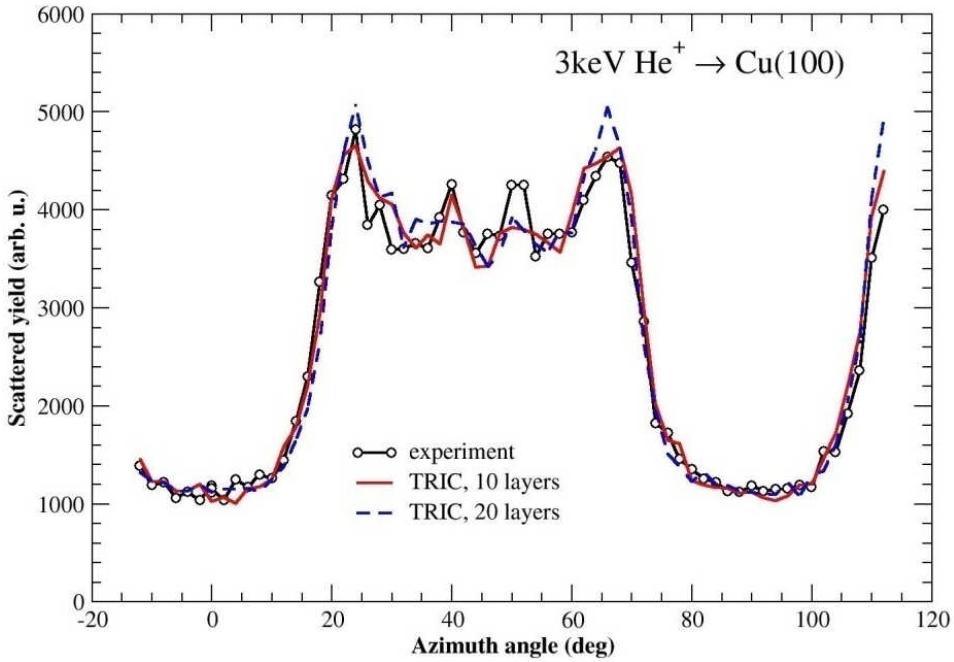

Fig. 5.8. *Comparison of the experimental azimuth scan with simulations with the HF potential, modified geometry and relaxation values of +1.6%/-1.7% carried out for 10 and 20 Cu layers, respectively, as indicated.*

For the simulation of the polar scans for 2 and 5 keV He^+ ions we used the HF potential and also the Molière potentials with and without the screening radius reduction factor of 0.53, in combination with the 3 sets of surface relaxation values used before. The simulations were carried out for the original geometry of the measurement, i.e. with the rotation axis in the (010) surface string direction, for 20 layers and the energy window as used in the experiments. Again by far the best fits to the experimental data were obtained for the HF potential. No differences were found for the 3 sets of relaxation parameters applied in the simulation of the azimuth scans.

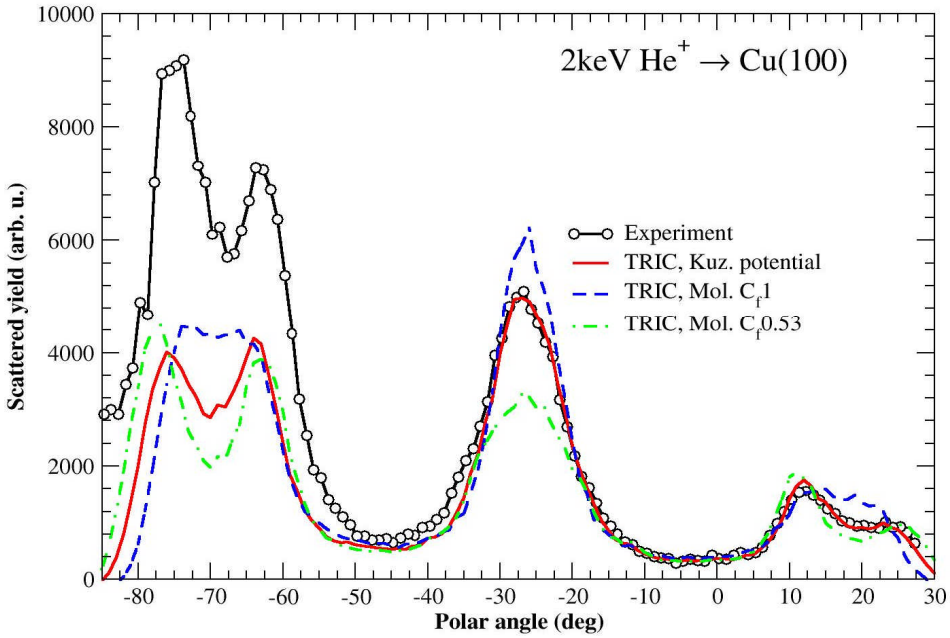

Fig. 5.9. *Experimental polar scan for 2 keV He^+ ions compared with the results of simulations with the different potentials as indicated and relaxation values of +1.6%/-1.7%.*

In fig. 5.9 the experimental polar scan for 2 keV is compared with the results of simulations with the different potentials and relaxation values of +1.6%/-1.7%. As can be seen, for the HF potential, a perfect fit is obtained for 2 keV for a range of polar angles between -40^o and + 30^o. The fit in this region is a lot worse for the Molière potentials. In the range between -85^o and -50^o there is a serious lack of fit, even when the two peaks at -62^o and -75^o are at the right positions in the simulations. It would be hard to imagine that in this latter angular range the simulation model would not be correct, while it reproduces the first angular range so perfectly. To trace the cause of the lack of fit we show in fig. 5.10 for this case the yield per layer for the first 10 layers. In the left frame the yield per layer is shown without a restriction of the energy;

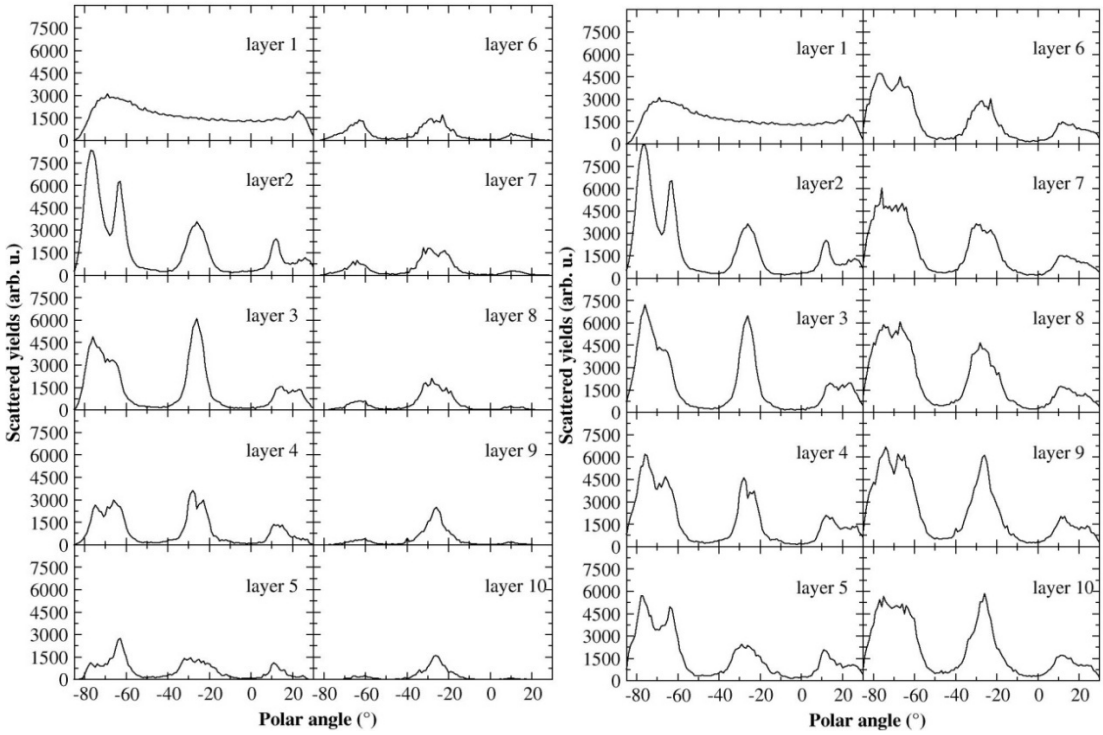

Fig. 5.10. *The yield per layer calculated for the polar scan for 2 keV using the HF potential. In the left frame no restriction to the energy is applied; in the right-hand frame same energy window as used to construct the polar scan is applied.*

In the frame on the right the same energy window as used to construct the polar scan is applied. From this result it may be concluded that the ratio of the intensity of the peaks in the polar scan above and below -50^o is seriously affected by the contribution from layers 6-10. For this reason we changed the model used in the simulations for electronic energy loss from the Oen-Robinson model to the ZBL model. The stopping power calculated with the latter model is lower by approximately a factor of 2. The result of the simulation carried out with this lower electronic energy loss and with the HF potential is shown in fig. 5.11. The difference due to this large change in stopping is not very significant. Therefore, it is improbable that a good fit in the angular range from -85^o to – 50^o can be obtained by improving the model for the electronic energy loss.

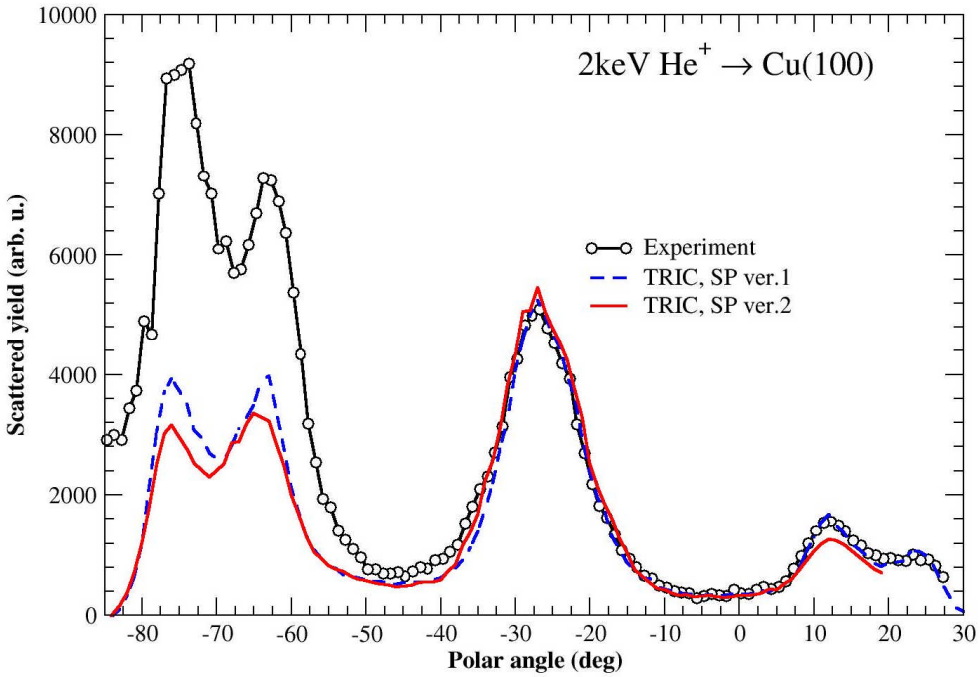

Fig. 5.11. *The same scan as shown in fig. 5.9, simulated with the HF potential (SP ver1) compared with a scan in which a value for the electronic energy loss that is smaller by approximately a factor of 2 was used (SP ver2).*

A plausible explanation for the discrepancy is that at these more glancing angles a part of the beam hits the sample close to the edge, where polished single crystals are commonly a little bit rounded. As a consequence, part of the beam may "see" upward steps or even facets that could give rise to a higher yield. In the figure it can be seen that yield is measured in the range from -80° to-90°, where the yield should be close to zero due to blocking effects. This indicates also an imperfection in the measurements. It would be worthwhile to repeat the measurements as a check.

Qualitatively the same comments as made for the 2 keV polar scan also apply to the 5 keV scan. A very good fit is obtained for polar angle > -30°; there is a serious lack of fit for more glancing angles. This is illustrated in fig. 5.12, where simulations of the polar scan for 5 keV He^+ ions, calculated with three different potentials as indicated, are compared with the experimental data. In the angular region from -30° to + 30° the simulation with the HF potential is much better than those obtained with the Molière potentials.

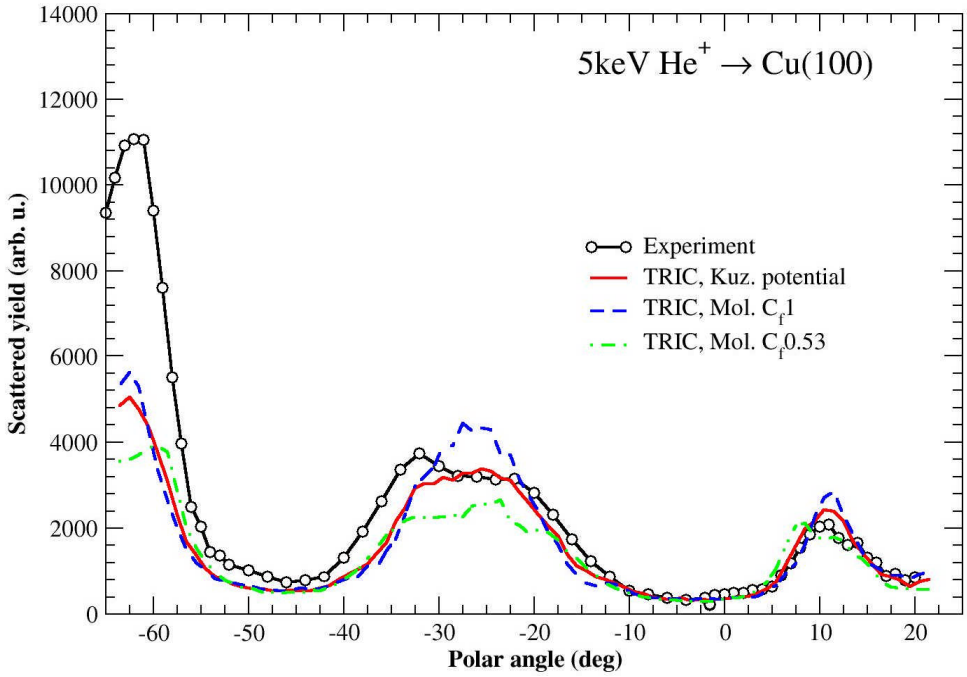

Fig. 5.12. *Experimental polar scan for 5 keV He^+ ions compared with the results of simulations with the different potentials as indicated and relaxation values of +1.6%/-1.7%.*

5.5 Conclusions

The first conclusion of the work presented in this chapter is that it is of utmost importance to use a proper potential to describe the interaction of the projectiles with the atoms in the sample. Only potentials obtained by first-principle methods are suitable. In the present case a dynamic potential, in which the polarization of the projectile-atom pair is fully taken into account gives excellent results. For medium-to high energies a static potential may be more suitable. In this type of potential no polarization effects are taken into account. Such a potential can be calculated from the tabulated electron wave functions for the projectile and the atom as described in section 5.2. Methods to calculate partial polarization have not been developed yet.

A second conclusion is that the measurement with ToF of angular scans of the scattered yield of light (H,He) ions from crystal structure can be used to study the composition and structure of the first 10 to 20 layers. The measurements must be carried out with high precision regarding the measuring geometry. The quantitative interpretation of the data by comparing with simulations has been, until now, a bottleneck for this type of studies. With the program TRIC these simulations are possible in a reasonable computation time. This means that a new tool (LEIS-ToF with light ions) has become available for such studies. This tool is less complicated than a set-up for MEIS as used for such studies. At the same time it has been shown in this work that LEIS-ToF with light ions is not well suited for the study of the detailed structure of surfaces. For this purpose it would be better to used heavier ions as projectiles, like Ne or Ar ions of a few keV.

Conclusiones principales de la tesis "Nuevos métodos para análisis de alta resolución con haces de iones" por Roch Andrzejewski.

El capítulo 2 de esta tesis da una visión general del estado actual de las técnicas de análisis con haces de iones. La conclusión de esta visión general es que son posibles y deseables nuevos desarrollos. Por una parte, se trata de la creación de un detector bidimensional sensible a la posición que combina una gran resolución en energía con la capacidad de discriminar entre los diferentes tipos de iones que llegan al detector. Además, se explican las razones por las que estos detectores deben medir de manera efectiva todos los estados de carga de los iones detectados. Por otra parte, se describen las razones por las que las aproximaciones realizadas en los programas de simulación utilizados para el análisis de los datos experimentales no son adecuadas para análisis precisos en numerosas ocasiones. Se llega a la conclusión de que tanto la instrumentación como el análisis de datos necesitan ser mejorados para la realización de análisis con haces de iones con precisión del orden de nanómetros.

El capítulo 3 trata del diseño de un nuevo tipo de espectrógrafo magnético. En la práctica, se trata de un detector que posee todas las características de un detector ideal como se definen en el capítulo 2. El instrumento fue diseñado satisfactoriamente. Se construyó por una empresa de acuerdo a las especificaciones y fue instalado en el Centro de Microanálisis de Materiales de la Universidad Autónoma de Madrid. Ha pasado todos los tests de funcionamiento realizados hasta el momento.

El capítulo 4 describe un nuevo tipo de programa de simulación para análisis con haces de iones. Es capaz de reproducir espectros en energía de iones dispersados o en retroceso por medio del cálculo de muchas (hasta 10^6) trayectorias de manera similar a otros programas existentes, pero eludiendo las aproximaciones usuales. Esto se consigue introduciendo un nuevo concepto matemático en estas simulaciones, concretamente el de muestreo por importancia. Esto permite la realización de simulaciones más rápidamente en un factor grande (dependiendo del caso hasta 10^5). Esto permite la omisión de las aproximaciones. El programa fue probado satisfactoriamente comparando sus resultados con los de otros programas existentes previamente para los casos en que las aproximaciones incluidas en ellos son válidas. También se simularon datos para compararlos con experimentos y se encontró que pueden reproducirlos dentro de los errores experimentales. Se ha demostrado que los programas habitualmente utilizados en muchas publicaciones producen datos con desviaciones significativas debido a las aproximaciones que emplean.

En el capítulo 5 se analizan datos de dispersión de iones de He de baja energía por un monocristal de Cu, medidos por un sistema de tiempo de vuelo de alta resolución. Para ello se utilizó el programa TRIC. Otros intentos previos de reproducir estos datos por medio de simulaciones no fueron exitosos. Se obtuvo un ajuste satisfactorio empleando un potencial de Hartree-Fock para describir la interacción ion-sólido. Hasta el momento sólo se habían empleado potenciales "empíricos". También se introdujo una pequeña corrección en la geometría de medida. Las muchas simulaciones necesarias para variar los parámetros mencionados no hubieran sido posibles con otro programa distinto de TRIC. Las conclusiones principales son que los potenciales basado en cálculos de primeros principios deben ser usados para el análisis de los datos de dispersión de iones de baja energía. Este método, empleando iones ligeros no es apropiado para la determinación de la estructura superficial de muestras cristalinas, al contrario que en el

caso de iones más pesados como Ne o Ar. Sin embargo, combinada con el uso del programa TRIC la dispersión de iones ligeros de baja energía es una excelente herramienta para el estudio de las primeras 10-20 capas de muestras (cristalinas) para la determinación de su composición y estructura. Actualmente se esta probando en el CMAM el equipamiento necesario para la realización de medidas con este método.

En resumen, las conclusiones de esta tesis son que se han identificado las limitaciones actuales de las técnicas de análisis con haces de iones y se han realizado dos mejoras importantes, como son la creación de un nuevo tipo de detector que combina las propiedades necesarias para el análisis de alta calidad en la escala nanométrica y la creación de una nueva vía para el análisis de datos. Adicionalmente se muestra que la dispersión de iones ligeros puede ser una herramienta excelente para el estudio de las primeras 10-20 capas de las muestras (cristalinas).